#### الجمهورية الجزائرية الديمقراطية الشعبية

## République Algérienne Démocratique et Populaire Ministère de L'Enseignement Supérieur et de la Recherche Scientifique



# UNIVERSITÉ FERHAT ABBAS - SETIF 1 FACULTÉ DES SCIENCES

#### **THESE**

Présentée au Département de Physique

Pour l'obtention du diplôme de

#### **DOCTORAT EN SCIENCES**

Option: Physique du solide

Par

Mr. Boudissa Rabah

## **THÈME**

## Etude des Propriétés Physiques de quelques Composés Intermétalliques Binaires de Type AB<sub>3</sub>

Soutenue Publiquement le 28/06/2025 devant le Jury :

M. Boukelkoul	Professeur	Univ. Ferhat Abbas Sétif 1	Président
Y. Medkour	M.C.A	Univ. Ferhat Abbas Sétif 1	Directeur de thèse
T. Chihi	Professeur	Univ. Ferhat Abbas Sétif 1	Co-Directeur
Y. Benarioua	Professeur	Univ. Med Boudiaf M'Sila	Examinateur
I. Bouchama	Professeur	Univ. Med Boudiaf M'Sila	Examinateur
T. Ghellab	Professeur	Univ. Med Boudiaf M'Sila	Examinateur

#### الجمهورية الجزائرية الديمقراطية الشعبية

### République Algérienne Démocratique et Populaire Ministère de L'Enseignement Supérieur et de la Recherche Scientifique



## UNIVERSITÉ FERHAT ABBAS - SETIF 1 FACULTÉ DES SCIENCES

### **THESE**

Présentée au Département de Physique Pour l'obtention du diplôme de

#### **DOCTORAT EN SCIENCES**

Option: Physique du solide

Par

Mr. Boudissa Rabah

## **THÈME**

## Etude des Propriétés Physiques de quelques Composés Intermétalliques Binaires de Type AB<sub>3</sub>

Soutenue Publiquement le 28/06/2025 devant le Jury :

M. Boukelkoul	Professeur	Univ. Ferhat Abbas Sétif 1	Président
Y. Medkour	M.C.A	Univ. Ferhat Abbas Sétif 1	Directeur de thèse
T. Chihi	Professeur	Univ. Ferhat Abbas Sétif 1	Co-Directeur
Y. Benarioua	Professeur	Univ. Med Boudiaf M'Sila	Examinateur
I. Bouchama	Professeur	Univ. Med Boudiaf M'Sila	Examinateur
T. Ghellab	Professeur	Univ. Med Boudiaf M'Sila	Examinateur

## **Dedication**

#### I dedicate this work:

- -To my dearest parents;
- -To my dear wife in particular;
- -To my little princess: Serine;
- -To my children: Taki Eddine, Heithem Seif Eddine & Abderrahmene.
- -To all my family & friends
- -To everyone who contributed directly or indirectly to the completion of this work.

Rabah Boudissa

#### Acknowledgements

I sincerely thank **ALLAH**, the Almighty, for granting me the strength, willpower, courage, and health to accomplish this thesis.

First, I would like to express my sincere gratitude to the President of the Jury: **Professor M. Boukelkoul** for dedicating time and effort to evaluate my work.

I express my deepest gratitude to my thesis supervisor, **Dr. Y. Medkour**, Associate Professor at **Ferhat Abbas University of Sétif 1**, for his continuous support and guidance throughout this research.

I extend my heartfelt appreciation to my co-supervisor, **Professor T. Chihi**, for his valuable discussions, insightful advice, and exemplary human qualities, which have greatly contributed to the success of this work.

My sincere thanks and deep respect go to all the members of the jury: **Y. Benarioua, I. Bouchama and T. Ghellab**, for accepting to evaluate this work and for honoring me with their participation.

Rabah Boudissa

## **Summary**

General Introduction
<b>Chapter I: Generalities on the Fundamental Properties of Semiconductors 05</b>
I.1 Introduction
I.2 Definition of a Semiconductor and its Electronic Structure07
I.2.1 Electrical Conductivity
I.2.2 Energy Bands
I.2.2.1 Direct and Indirect Band Gaps10
I.2.3 Conduction by Electrons and Holes
I.2.4 Intrinsic Semiconductors
I.2.5 Extrinsic Semiconductors and Doping
I.3 Structural Properties of Semiconductors
I.3.1 Crystalline Semiconductors
I.3.1.1 Zinc-Blende and Rock Salt Structures
I.3.1.2 Lattice Parameters
I.3.1.3 The Reciprocal Lattice
I.3.2 Influence of Structural Properties on Semiconductor Applications 16
I.3.3 Methods for Determining Structural Properties
I.4 Optical Properties of Semiconductors
I.4.1 Electromagnetic Waves
I.4.2 The Electromagnetic Spectrum
I.4.3 Visible Light
I.4.4 Photons and Their Energy
I.4.5 Light-Matter Interaction in Semiconductors
I.4.5.1 Fundamental Absorption
I.4.5.2 Spontaneous Emission
I.4.5.3 Stimulated Emission
I.4.6 Recombination in Semiconductors
I.4.7 Refractive Index
I.4.8 Direct vs. Indirect Optical Transitions

I.4.9 Semiconductor Colors	23
I.4.10 Optical Absorption and Transmission	24
I.5 Elastic and Mechanical Properties of Crystalline Solids	24
I.5.1 Elastic Behavior of Crystals	25
I.5.2 Stress and Strain: Hooke's Law	26
I.5.3 Elastic Moduli and Mechanical Constants	27
I.5.3.1 Young's Modulus E	27
I.5.3.2 Bulk Modulus (B)	27
I.5.3.3 Shear Modulus (G)	28
I.5.4 Elastic Constants and Anisotropy	29
I.5.5 Zener Anisotropy Factor and Debye Temperature	30
I.5.6 Debye Temperature θ <sub>D</sub>	30
I.6 Diluted Magnetic Semiconductors (DMS)	30
I.6.1 Structural, Electronic, and Magnetic Properties of DMS	31
I.6.1.1 Crystal Structures of DMS Materials	31
I.6.2 Theoretical Mechanisms of Magnetism in DMS	31
I.6.2.1 Exchange Interactions in DMS	32
I.6.2.2 Carrier-Mediated Ferromagnetic Ordering	32
I.6.3 Curie Temperature and its Dependence on Carrier Density	32
I.6.4 Optical and Transport Properties of DMS	33
I.6.4.1 Optical Effects in DMS	33
I.6.4.2 Electrical Transport in DMS	33
I.6.5 Applications of DMS in Spintronics	33
I.6.5.1 Key Spintronic Devices	34
I.6.6 Challenges and Future Prospects	34
I.7. Conclusion	34
Chapter II: First-Principles Methods and Computational Details	36
II.1 Introduction	37
II.2 Many-Body Problem and Approximations	37
II.2.1 Schrödinger Equation	37
II.2.2 Born-Oppenheimer Approximation	39

II.2.3 Self-Consistent Field Approximation
II.3. Density Functional Theory (DFT)42
II.3.1 Electronic Density
II.3.2 Hohenberg-Kohn Density Functional Theory44
II.3.3 Kohn-Sham Method45
II.3.4 Exchange-Correlation Functional Approximations
II.3.5 Self-Consistency in DFT Calculations
II.4 Pseudopotential and Plane Wave Methods47
II.4.1 Bloch's Theorem and the Plane Wave Approach48
II.4.2 Brillouin Zone Sampling
II.4.3 Cut-off Energy E <sub>cut-off</sub>
II.5 Pseudopotential Method50
II.5.1 Frozen Core Approximation
II.5.2 Phillips-Kleinman Formulation
II.5.3 Pseudopotential Construction
II.5.3.a Norm-Conserving Pseudopotentials
II.5.3.b Ultrasoft Pseudopotentials
II.6 Introduction to CASTEP Code and Calculation Details53
II.6.1 Overview of CASTEP Calculation Code53
II.6.1.1 Geometric Optimization with CASTEP54
II.6.1.2 Convergence in Cutoff Energy and k-Point Sampling in CASTEP 54
II.6.1.3 Band Structure and Density of States Diagrams
II.6.1.4 Optical Properties Computation in CASTEP 56
II.6.2 Calculation Method and Parameters56
II.7. Conclusion
Chapter III: Optical, Structural and Electronic properties of WClx58
III.1 Introduction
III.2. Computational Methodology61
III.2.1 Structural Optimization
III.2.2 Electronic Structure Calculations
III.2.3 Optical Properties
III.2.4 Phonon and Stability Analysis
III 3 Results and discussions 62

III.3.1. Structural Parameters
III.3.2. Electronic Band Structure
III.3.2.1. Band Structure Analysis
III.3.2.2. Projected Density of States (PDOS)69
III.3.2.3. Influence of Structural Characteristics on Band Structure 69
III.3.2.4. Comparison with Experimental Data70
III.3.2.5. Implications for Applications
III.3.2.6. Summary of Key Findings70
III.3.3. Optical Properties
III.3.3.1. Reflectivity and Absorption Coefficient
III.3.3.2. Dielectric Function Analysis
III.3.3.3. Optical Conductivity
III.3.3.4. Refractive Index and Energy Loss Function
III.3.3.5. Summary of Optical Properties and Potential Applications75
III.4. Discussion
III.4.1. Structural and Stability Analysis
III.4.2. Electronic Structure and Band Gap Analysis77
III.4.3. Optical Properties and Potential Applications
III.4.4. Technological Implications and Future Prospects
III.5. Conclusion
Chapter IV: Physical Properties of $4C_{16}H_{10}Br_2O_2$ : A DFT–Based Approach . 81
IV.1 Introduction
IV.2. Computational Methodology83
IV.2.1 Crystal Structure Optimization83
IV.2.2 Electronic Structure Calculations84
IV.2.3 Optical Properties Calculations84
IV.2.4 Charge Population Analysis85
IV.2.5 Computational Accuracy and Validation85
IV.2.6 Summary of Computational Parameters

IV.3. Results and discussions	86
VI.3.1. Structural Parameters	86
IV.3.2. Electronic Properties	88
IV.3.3. Optical Properties	92
IV.3.4. Population Analysis	97
IV.4. Conclusion	100
General Conclusion	101
Bibliographic references	105

## **List of Figures**

Chapter 1: Generalities on the Fundamental Properties of Semiconductors	
Figure I.1: Electrical conductivity of various solid materials at ambient temperature	9
Figure I.2: Band structures of an insulator, semiconductor, and conductor	10
Figure I.3: Direct and Indirect Band Gaps in semiconductors like GaAs and Si	11
Figure I.4: Electron transition from the valence band to the conduction band	11
Figure I.5: Formation of an electron-hole pair due to covalent bond breaking	12
Figure I.6: Band structures of n-type and p-type semiconductors	12
Figure I.7: Representation of the Zinc-Blende (ZB) structure, showing the tetrahedral	
coordination of atoms	14
Figure I.8: Representation of the Rock Salt (RS) structure, where empty and filled	
spheres represent Mn and X atoms, respectively	14
Figure I.9: Illustration of a triclinic unit cell, showing the three edge lengths	
and angles.	15
Figure I.10: First Brillouin Zone of a Zinc-Blende Crystal, showing the symmetry	
directions	16
Figure I.11: Electromagnetic wave	18
Figure I.12: The electromagnetic spectrum, showing different types of radiation and the	neir
applications	19
Figure I.13: The visible spectrum, showing the range of wavelengths corresponding to	)
different colors	20
Figure I.14: Absorption process in semiconductors	21
Figure I.15: Spontaneous photon emission in semiconductors	21
Figure I.16: Stimulated emission mechanism	22
Figure I.17: Direct vs. Indirect optical transitions	23
Figure I.18: Intrinsic colors of semiconductors based on bandgap	23
Figure I.19: Variation of energy and force with interatomic distance d	26
Figure I. 20: Various types of elastic deformations	27
Figure I.21: Bulk modulus variation in different semiconductors	28
Figure I.22: Shear deformation and mechanical properties	29

Chapter II: First-Principles Methods and Computational Details
Figure II.1: Different steps in the self-consistent resolution of the Kohm-Sham
Equations
Chapter III : Optical, Structural and Electronic properties of WClx $(x = 3 \text{ to } 6)$
Figure III.1: The region 80 to 86 atomic Cl % of the phase diagram for the
W-Cl system60
Figure III.2. The effect of Cl content on total energies of W-Cl system64
Figure III.3. Top and Perspective Views of the Crystalline Structures of WCl <sub>3</sub> , WCl <sub>4</sub> ,
$WCl_5$ , $\beta$ - $WCl_6$ , and $\alpha$ - $WCl_6$ "66
Figure III.4. Energy as a function on volume of WCl <sub>3</sub> (a), WCl <sub>4</sub> (b), WCl <sub>5</sub> (c), β-WCl <sub>6</sub>
(d) and $\alpha$ -WCl <sub>6</sub> (e)67
Figure III.5. Band structures and total densities of states of β-WCl <sub>6</sub> and α-WCl <sub>6</sub> 68
Figure III.6. The reflectivity (a), absorption (10 <sup>4</sup> cm <sup>-1</sup> ) (b), conductivity (c), real and
imaginary parts of dielectric function (d), refractive index (e) and loss function (f) for β-
WCl <sub>6</sub>
Figure III.7. The reflectivity (a), absorption (10 <sup>4</sup> cm <sup>-1</sup> ) (b), conductivity (c), real and
imaginary parts of dielectric function (d), refractive index (e) and loss function (f) for $\alpha$ -
WCl <sub>6</sub> 73
Figure III.8. The reflectivity (a), absorption (10 <sup>4</sup> cm <sup>-1</sup> ) (b), conductivity (c), real and
imaginary parts of dielectric function (d), refractive index (e) and loss function (f) for
WCl <sub>5</sub>
Chapter IV: Physical Properties of 4C <sub>16</sub> H <sub>10</sub> Br <sub>2</sub> O <sub>2</sub> : A DFT-Based Approach
Figure IV.1. The perspective view of C <sub>16</sub> H <sub>10</sub> Br <sub>2</sub> O <sub>2</sub> in orthorhombic Pbnc (N°60) (a)
and monoclinic P2 <sub>1</sub> /c (N°14) (b) crystal structures83
Figure IV.2 DFT calculated Band structure of C <sub>16</sub> H <sub>10</sub> Br <sub>2</sub> O <sub>2</sub> in Pbnc (a), and P2 <sub>1</sub> /c
(b) space group90
Figure IV.3 The partial density of states of C <sub>16</sub> H <sub>10</sub> Br <sub>2</sub> O <sub>2</sub> molecule in Pbnc
(a) and P2 <sub>1</sub> /c (b) space group93
Figure IV.4 Real and imaginary parts of the dielectric function of C <sub>16</sub> H <sub>10</sub> Br <sub>2</sub> O <sub>2</sub> molecules
in $Pbnc$ and $P2_1/c$ space groups as a function of energy93
Figure IV.5 The refractive index of $C_{16}H_{10}Br_2O_2$ in <i>Pbnc</i> and $P2_1/c$ space groups
as a function of energy93
Figure IV.6 The absorption of $C_{16}H_{10}Br_2O_2$ in <i>Pbnc</i> and $P2_1/c$ space groups as a function
of energy94
Figure IV.7 The reflectivity of $C_{16}H_{10}Br_2O_2$ in <i>Pbnc</i> and $P2_1/c$ space groups
as a function of energy.
Figure IV.8 The conductivity of $C_{16}H_{10}Br_2O_2$ in <i>Pbnc</i> and $P2_1/c$ space groups as a
function of energy.

Figure IV.9 The loss functions of $C_{16}H_{10}Br_2O_2$ in <i>Pbnc</i> and $P2_1/c$ space groups	
as a function of energy	.96

## **Table List**

Chapter III: Optical, Structural and Electronic properties of WClx $(x = 3 \text{ to } 6)$
Table III.1. Space groups, lattice parameters, angle, conventional volume, number
of cell formula of compounds and reference in the W-Cl system (a) This study at 0
GPa, (b) This study at 1.45 GPa63
Table III.2. Total energy, density and bond lengths between atoms for W, WCl <sub>3</sub> ,
WCl <sub>4</sub> , WCl <sub>5</sub> , $\beta$ -WCl <sub>6</sub> , $\alpha$ -WCl <sub>6</sub> and Cl <sub>2</sub> 64
Chapter IV: Physical Properties of 4C <sub>16</sub> H <sub>10</sub> Br <sub>2</sub> O <sub>2</sub> : A DFT–Based Approach
Table IV.1 The atomic coordinates of C <sub>16</sub> H <sub>10</sub> Br <sub>2</sub> O <sub>2</sub> in orthorhombic Pnca (N°60) and
monoclinic P2 <sub>I</sub> /c (N° 14) structures compared with the experimental values87
Table IV.2 The lattice parameters c/a, c/b ratios, volume, density, atomic number and
energy of in Pbnc (N°60) (a), P2 <sup>1</sup> /c (N°14) compound
Table IV.3 Mulliken of all electrons for C <sub>16</sub> H <sub>10</sub> Br <sub>2</sub> O <sub>2</sub> in Pbnc (N°60)97
Table IV.4 Atomic populations (Mulliken) of all electron configurations of atoms
for C <sub>16</sub> H <sub>10</sub> Br <sub>2</sub> O <sub>2</sub> in P2 <sub>1</sub> /c (N°14)97
Table IV.5 Geometric parameters of C <sub>16</sub> H <sub>10</sub> Br <sub>2</sub> O <sub>2</sub> in <i>Pbnc</i> (N°60) in brackets those
given experimentally
Table IV.6 Geometric parameters (Å) of $C_{16}H_{10}Br_2O_2$ in $P2_1/c$ (N°14) in brackets
those given experimentally99

## General Introduction

#### **General Introduction**

The rapid advancements in materials science have driven the development of innovative materials with tailored physical properties, enabling their integration into a wide range of technological applications. From semiconductors and optoelectronics to energy storage and organic electronics, the ability to predict and engineer material behavior at the atomic scale has become a fundamental challenge in modern research. This thesis explores the structural, electronic, and optical properties of selected inorganic and organic materials using first-principles calculations based on Density Functional Theory (DFT), providing a theoretical foundation for their potential applications in next-generation technologies.

#### **Motivation and Research Context**

Materials with tunable electronic and optical properties are at the core of contemporary technologies, including transistors, solar cells, light-emitting diodes (LEDs), photodetectors, and catalysts. The search for new materials with enhanced performance and stability requires a fundamental understanding of their atomic and electronic structures, as well as their interactions with light and charge carriers. First-principles computational methods, particularly those based on DFT, have emerged as powerful tools to investigate material properties without relying on empirical parameters. These techniques allow researchers to predict band structures, optical responses, and thermodynamic stability, guiding experimental efforts in material synthesis and device fabrication.

#### **Objectives of the Thesis**

The main objective of this thesis is to perform a detailed theoretical investigation of different classes of materials, including semiconductors, transition metal halides, and organic crystals. The specific aims are:

- To analyze the fundamental properties of semiconductors, including their band structure, optical behavior, and mechanical properties.
- To develop and implement first-principles computational techniques based on Density Functional Theory (DFT), highlighting the role of exchange-correlation functionals and pseudopotential methods.
- To study the structural stability, electronic properties, and optical response of tungsten chlorides (WCl<sub>x</sub>, x = 3 to 6), which have potential applications in optoelectronics, catalysis, and energy storage.
- To investigate the optical and electronic characteristics of the organic compound  $4C_{16}H_{10}Br_2O_2$ , exploring its feasibility for UV absorption, nonlinear optics, and organic electronic devices.
- To correlate the structural arrangements of these materials with their **electronic** and optical properties, identifying trends that can guide material optimization.

#### Methodology

The study is conducted using Density Functional Theory (DFT), implemented through the CASTEP computational package. This approach involves:

- **Structural Optimization**: Determining the equilibrium lattice parameters and atomic positions to ensure the stability of the studied materials.
- **Electronic Structure Calculations**: Computing the band structure, density of states (DOS), and charge distribution to evaluate electrical and optical behavior.
- Optical Properties Analysis: Deriving key optical parameters such as dielectric function, refractive index, reflectivity, and absorption spectra, which are critical for optoelectronic applications.
- Charge Population Analysis: Investigating the nature of chemical bonding and charge transfer mechanisms to understand material interactions at the atomic level.

#### **Scientific Contributions**

The findings of this thesis contribute to the field of computational materials science by:

- 1. Providing accurate theoretical predictions of structural, electronic, and optical properties of novel materials.
- 2. Establishing a clear link between atomic structure and functional properties, enabling the rational design of materials for optoelectronics, energy conversion, and photonic devices.
- 3. Identifying key trends in semiconductor behavior, particularly in transition metal halides and organic compounds, which can be leveraged for advanced device engineering.
- 4. Expanding the applicability of DFT-based simulations to organic and inorganic systems, validating computational models against available experimental data.

#### **Thesis Organization**

This thesis is structured as follows:

- Chapter I presents a general overview of semiconductor materials, discussing their fundamental physical properties, electronic band structures, optical interactions, and mechanical stability.
- **Chapter II** outlines the theoretical and computational framework, introducing quantum mechanical approximations, Density Functional Theory (DFT), and the CASTEP simulation package.
- Chapter III focuses on the structural, electronic, and optical properties of tungsten chlorides (WCl<sub>x</sub>, x = 3 to 6), emphasizing their potential in optoelectronics and energy applications.
- Chapter IV investigates the organic compound  $4C_{16}H_{10}Br_2O_2$ , analyzing its electronic band structure, charge distribution, and optical absorption characteristics.
- The General Conclusion summarizes the key findings and proposes future research directions for enhancing the performance of the studied materials.

## **Chapter I**

## Generalities on the Fundamental Properties of Semiconductors

#### I.1 Introduction

Materials play a crucial role in various fields and can become increasingly significant in the technological advancements surrounding us. Semiconductor materials, in particular, are at the core of modern electronic and optoelectronic devices. Binary semiconductor compounds, characterized by their adjustable lattice parameters, energy gaps, and optical and dielectric constants, have gained prominence due to their diverse applications.

The understanding of fundamental properties such as structural, mechanical, and elastic behavior, along with the electronic band structure, is essential to assess the potential applications of a given material. Optical properties, specifically direct and indirect electronic transitions—spontaneous and stimulated emission, as well as photon absorption—are of critical importance in semiconductor physics. These properties govern the efficiency of devices such as lasers, light-emitting diodes (LEDs), and photovoltaic cells.

Semiconductor materials, particularly binary compounds, have widespread applications in the development of high-performance optoelectronic devices. These include solar cells, photodetectors, LEDs, and laser diodes, among others. The ability to fine-tune their electronic properties through controlled doping and structural modifications makes them ideal candidates for various technological innovations.

One of the defining characteristics of semiconductors is their ability to modulate conductivity under different conditions. Unlike metals, which exhibit high electrical conductivity due to free electrons, or insulators, which prevent electron flow, semiconductors offer a middle ground where electrical conductivity can be controlled through temperature, illumination, impurities, and external fields. This tunability underpins their functionality in transistors, integrated circuits, and optoelectronic sensors.

Furthermore, advancements in material synthesis techniques have enabled the fabrication of semiconductors with tailored properties. The introduction of new methodologies such as molecular beam epitaxy (MBE) and metal-organic chemical vapor deposition (MOCVD) has allowed for precise control over layer thickness, doping levels, and

crystalline quality. These techniques contribute to the realization of high-efficiency semiconductor-based applications.

The study of semiconductor materials encompasses multiple aspects, including structural, electronic, mechanical, and optical properties. The structural characterization of semiconductors provides insights into their atomic arrangement, lattice constants, and crystallographic orientations, which directly influence their physical behavior. Electronic properties, such as band structure and carrier concentration, determine charge transport mechanisms, while mechanical properties, including elasticity and hardness, dictate the material's robustness under external forces. Optical properties, on the other hand, reveal how semiconductors interact with light, enabling their use in photonic and optoelectronic applications.

This chapter aims to provide an overview of the fundamental properties of semiconductors, exploring their structural, electronic, optical, and mechanical attributes. Through a comprehensive understanding of these aspects, researchers can optimize semiconductor materials for specific applications, paving the way for future advancements in electronic and optoelectronic technologies.

#### I.2 Definition of a Semiconductor and its Electronic Structure

Crystalline materials can be classified into three main categories: insulators, conductors, and semiconductors. Each of these materials exhibits different electrical properties due to variations in their atomic structures and electronic band configurations.

- Insulators have very low electrical conductivity due to a large energy gap between the valence and conduction bands, preventing free charge carriers from forming under normal conditions.
- Conductors (such as metals) have overlapping valence and conduction bands, allowing free electrons to move easily, resulting in high electrical conductivity.
- Semiconductors fall between these two extremes: at absolute zero temperature (T=0 K), they behave like insulators because all electrons remain bound in the valence band. However, as temperature increases, thermal excitation promotes electrons into the conduction band, allowing the material to conduct electricity.

The electrical conductivity  $\sigma$  of semiconductors is within the range:

$$10^{-8}$$
 S/cm  $< \sigma < 10^{3}$  S/cm

For example, silicon (Si) has a conductivity that varies between:

$$10^{-5}$$
 S/cm to  $10^{3}$  S/cm

For comparison, the conductivity of metals is significantly higher:

$$10^3$$
 S/cm  $< \sigma$ (silver:  $10^6$  S/cm)

while insulators exhibit extremely low conductivity:

$$\sigma < 10^{-8} \text{S/cm} (\text{diamond: } 10^{-14} \text{S/cm})$$

These distinct electrical properties are crucial in designing electronic devices, especially for applications in optoelectronics, transistors, and photovoltaic cells [1].

#### **I.2.1 Electrical Conductivity**

Electrical conductivity ( $\sigma$ ) quantifies a material's ability to allow the free movement of electrical charges, facilitating the passage of electric current. The term "semiconductor" suggests an intermediate electrical behavior: it conducts electricity better than an insulator but less effectively than a metal.

The electrical conductivity of a material is influenced by several factors, including:

- Temperature: As temperature increases, more electrons gain sufficient energy to move into the conduction band, increasing conductivity.
- Illumination: Light energy can excite electrons, enhancing conductivity (photoelectric effect).
- Impurity concentration: Doping semiconductors with controlled impurities alters their charge carrier density, significantly modifying conductivity.
- Pressure: High pressure can alter atomic spacing, influencing the band structure and conductivity [2].

The conductivity of a semiconductor at room temperature is illustrated in Figure I.1:

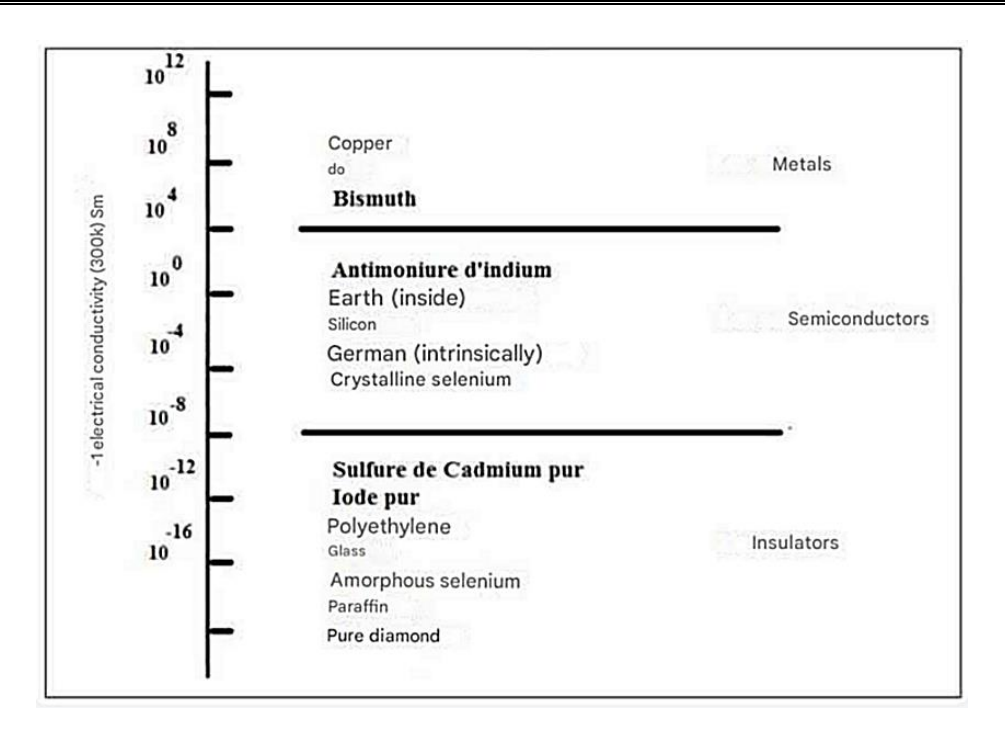


Fig. I.1: Electrical conductivity of various solid materials at ambient temperature.

The boundaries between semiconductors, metals, and insulators are not strictly defined [2].

The temperature dependence of conductivity follows an exponential law. As temperature increases, the conductivity of a semiconductor also increases. The extent of this variation depends on the purity and defect concentration of the material [3].

#### **I.2.2 Energy Bands**

Electrons in an atom occupy discrete energy levels determined by quantum mechanics. In a crystalline solid, these energy levels form continuous energy bands.

The two most important bands in semiconductors are:

- Valence Band (VB): Contains the highest energy electrons bound to atoms.
- Conduction Band (CB): Higher energy states where electrons can move freely, contributing to electrical conduction.

The gap between these bands, called the band gap  $(E_g)$ , is a fundamental parameter that dictates a material's electronic and optical behavior [4].

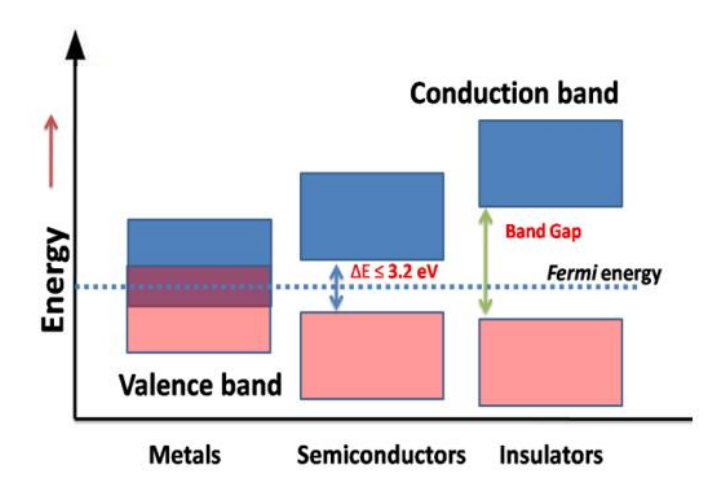


Figure I.2: Band structures of an insulator, semiconductor, and conductor.

- Insulators: Large band gap( $E_g > 3$  eV), preventing electron transitions under normal conditions.
- Metals: Overlapping VB and CB, enabling unrestricted electron movement.
- Semiconductors: Small band gap (0.1 eV <  $E_g$  < 3 eV), where thermal or optical excitation can bridge the gap.

At absolute zero (0 K), semiconductors act as perfect insulators since no electrons can occupy the conduction band. However, even a slight thermal or electrical excitation can generate charge carriers, allowing conduction [5].

#### I.2.2.1 Direct and Indirect Band Gaps

Semiconductors can have either a direct or indirect band gap, depending on how the conduction and valence bands align in momentum space.

- Direct Band Gap: The valence band maximum (VBM) and the conduction band minimum (CBM) are at the same wavevector k. This allows direct electron transitions, making light emission highly efficient (e.g., GaAs, CdTe).
- Indirect Band Gap: The VBM and CBM occur at different momenta, requiring phonon assistance for transitions. This makes light emission less efficient, as in Si and Ge [6].

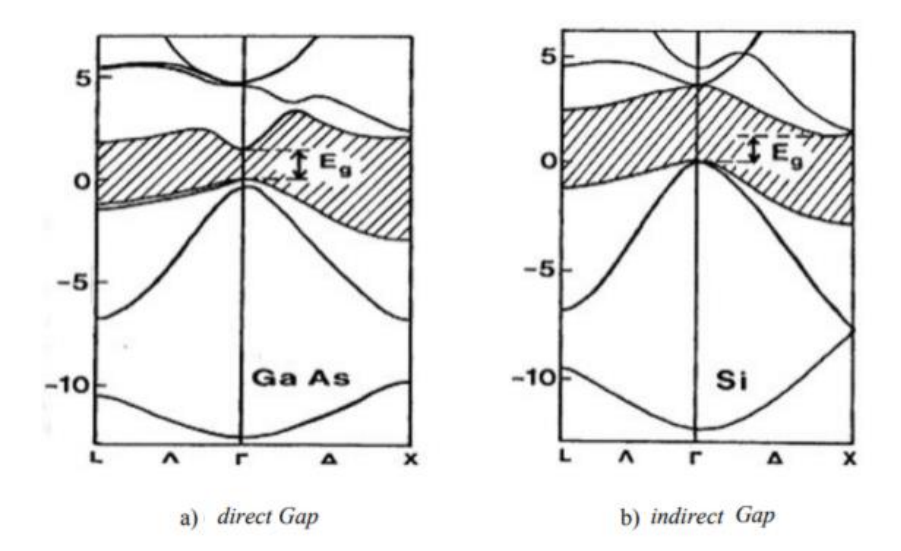


Figure I.3: Direct and Indirect Band Gaps in semiconductors like GaAs and Si [4].

The band gap varies with temperature, described by the Varshni equation [5]:

$$E_g(T) = E_g(0) - \frac{\alpha T^2}{T + \beta} \tag{I.1}$$

where:

- $E_g(0)$  is the band gap at absolute zero,
- $\alpha$  and  $\beta$  are empirical parameters.

#### **I.2.3 Conduction by Electrons and Holes**

In a semiconductor, charge carriers arise when electrons gain enough energy to jump from the valence band to the conduction band. This process leaves behind holes, which behave as positive charge carriers.

- Electrons: Negatively charged, contributing to conduction in the CB.
- Holes: Positively charged, resulting from missing electrons in the VB.

Under an applied electric field, electrons move toward the positive terminal, while holes move toward the negative terminal.

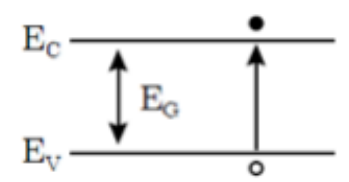


Figure I.4: Electron transition from the valence band to the conduction band [8].

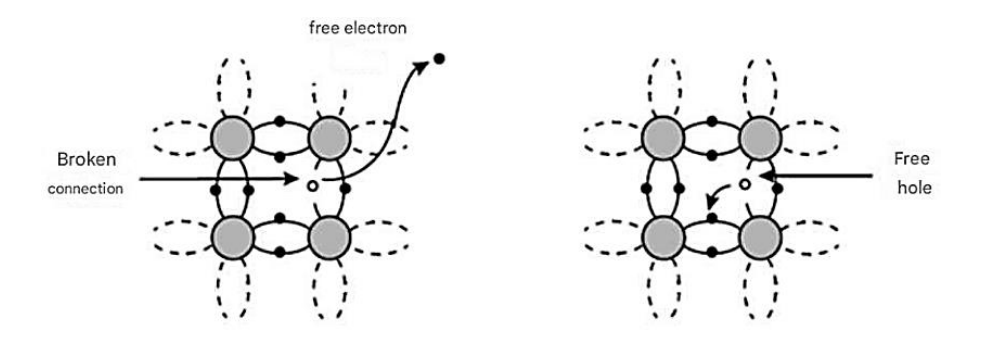


Figure I.5: Formation of an electron-hole pair due to covalent bond breaking [8].

#### **I.2.4 Intrinsic Semiconductors**

An intrinsic semiconductor is a pure material (free of impurities) where charge carriers arise solely from thermal excitation. These materials exhibit high resistivity and are mainly used as base materials for doping.

- Examples: Silicon (Si), Germanium (Ge).
- At high temperatures, intrinsic semiconductors generate equal concentrations of electrons and holes, leading to intrinsic conduction [9].

#### I.2.5 Extrinsic Semiconductors and Doping

To enhance semiconductor performance, doping introduces intentional impurities that modify charge carrier concentrations:

- n-type semiconductors: Doped with donor atoms (e.g., phosphorus in Si), increasing free electrons.
- p-type semiconductors: Doped with acceptor atoms (e.g., boron in Si), increasing hole concentration.

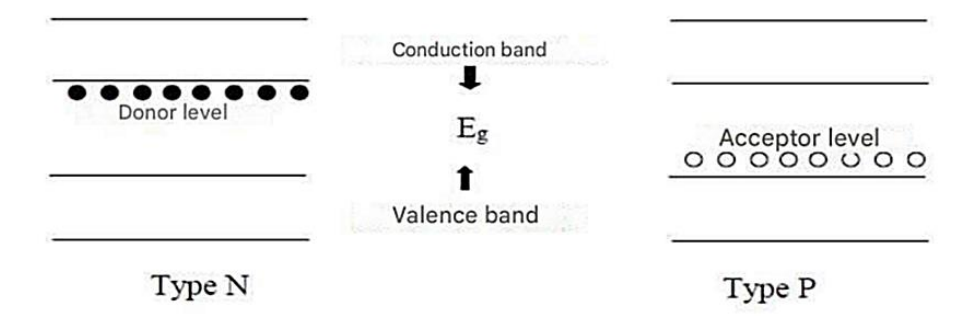


Figure I.6: Band structures of n-type and p-type semiconductors [10].

Doping is essential for semiconductor device fabrication, influencing properties such as band structure engineering, carrier mobility, and electrical conductivity [11].

#### I.3 Structural Properties of Semiconductors

The structural properties of semiconductors play a crucial role in determining their mechanical, electronic, and optical behaviors. Understanding the atomic arrangement, crystal structure, and lattice parameters of a semiconductor is essential for predicting and optimizing its performance in electronic and optoelectronic applications.

Semiconductor materials primarily crystallize in well-defined crystalline structures, which affect their band structure, charge carrier mobility, and interaction with electromagnetic radiation [1].

#### **I.3.1** Crystalline Semiconductors

The crystalline state is characterized by an ordered and periodic arrangement of atoms in three-dimensional space. This periodicity is fundamental in defining a material's electronic properties, particularly its band structure.

A crystal structure consists of a unit cell, which is a repeating pattern of atoms forming the material's lattice. Each unit cell is defined by:

- Lattice parameters: The lengths of the unit cell edges (a, b, c).
- Angles between the edges  $(\alpha, \beta, \gamma)$  [2].

The overall crystal structure of a semiconductor determines its:

- Density
- Mechanical properties (elasticity, hardness)
- Electrical conductivity
- Optical absorption and emission characteristics.

Different semiconductors adopt different crystal structures, influencing their electronic and optical performance.

#### I.3.1.1 Zinc-Blende and Rock Salt Structures

Semiconductors often crystallize in either the Zinc-Blende (ZB) or Rock Salt (RS) structures, both of which are cubic.

#### > Zinc-Blende Structure (ZB)

The Zinc-Blende (ZnS-type) structure is a face-centered cubic (FCC) lattice where each atom is tetrahedrally coordinated (each atom has four nearest neighbors). This structure is common in many III-V and II-VI semiconductors, such as:

- Gallium arsenide (GaAs)
- Zinc telluride (ZnTe)
- Cadmium selenide (CdSe) [3].

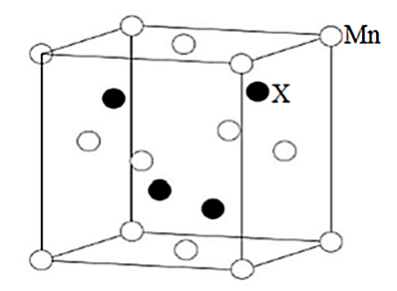


Figure I.7: Representation of the Zinc-Blende (ZB) structure, showing the tetrahedral coordination of atoms [4].

#### ➤ Rock Salt Structure (RS)

The Rock Salt (NaCl-type) structure is another FCC lattice, but with octahedral coordination (each atom has six nearest neighbors). This structure is often found in high-pressure phases of some semiconductors, such as MnTe, MnSe, and MnS, which transition from the Zinc-Blende structure to the Rock Salt structure under pressure [4].

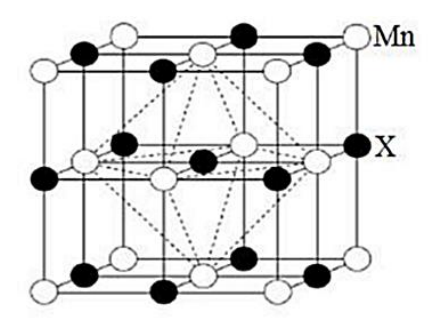


Figure I.8: Representation of the Rock Salt (RS) structure, where empty and filled spheres represent Mn and X atoms, respectively [4].

Under high pressure, certain II-VI semiconductors (such as MnS) undergo a phase transition from the Zinc-Blende structure to the Rock Salt structure, altering their electronic and optical properties [5].

#### **I.3.1.2** Lattice Parameters

Lattice parameters (also called unit cell parameters) describe the dimensions of a crystalline structure. These parameters include:

- Edge lengths (a, b, c) of the unit cell.
- Inter-axial angles  $(\alpha, \beta, \gamma)$ .
- Atomic positions within the unit cell.

For cubic semiconductors (such as Zinc-Blende and Rock Salt structures), the lattice parameter is a single value a, since  $a_i = b = c$  and  $\alpha = \beta = \gamma = 90^\circ$ .

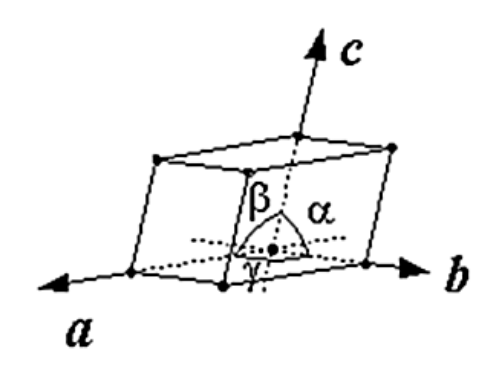


Figure I.9: Illustration of a triclinic unit cell, showing the three edge lengths and angles.

Lattice parameters vary with temperature, pressure, and doping concentration. Precise determination of lattice parameters is essential for calculating:

- Atomic density
- Interatomic distances
- Strain and defects in semiconductor films.

Lattice parameters are typically measured using X-ray diffraction (XRD), neutron diffraction, or electron diffraction techniques [6].

#### I.3.1.3 The Reciprocal Lattice

The reciprocal lattice is a mathematical representation of the periodicity of a crystal in momentum space. It is widely used in solid-state physics to describe:

- Phonon vibrations
- Electron wave propagation
- X-ray diffraction patterns.

For a Zinc-Blende structure, the reciprocal lattice is a Body-Centered Cubic (BCC) lattice, and its first Brillouin zone (the region defining wavevector space) is an octahedron truncated by the six faces of a cube.

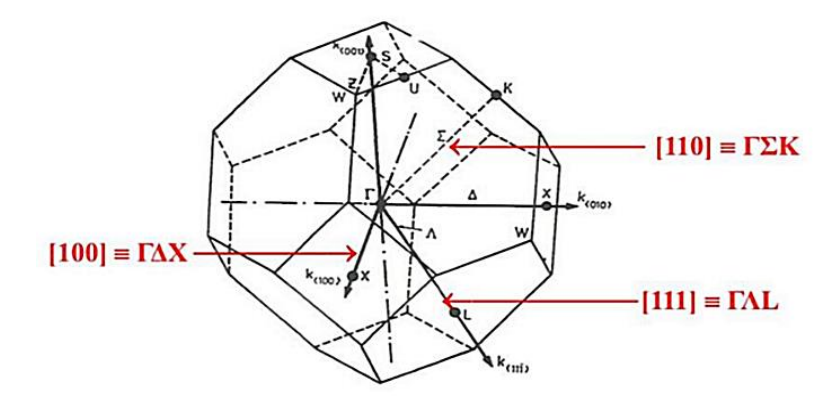


Figure I.10: First Brillouin Zone of a Zinc-Blende Crystal, showing the symmetry directions [8].

Key high-symmetry points in the Brillouin Zone include:

- X  $(2\pi/a, 0, 0)$  along <100> direction
- L  $(\pi/a, \pi/a, \pi/a)$  along <111> direction
- K (0,  $3\pi/2a$ ,  $3\pi/2a$ ) along <011> direction.

Understanding the reciprocal lattice is essential for analyzing electronic band structures and phonon dispersion relations.

#### I.3.2 Influence of Structural Properties on Semiconductor Applications

The crystal structure and lattice parameters of a semiconductor significantly impact its electronic, optical, and mechanical properties.

- Smaller lattice constants lead to stronger interatomic interactions, increasing bandgap energy  $E_G$ .
- Defects and dislocations can alter carrier mobility, impacting semiconductor device performance.
- Heterostructures (materials with different lattice parameters) may experience strain, modifying band structure and optical response [8].

Lattice parameters also determine epitaxial growth compatibility. For instance, GaAs (a = 5.653 Å) and AlAs (a = 5.660 Å) have nearly matching lattice constants, enabling strainfree heterostructures for high-performance optoelectronic devices [9].

#### **I.3.3 Methods for Determining Structural Properties**

Several techniques are used to analyze semiconductor structures, including:

- X-Ray Diffraction (XRD): Measures lattice parameters and phase composition.
- Transmission Electron Microscopy (TEM): Reveals atomic-scale structure.
- Raman Spectroscopy: Identifies vibrational modes influenced by crystal symmetry [10]

Structural characterization helps refine theoretical models of semiconductors and optimize their practical applications.

#### I.4 Optical Properties of Semiconductors

The optical properties of semiconductors play a fundamental role in many applications, including optoelectronics, photovoltaics, sensors, and lasers. The study of how semiconductors interact with electromagnetic radiation provides essential insights into their electronic structure, energy bandgap, and carrier dynamics.

Two primary reasons make the optical properties of semiconductors particularly important:

- 1. Understanding light-matter interaction to explain phenomena such as absorption, reflection, and emission.
- 2. Utilizing these interactions for practical applications in photodetectors, LEDs, lasers, and solar cells [1].

The optical properties of semiconductors are closely related to their electronic structure, specifically the bandgap energy (Eg). These properties dictate how the material absorbs, transmits, and emits light [2].

#### I.4.1 Electromagnetic Waves

An electromagnetic wave consists of two coupled oscillations: an electric field (E) and a magnetic field (B), which oscillate perpendicular to each other and to the direction of propagation.

To generate an electromagnetic wave, two fundamental conditions must be met:

- A charge must exist, creating an electric field.
- The charge must move (current flow), generating a magnetic field.

Together, these oscillations form an electromagnetic wave, which propagates at the speed of light c.

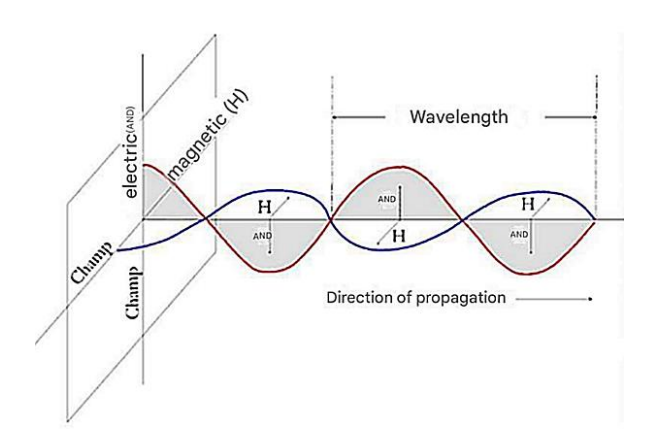


Figure I.11: Electromagnetic wave.

Figure I.10: Schematic representation of an electromagnetic wave, showing the perpendicular orientation of the electric and magnetic fields [3].

Electromagnetic waves are characterized by:

- Wavelength  $\lambda$
- Frequency ν
- Photon energy  $E = h\nu$ , where h is Planck's constant.

#### **I.4.2** The Electromagnetic Spectrum

The electromagnetic spectrum categorizes different types of electromagnetic waves based on wavelength and frequency. It ranges from gamma rays (shortest wavelength, highest energy) to radio waves (longest wavelength, lowest energy).

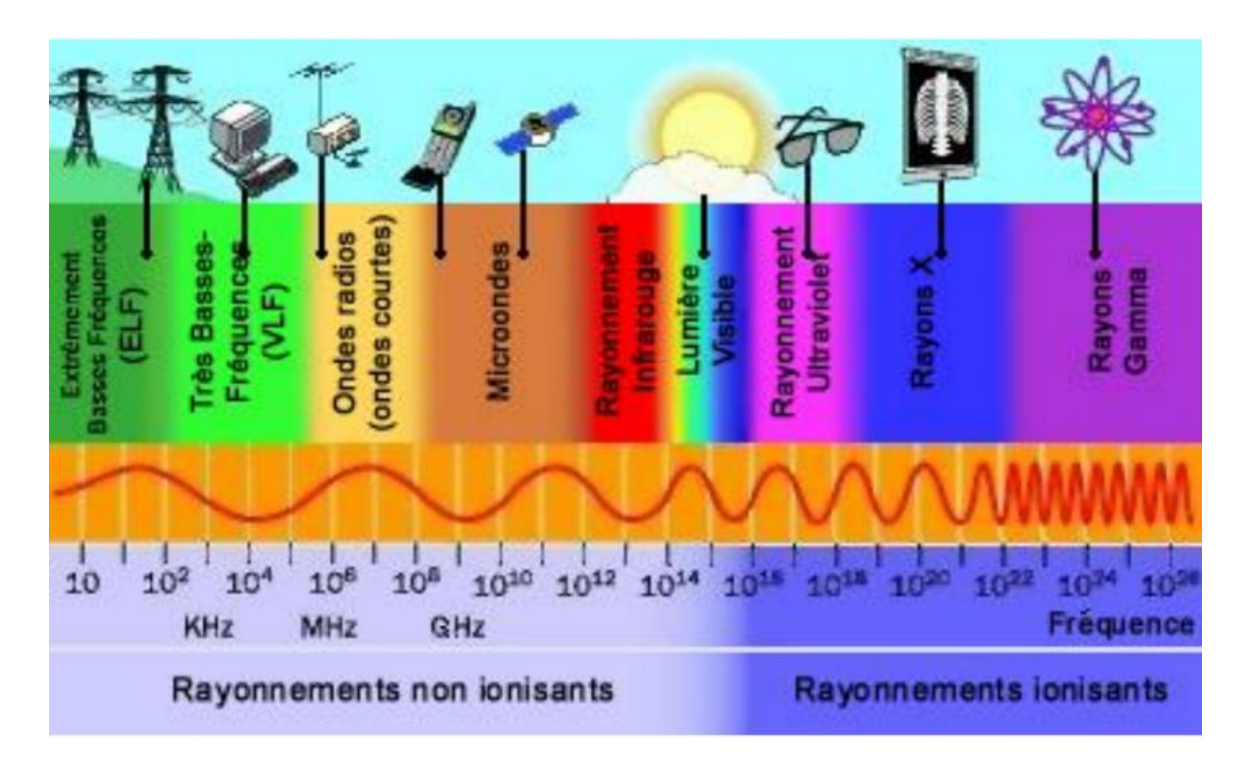


Figure I.12: The electromagnetic spectrum, showing different types of radiation and their applications [4].

Semiconductors typically interact with:

- Infrared (IR): Used in thermal imaging and fiber-optic communication.
- Visible Light: Key for LEDs, lasers, and solar cells.
- Ultraviolet (UV): Important for photodetectors and UV LEDs.

#### I.4.3 Visible Light

The visible spectrum (also called the optical spectrum) consists of light detectable by the human eye, with wavelengths ranging from 380 nm (violet) to 780 nm (red).

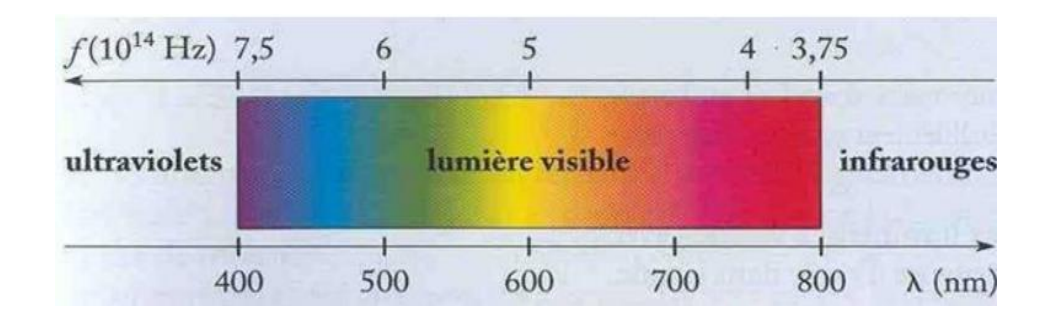


Figure I.13: The visible spectrum, showing the range of wavelengths corresponding to different colors [5].

The ability of a semiconductor to absorb or emit specific wavelengths depends on its bandgap energy. A semiconductor with a large bandgap emits blue or UV light, while a small bandgap material emits red or infrared light [6].

#### I.4.4 Photons and Their Energy

A photon is a quantum of light energy that exhibits both wave-like and particle-like behavior (wave-particle duality). The energy of a photon is given by:

$$E = h\nu = \frac{hc}{\lambda} \tag{I.2}$$

where:

- $h = 6.626 (10^{-34}) \text{ J} \cdot \text{s}$  (Planck's constant),
- $-c = 3.0 (10^8) \text{ m/s (speed of light)},$
- $\lambda$  is the wavelength.

In electron volts (eV), this equation simplifies to:

$$E(eV) = \frac{1.24}{\lambda(\mu m)} \tag{I.3}$$

This relationship is crucial in semiconductor physics, as it links the bandgap energy with the wavelength of absorbed or emitted light [8].

#### I.4.5 Light-Matter Interaction in Semiconductors

When light interacts with a semiconductor, three primary processes occur:

**1. Absorption:** A photon excites an electron from the valence band to the conduction band, creating an electron-hole pair.

- **2. Spontaneous Emission:** An electron recombines with a hole, releasing energy as a photon.
- **3. Stimulated Emission:** A photon induces an excited electron to drop to a lower energy state, emitting a second identical photon (principle of lasers).

#### I.4.5.1 Fundamental Absorption

A semiconductor absorbs photons with energy greater than or equal to the bandgap energy  $E_q$ . This excites electrons to the conduction band, allowing electrical conduction.

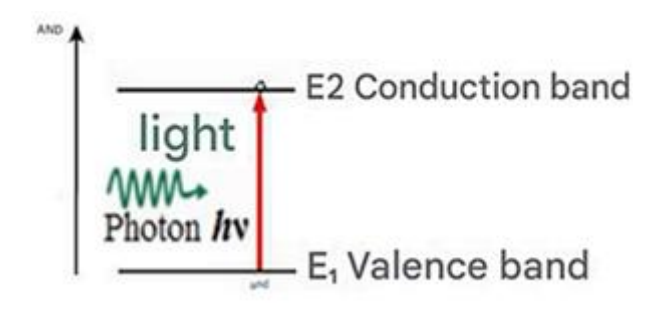


Figure I.14: Absorption process in semiconductors

This process is widely used in solar cells and photodetectors.

#### I.4.5.2 Spontaneous Emission

When an electron in the conduction band recombines with a hole in the valence band, energy is released as light emission. This process forms the basis of LEDs and OLEDs.

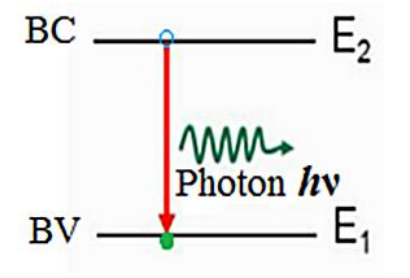


Figure I.15: Spontaneous photon emission in semiconductors

Spontaneous emission is random in direction and phase.

#### I.4.5.3 Stimulated Emission

Stimulated emission occurs when an incoming photon with energy  $E_g$  induces an electron to drop to a lower energy state, releasing an identical photon. This principle is used in lasers, where photons are amplified to produce coherent light.

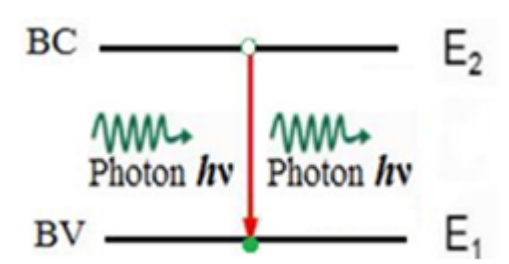


Figure I.16: Stimulated emission mechanism

Unlike spontaneous emission, stimulated emission is directional and phase-coherent, making it ideal for laser technology.

#### I.4.6 Recombination in Semiconductors

Recombination is the process where electrons and holes annihilate, releasing energy. There are two types:

- 1. Radiative Recombination: Releases energy as light (photon emission).
- 2. Non-Radiative Recombination: Releases energy as heat, often through:
  - Auger recombination: Energy is transferred to another charge carrier.
  - Excitonic recombination: Electrons and holes form bound states (excitons).
  - Phonon recombination: Energy dissipates as lattice vibrations [11].

#### I.4.7 Refractive Index

The refractive index (n) determines how light propagates in a semiconductor. It is given by:

$$\tilde{n} = n + ik \tag{I.4}$$

where:

- n is the real part (phase velocity of light),

- *k* is the imaginary part (absorption coefficient).

Higher bandgap semiconductors generally have lower refractive indices. Controlling the refractive index is critical for waveguides, optical fibers, and photonic devices [12].

#### I.4.8 Direct vs. Indirect Optical Transitions

Semiconductors are classified as:

- Direct Bandgap: Electron transitions do not require a change in momentum k. These materials efficiently absorb and emit light (e.g., GaAs, CdTe).
- Indirect Bandgap: Electron transitions require phonon assistance, reducing optical efficiency (e.g., Si, Ge).

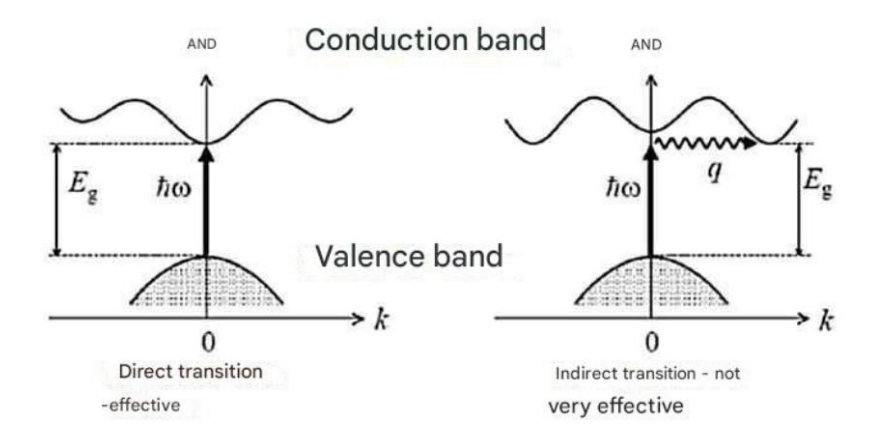


Figure I.17: Direct vs. Indirect optical transitions.

This distinction is crucial for choosing materials for LEDs and lasers.

#### **I.4.9 Semiconductor Colors**

A semiconductor's color is determined by its bandgap energy.

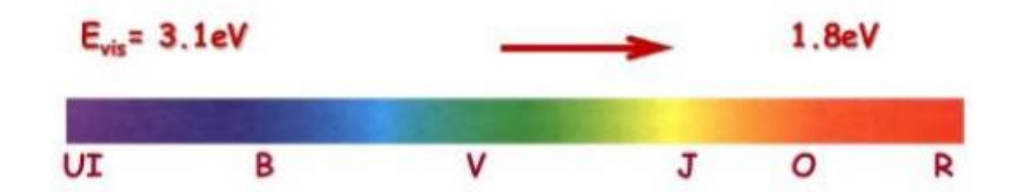


Figure I.18: Intrinsic colors of semiconductors based on bandgap [14].

Doping a semiconductor with impurities can also change its color by introducing defect states.

### I.4.10 Optical Absorption and Transmission

Optical transmission follows Lambert's Law:

$$I = I_0 e^{-\alpha x} \tag{I.5}$$

where:

- $\alpha$  is the absorption coefficient,
- x is the penetration depth.

Materials with large bandgaps are transparent to visible light, while those with small bandgaps absorb lower-energy photons [15].

I will now provide a more detailed and expanded version of Section I.5 "Elastic and Mechanical Properties of Crystalline Solids", ensuring that all subsections, formulas, and references are preserved while adding in-depth explanations, real-world applications, and technical elaboration for improved clarity.

#### I.5 Elastic and Mechanical Properties of Crystalline Solids

The mechanical and elastic properties of crystalline solids are fundamental in understanding their behavior under stress and deformation. These properties govern how a material responds to external forces, withstands mechanical loads, and returns to its original shape once the force is removed. In semiconductor materials, these characteristics are critical as they influence device reliability, fabrication processes, and thermal expansion compatibility in electronic and optoelectronic applications.

The study of mechanical and elastic properties in crystalline solids is essential in both fundamental physics and practical engineering applications. Some key aspects include:

- Atomic interactions and bonding that determine structural stability.
- Mechanical strength and resistance to deformation in semiconductors.
- Influence of mechanical strain on electronic properties in microelectronics.

- Elasticity and mechanical stress management in thin films, MEMS, and nanoelectronics.

For instance, in semiconductor devices, mechanical stress affects charge carrier mobility, band structure, and thermal dissipation, making it crucial to understand and control these properties [1].

The mechanical behavior of materials is largely dictated by their crystal structure, defect density, and interatomic bonding forces. In semiconductors, covalent bonding (such as in silicon and gallium arsenide) results in high stiffness but also brittleness [2].

#### I.5.1 Elastic Behavior of Crystals

Elasticity refers to a material's ability to return to its original shape after being deformed by an applied force. The elastic properties of a solid are determined by the strength of atomic bonds and how the crystal lattice deforms under mechanical loads.

When a force is applied to a crystal, atomic bonds stretch or compress, creating an internal restoring force that opposes the deformation. This interaction follows Hooke's Law for small deformations, where stress is proportional to strain [3].

#### > Types of Atomic Forces in Elasticity

Crystals experience two opposing forces:

- 1. Attractive Forces:
  - Maintain structural cohesion.
  - Arise from covalent, ionic, or metallic bonds.
- 2. Repulsive Forces:
  - Prevent excessive compression.
  - Result from electron cloud overlap.

At equilibrium, these forces balance at an interatomic distance  $d_0$ , defining the stability and mechanical properties of the material.

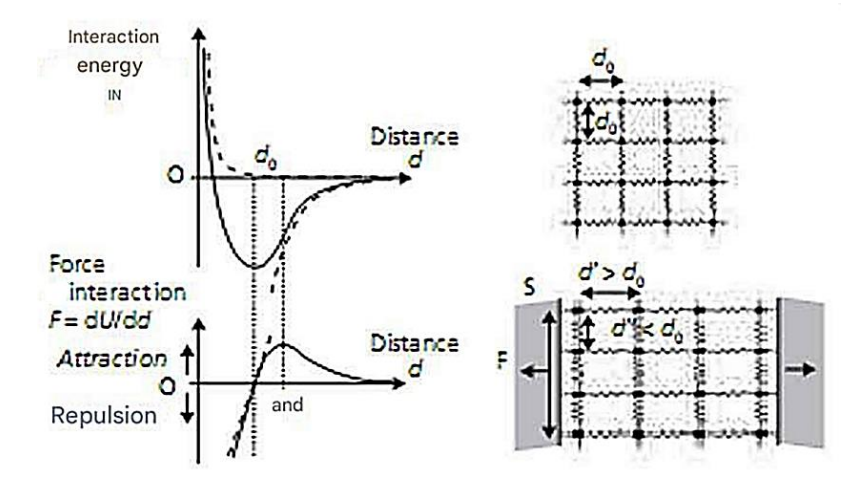


Figure I.19: Variation of energy and force with interatomic distance d [4].

Elasticity is governed by small oscillations around  $(d_0)$ , where atoms act like springs.

#### I.5.2 Stress and Strain: Hooke's Law

The relationship between stress  $\sigma$  and strain  $\epsilon$  describes how a material responds to applied forces.

- Stress  $\sigma$ : Force per unit area applied to a material.
- Strain  $\epsilon$ : Relative change in shape due to applied stress.

For small deformations, the relationship is linear, following Hooke's Law:

$$\sigma_{ii} = E \cdot \epsilon$$
 (I.6)

where:

- E = Young's modulus (elastic constant, in GPa),
- $\sigma_{ii}$  = Stress (Pa or N/m<sup>2</sup>),
- $\epsilon$  = Strain (dimensionless).

Simultaneously, a material undergoes lateral contraction when stretched, described by Poisson's ratio  $\nu$ :

$$\nu = -\frac{\epsilon_{\text{transverse}}}{\epsilon_{\text{axial}}} \tag{I.7}$$

This ratio represents the degree of lateral shrinkage when stretched longitudinally.

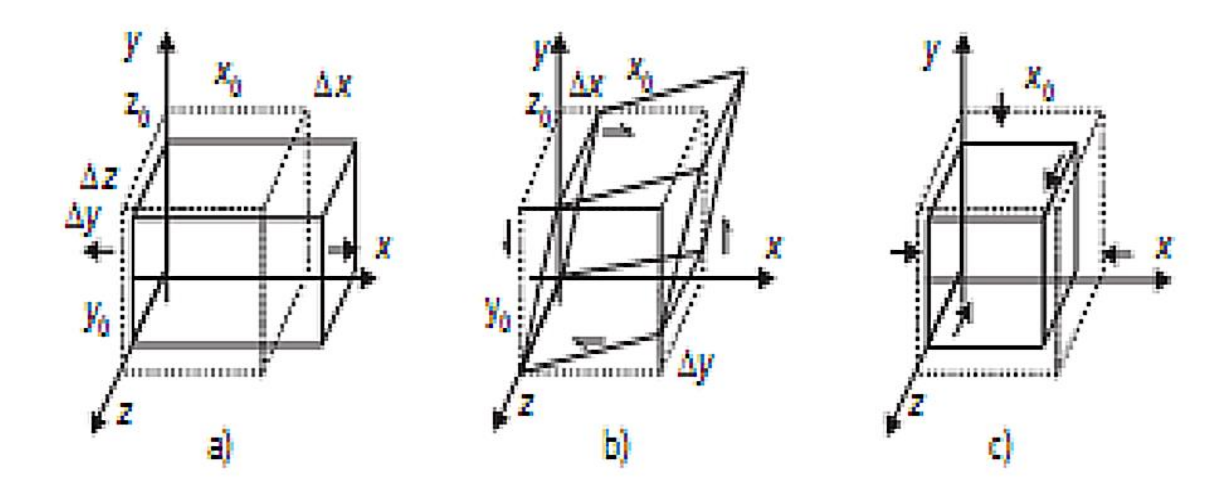


Figure I.20: Various types of elastic deformations [5].

#### I.5.3 Elastic Moduli and Mechanical Constants

Several elastic moduli characterize how materials resist mechanical forces.

# I.5.3.1 Young's Modulus E

Young's modulus measures a material's stiffness:

$$E = \frac{\sigma}{\epsilon} \tag{I.8}$$

- Higher  $E \rightarrow$  Stiff materials (e.g., diamond, silicon carbide).
- Lower  $E \rightarrow$  Flexible materials (e.g., rubber, polymers).

Semiconductors with high Young's modulus are rigid and brittle, making them ideal for microelectronics but challenging for mechanical flexibility [6].

#### I.5.3.2 Bulk Modulus (B)

The bulk modulus (B) measures a material's resistance to uniform compression:

$$B = -V \frac{dP}{dV} \tag{I.9}$$

For cubic crystals:

$$B = \frac{C_{11} + 2C_{12}}{3} \tag{I.10}$$

Materials with high bulk modulus (e.g., diamond, GaN) are used in high-pressure applications.

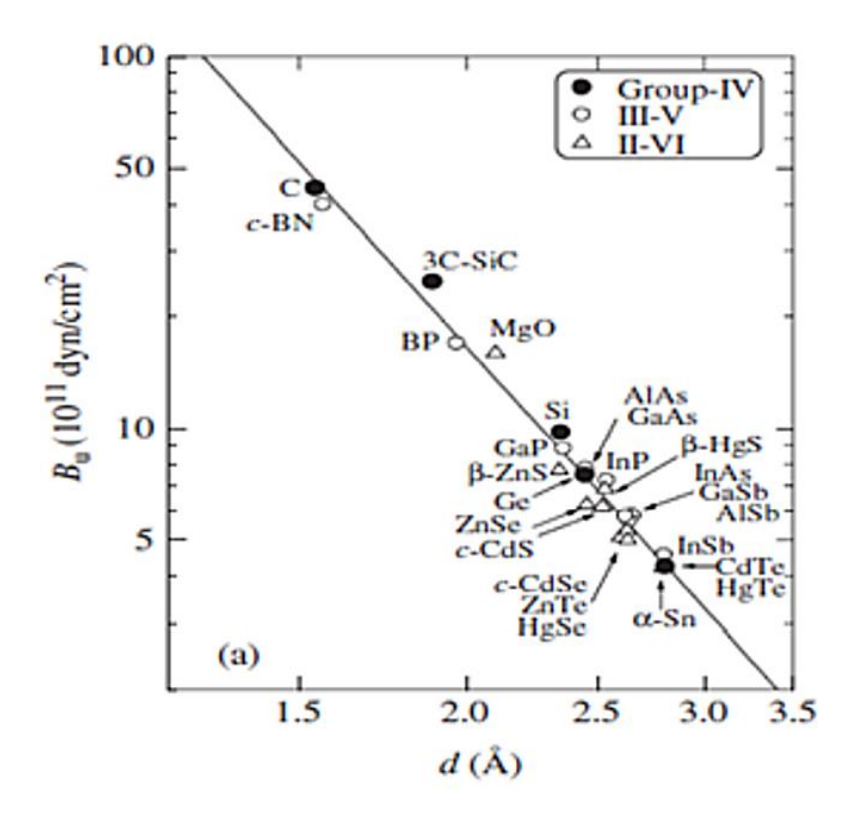


Figure I.21: Bulk modulus variation in different semiconductors [27].

# I.5.3.3 Shear Modulus (G)

The shear modulus (G) measures a material's resistance to shape deformation:

$$G = \frac{\tau}{\gamma} \tag{I.11}$$

For cubic crystals:

$$G = \frac{C_{11} - C_{12}}{2} \tag{I.12}$$

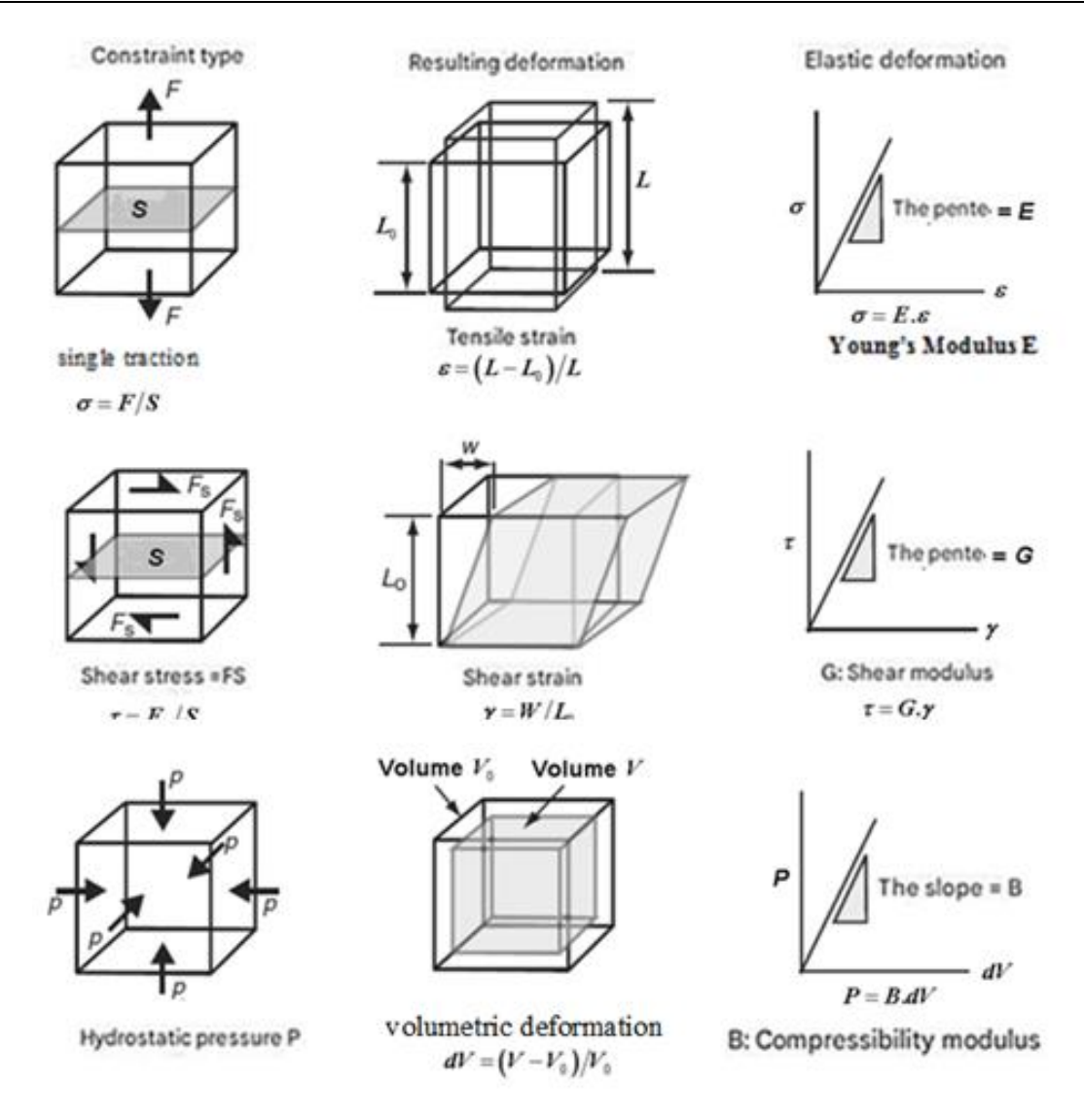


Figure I.22: Shear deformation and mechanical properties [8].

### I.5.4 Elastic Constants and Anisotropy

For anisotropic materials, elasticity is described by a fourth-rank tensor:

$$\sigma_{ij} = C_{ijkl} \epsilon_{kl} \tag{I.13}$$

For cubic crystals, the independent elastic constants are:

- $C_{11}$  Measures stiffness against uniaxial strain.
- $C_{12}$  Describes coupling between perpendicular strains.
- $C_{44}$  Represents shear resistance.

To ensure stability, the following conditions for cubic system must be met:

$$C_{11} - C_{12} > 0, C_{44} > 0, C_{11} + 2C_{12} > 0$$
 (I.14)

Elastic anisotropy impacts fracture toughness and mechanical reliability.

#### I.5.5 Zener Anisotropy Factor and Debye Temperature

The Zener anisotropy factor quantifies elastic anisotropy for cubic system:

$$A_Z = \frac{2C_{44}}{C_{11} - C_{12}} \tag{I.15}$$

- $A_Z = 1 \rightarrow$  Isotropic materials.
- $A_Z \neq 1 \rightarrow$  Anisotropic materials.

Highly anisotropic materials require stress engineering to prevent mechanical failure [9].

# **I.5.6 Debye Temperature** $\theta_D$

The Debye temperature estimates the highest vibrational frequency in a solid:

$$\theta_D = \frac{h}{k_B} \left(\frac{3N}{4\pi V}\right)^{\frac{1}{3}} v_m \tag{I.16}$$

where  $v_m$  is the average sound velocity.

Higher  $\theta_D$  means:

- Better thermal conductivity.
- Lower phonon scattering.
- Higher resistance to thermal stress [10].

#### I.6 Diluted Magnetic Semiconductors (DMS)

The discovery of Diluted Magnetic Semiconductors (DMS) in the 1970s and 1980s opened a new chapter in semiconductor research, introducing magnetism into traditional semiconductors. Unlike conventional semiconductors that rely solely on electron charge transport, DMS materials exploit both charge and spin degrees of freedom, leading to carrier-induced ferromagnetism and novel spintronic functionalities.

The Evolution of DMS Materials

- 1970s: Initial research on II-VI compounds like CdMnTe and ZnMnSe revealed strong magneto-optical effects.

- 1980s: III-V compounds such as GaMnAs demonstrated carrier-mediated magnetic interactions.
- 1990s: The concept of spintronics emerged, leveraging DMS materials for information storage and processing.
- 2000s Present: Research focused on increasing Curie temperature (T<sub>C</sub>) to room temperature, essential for practical applications [1].

DMS materials are now being explored for use in quantum computing, high-density memory, ultrafast spin transistors, and magneto-optical communication systems.

#### I.6.1 Structural, Electronic, and Magnetic Properties of DMS

DMS materials are conventional semiconductors doped with transition metal elements (Mn, Fe, Co, Ni, Cr) that introduce localized magnetic moments into the crystal lattice.

#### **I.6.1.1 Crystal Structures of DMS Materials**

DMS compounds are typically based on the following semiconductor families:

- 1. II-VI DMS (ZnMnSe, CdMnTe, HgMnTe):
  - Exhibits antiferromagnetic superexchange interactions.
  - Used in magneto-optical applications such as Faraday rotators.
- 2. III-V DMS (GaMnAs, InMnSb, GaMnP):
  - Exhibits hole-mediated ferromagnetism.
  - Used in spintronics and magnetic memory devices.
- 3. IV-IV DMS (GeMn, SiMn):
  - High potential for room-temperature ferromagnetism.
  - Suitable for quantum computing and nanoscale spintronic devices [2].

# I.6.2 Theoretical Mechanisms of Magnetism in DMS

DMS materials do not follow conventional ferromagnetic exchange mechanisms. Instead, magnetism arises due to carrier-mediated interactions, governed by exchange coupling between localized spins and charge carriers.

# **I.6.2.1 Exchange Interactions in DMS**

The interaction between magnetic dopants and free carriers is categorized as:

- 1. s-d Exchange Interaction: Coupling between conduction electrons and localized magnetic ions.
- 2. p-d Exchange Interaction: Stronger interaction between valence band holes and magnetic ions.

These interactions significantly modify the electronic band structure, leading to:

- Giant Zeeman Splitting under a magnetic field.
- Anomalous Hall Effect (AHE) caused by spin-dependent scattering.
- Tunable magneto-optical properties [4].

# I.6.2.2 Carrier-Mediated Ferromagnetic Ordering

Unlike conventional ferromagnets, where exchange occurs via direct d-d interactions, DMS materials rely on charge carriers (holes or electrons) to mediate long-range magnetic coupling.

The dominant mechanisms include:

- RKKY Interaction: Long-range oscillatory coupling via conduction electrons.
- Double Exchange Mechanism: Direct hopping of carriers between magnetic sites.
- Superexchange Interaction: Indirect antiferromagnetic coupling via a non-magnetic anion [5].

#### I.6.3 Curie Temperature and its Dependence on Carrier Density

A major challenge in DMS research is achieving room-temperature ferromagnetism  $T_C > 300 \, K$ ). The Curie temperature  $T_C$  in DMS materials is given by:

$$T_C \approx J_{\text{eff}} \cdot x \cdot p^{\frac{1}{3}}$$
 (I.17)

where:

- $J_{\text{eff}}$  = Effective exchange energy.
- x = Magnetic dopant concentration.
- p = Hole concentration.

Experimental  $T_C$  Values in DMS Materials

- GaMnAs:  $T_C \approx 170K$ .
- GeMn:  $T_C \approx 110K$ .
- ZnMnSe: Paramagnetic (no free carriers).

Strategies to Enhance  $T_C$ 

- Optimized doping levels to prevent dopant clustering.
- Strain engineering to modify band alignment.
- Co-doping with additional elements to enhance carrier concentration.

# I.6.4 Optical and Transport Properties of DMS

DMS materials exhibit unique magneto-optical and transport effects, making them ideal for spintronic applications.

# **I.6.4.1 Optical Effects in DMS**

- Giant Faraday and Kerr Effects: Large rotation of polarized light in a magnetic field.
- Magneto-Photoluminescence: Spin-polarized carriers modify luminescence spectra.
- Bandgap Tuning via Magnetic Field: Redshift in absorption edge due to p-d exchange.

# I.6.4.2 Electrical Transport in DMS

- Anomalous Hall Effect (AHE): Arises from spin-polarized carrier scattering.
- Colossal Magnetoresistance (CMR): Strong resistance change with applied magnetic field.
- Spin-Polarized Current Injection: Enables efficient spintronic devices [10].

#### **I.6.5 Applications of DMS in Spintronics**

DMS materials have revolutionized spin-based computing, memory, and sensors.

# **I.6.5.1** Key Spintronic Devices

- 1. Magnetic Tunnel Junctions (MTJ):
  - Used in MRAM (Magnetoresistive Random-Access Memory).
  - Exploits tunneling magnetoresistance (TMR).
- 2. Spin-Field Effect Transistors (Spin-FETs):
  - Controls spin-polarized transport for low-power computation.
- 3. Quantum Computing:
  - DMS-based qubits enable spin-based quantum logic.
- 4. Magneto-Optical Sensors:
  - Detects ultra-low magnetic fields for security and medical diagnostics [11].

#### **I.6.6 Challenges and Future Prospects**

Despite significant progress, several challenges remain:

- Achieving Room-Temperature Ferromagnetism:  $(T_C > 300K)$  is required for commercial applications.
- Controlling Doping Homogeneity: Avoiding dopant clustering and secondary phases.
- Enhancing Spin Injection Efficiency: Crucial for spintronic device integration.

#### I.7. Conclusion

In this chapter, we have provided a comprehensive overview of the fundamental properties of semiconductors, focusing on their structural, electronic, optical, and mechanical characteristics. Semiconductors are unique materials that bridge the gap between conductors and insulators, with electrical properties that can be precisely controlled through temperature, doping, and external stimuli. Their band structure, characterized by direct and indirect energy gaps, governs their optical and electronic behaviors, making them essential for optoelectronic applications such as LEDs, lasers, and photovoltaic cells.

We have also explored the significance of crystal structures, including the Zinc-Blende and Rock Salt configurations, and how structural properties influence mechanical stability, elastic moduli, and material strength. Optical properties, such as light absorption, emission, and refractive index, play a crucial role in semiconductor functionality, particularly in photonic and spintronic devices. Furthermore, the interaction between charge carriers and electromagnetic waves underpins key applications in modern electronics and photonics.

Understanding these properties is crucial for optimizing semiconductor materials for technological advancements, including next-generation transistors, quantum computing, and high-efficiency energy devices. The insights presented in this chapter lay the groundwork for further exploration of semiconductor physics and the development of novel materials tailored for specific applications.

# **Chapter II**

# First-Principles Methods and Computational Details

#### **II.1 Introduction**

Due to its success in describing and predicting material properties, numerical simulation has become an essential tool in various fields, from solid-state physics to molecular chemistry. The rise of increasingly powerful processors has facilitated the implementation of sophisticated computational techniques, enabling better agreement between theoretical predictions and experimental results. In particular, nanomaterials are closely linked to technological advances in microelectronics and nanoelectronics. A deep understanding of material properties is crucial not only for optimizing the fabrication of electronic devices but also for discovering new materials with unique properties.

Ab initio methods aim to predict material properties by solving quantum mechanical equations without relying on empirical parameters. This chapter introduces the theoretical framework used in this work. We begin with a general discussion of the non-relativistic quantum treatment of multi-particle systems, followed by an overview of two major families of quantum calculations: the Hartree-Fock method and the various approximations used to account for exchange and correlation energies. We then introduce density functional theory (DFT), along with other key approximations, including pseudopotentials and the plane wave expansion method. For more details, see the references [7].

#### **II.2 Many-Body Problem and Approximations**

# II.2.1 Schrödinger Equation

A crystalline system consists of a collection of interacting particles (electrons and nuclei). In principle, its properties can be derived from quantum mechanical laws by solving the Schrödinger equation.

The Schrödinger equation is fundamental in theoretical physics and chemistry. It determines the energy levels and wave functions of a system in its stationary states.

For a non-relativistic system composed of  $N_e$  bound electrons, with spatial coordinates  $\vec{r_i}$ , and  $N_N$  nuclei with charge  $Z_N$ , mass  $m_N$ , and spatial coordinates  $\overrightarrow{R_N}$ , the equation takes the form:

$$H_{\Psi_n}(\vec{r_l}, \overrightarrow{R_N}) = E_{n\Psi_n}(\vec{r_l}, \overrightarrow{R_N}) \tag{II.1}$$

where H is the Hamiltonian of the system,  $\Psi_n$  is the wave function associated with energy level  $E_n$ , and n is an integer indicating quantized energy levels.

The Hamiltonian of a crystal, which accounts for electrostatic interactions (attractive or repulsive, depending on particle charge), is given by:

$$H = \frac{-\frac{1}{2} \left( \sum_{i=1}^{N_e} \Delta_i + \sum_{N=1}^{N_N} \frac{\Delta_N}{m_N} \right) + \sum_{i=1}^{N_e} \sum_{j < i} \frac{1}{|\vec{r}_i - \vec{r}_j|} + \sum_{N=1}^{N_N} \sum_{N' < N} \frac{Z_N Z_{N'}}{|\vec{R}_N - \vec{R}_{N'}|} - \sum_{i=1}^{N_e} \sum_{N=1}^{N_N} \frac{Z_N}{|\vec{R}_N - \vec{r}_i|}$$
(II.2)

The Hamiltonian can be decomposed into kinetic and potential energy components:

- Kinetic energy of nuclei:

$$\hat{T}_N = -\frac{1}{2} \sum_{N=1}^{N_N} \frac{\Delta_N}{m_N} \tag{II.3}$$

- Kinetic energy of electrons:

$$\hat{T}_e = -\frac{1}{2} \sum_{i=1}^{N_e} \Delta_i \tag{II.4}$$

- Nucleus-nucleus interaction energy:

$$\hat{V}_{NN'} = \sum_{N=1}^{N_N} \sum_{N' < N} \frac{Z_N Z_{N'}}{\left| \vec{R}_N - \vec{R}_{N'} \right|}$$
(II.5)

- Nucleus-electron attraction energy:

$$\hat{V}_{Ne} = \sum_{i=1}^{N_e} \sum_{N=1}^{N_N} \frac{Z_N}{|\vec{R}_N - \vec{r}_i|}$$
(II.6)

- Electron-electron repulsion energy:

$$\hat{V}_{ee} = \sum_{i=1}^{N_e} \sum_{j < i} \frac{1}{|\vec{r}_i - \vec{r}_j|}$$
 (II.7)

All observable properties of the electron-nucleus system are encoded in equation (II.1). Solving this equation grants access to the system's quantum states and its physical and chemical properties.

However, directly solving the Schrödinger equation for a system containing  $(N_e + N_N)$  interacting bodies is highly complex. Even for a small number of particles, analytical solutions are generally infeasible. To overcome this challenge, various approximations are employed, which we now discuss.

#### **II.2.2** Born-Oppenheimer Approximation

Developed by Born and Oppenheimer in 1927, this approximation exploits the significant mass difference between nuclei and electrons. Since nuclei are much heavier, they move much more slowly compared to electrons. Consequently, nuclear motion can be considered negligible while solving for electronic properties.

For a given nuclear configuration  $\vec{R}_N$ , only the electronic contribution  $E_{el}(\vec{R}_N)$  to the total energy  $E_n$  is relevant for determining system properties. This assumption drastically reduces computational complexity.

With fixed nuclei, their kinetic energy vanishes, and the nucleus-nucleus interaction energy becomes a constant. Under these conditions, the electronic Hamiltonian simplifies to:

$$\widehat{H}_{el} = \widehat{T}_e + \widehat{V}_{ee} + \widehat{V}_{Ne} \tag{II.8}$$

The Born-Oppenheimer approximation, also known as the adiabatic approximation separates, electronic and nuclear motion. This allows the electronic wave function  $\Psi_e$  to be determined independently of nuclear vibrations:

$$\Psi_n(\vec{R}_N, \vec{r}_i) = \Psi_n(\vec{R}_N) \times \Psi_e(\vec{r}_i) \tag{II.9}$$

where:

- $\Psi_n$  is the nuclear wave function.
- $\Psi_e$  is the electronic wave function, corresponding to frozen nuclear positions  $\vec{R}_N$

Thus, the total Hamiltonian is decomposed into electronic and nuclear components. The Schrödinger equation then reduces to:

$$[T_e + V_{ee} + V_{en}]\Psi_e(\vec{R}_N, \vec{r}_i) = E_e(\vec{R}_N) \times \Psi_e(\vec{R}_N, \vec{r}_i)$$
 (II.10)

Due to the complexity of solving this equation directly, further approximations are necessary, as discussed in the following sections.

# II.2.3 Self-Consistent Field Approximation

The self-consistent field (SCF) method is a key approach in quantum mechanics, allowing the treatment of many-electron systems by approximating the interactions within a mean-field framework. Instead of solving the full Schrödinger equation for a system with multiple interacting particles, the SCF method assumes that each electron moves in an effective potential created by the other electrons and the nuclei. This leads to an iterative process where the wave functions and associated potentials are updated until a self-consistent solution is obtained.

The fundamental starting point is the Hartree approximation, where the total wave function is written as a product of single-electron wave functions:

$$\psi_e(\vec{r}_1, \vec{r}_2, \dots, \vec{r}_{Ne}) = \phi_1(\vec{r}_1) \cdot \phi_2(\vec{r}_2) \dots \phi_{Ne}(\vec{r}_{Ne})$$
 (II.11)

Each electron is assumed to move in the mean field of the system, leading to the single-particle Schrödinger equation:

$$\hat{h}_i \phi_i(r) = \epsilon_i \phi_i(r) \tag{II.12}$$

where the single-electron Hamiltonian is defined as:

$$\hat{h}_i = -\frac{1}{2}\Delta + V_{ext}(r) + V_i(r)$$
(II.13)

The Hartree potential, describing the electrostatic interaction between electrons, is given by:

$$V_{i}(r) = \int \frac{\rho_{i}(r')}{|r - r'|} d^{3}r'$$
(II.14)

where the electron density is:

$$\rho_i(r) = \sum_{j \neq i}^{Ne} |\phi_j(r)|^2$$
 (II.15)

By substituting these equations, the Hartree equation for a single electron is obtained:

$$\left(-\frac{1}{2}\Delta + V_{ext}(r) + \int \frac{\rho_j(r')}{|r - r'|} d^3r'\right)\phi_i(r) = \epsilon_i \phi_i(r)$$
 (II.16)

This equation needs to be solved self-consistently since the potential itself depends on the wave functions. However, a major drawback of the Hartree method is that it does not enforce the Pauli exclusion principle, as the total wave function does not account for electron antisymmetry.

To address this issue, the Hartree-Fock method replaces the simple product of wave functions with a Slater determinant:

$$\psi_{e}(r_{1},...,r_{Ne}) = \frac{1}{\sqrt{Ne!}} \begin{vmatrix} \phi_{1}(r_{1}) & \phi_{2}(r_{1}) & ... & \phi_{Ne}(r_{1}) \\ \phi_{1}(r_{2}) & \phi_{2}(r_{2}) & ... & \phi_{Ne}(r_{2}) \\ \vdots & \vdots & \ddots & \vdots \\ \phi_{1}(r_{Ne}) & \phi_{2}(r_{Ne}) & ... & \phi_{Ne}(r_{Ne}) \end{vmatrix}$$
(II.17)

This determinant ensures the correct antisymmetry of the wave function, leading to the Hartree-Fock equations:

$$\left(-\frac{1}{2}\Delta + V_{ext}(r) + \int \frac{\rho_j(r')}{|r - r'|} d^3r' - \sum_{j \neq i}^{Ne} \int \frac{\phi_j^*(r')\phi_j(r)}{|r - r'|} d^3r' \delta_{\sigma_i \sigma_j}\right) \phi_i(r) = \epsilon_i \phi_i(r) \text{(II.18)}$$

where  $\delta_{\sigma_i \sigma_j}$  is the Kronecker delta function, ensuring that electrons with parallel spins experience an additional exchange term. While this method accounts for exchange interactions, it still neglects electron correlation, meaning it does not fully capture interactions between electrons with opposite spins.

To improve upon this, Slater introduced a local exchange potential that approximates the exchange interaction in a computationally efficient way:

$$V_x(r) = -\alpha (\frac{3}{4\pi})^{1/3} \rho^{1/3}(r)$$
 (II.19)

where  $\alpha$  is a dimensionless parameter, and  $\rho(r)$  is the charge density. Setting  $\alpha = 1$  corresponds to a homogeneous electron gas model. This method provides a simplified approach but does not fully account for correlation effects.

While these methods form the basis of quantum chemistry and solid-state physics, they are computationally demanding. Density Functional Theory (DFT) emerged as a more efficient alternative, replacing explicit many-body wave function calculations with functionals of the electron density. The DFT framework, especially in its Local Density Approximation (LDA) and Generalized Gradient Approximation (GGA) forms, significantly reduces computational cost while maintaining reasonable accuracy in electronic structure calculations.

The self-consistent field method remains a fundamental concept in computational quantum mechanics, providing the foundation for electronic structure calculations and material property predictions. By iteratively refining wave functions and potentials, SCF methods offer a practical yet powerful approach to solving quantum mechanical problems in many-electron systems.

#### II.3. Density Functional Theory (DFT)

Density Functional Theory (DFT) has become one of the most widely used methods in quantum calculations for determining the electronic structure of matter, including atoms, molecules, and solids. Unlike traditional ab initio methods, DFT offers a fundamentally different approach to handling electronic correlation, providing a practical alternative to wave function-based methods.

The primary objective of DFT is to replace the complex multi-electron wavefunction with the electron density as the fundamental quantity for calculations. The origins of DFT trace back to the model developed by Thomas and Fermi in the late 1920s. This model suggested that electronic properties could be described in terms of functionals of the electron density, applying local approximations to a homogeneous electron gas. While Thomas and Fermi's approach was an important initial step, it lacked precision for many applications. Notably, it did not account for the exchange energy of an atom, arising from the Pauli exclusion principle, or electronic correlation.

It was not until the mid-1960s, with the contributions of Hohenberg and Kohn, that DFT was placed on a solid theoretical foundation. They formulated and demonstrated two fundamental theorems that established DFT as a rigorous framework for electronic structure calculations. These theorems mathematically formalized the idea that all ground-state properties of a many-electron system are uniquely determined by its electron density.

Before delving into the fundamental principles of Density Functional Theory, it is essential to define the central quantity of this theory: the electron density  $\rho(r)$ .

# **II.3.1 Electronic Density**

Electrons can be described as indivisible and indistinguishable particles. Unlike classical particles, an electron cannot be precisely localized as an individual entity. However, its probability of presence in a given volume element can be estimated, which corresponds to the electronic density  $\rho(r)$ .

Electrons must therefore be considered collectively as an electronic cloud, and the electronic density helps identify the regions in space where electrons are most frequently found. The function  $\rho(r)$  is a positive quantity that depends solely on the three spatial coordinates (x, y, z). This function vanishes at infinity and, when integrated over the entire space, yields (N), the total number of electrons:

$$\begin{cases} \lim_{r \to \infty} \rho(r) = 0\\ \int \rho(r) dr = N \end{cases}$$
 (II.20)

By definition,  $\rho(r)$  represents the probability of finding an electron in an infinitesimal volume dr centered at r. Unlike the wave function, electronic density is an observable quantity.

Several attempts have been made to establish a quantum formalism based on electronic density, arguing that this quantity alone is sufficient to determine the complete properties of an atomic system.

However, it was Hohenberg and Kohn who formulated an exact formalism (free from approximations) through the statement of two theorems, which laid the foundation for Density Functional Theory (DFT).

### II.3.2 Hohenberg-Kohn Density Functional Theory

The approach developed by Hohenberg and Kohn reformulated the density functional theory initially proposed by Thomas and Fermi into a rigorous many-body framework. Their formulation applies to any interacting particle system evolving under an external potential and is based on two fundamental theorems established in 1964.

- **First Theorem:** For an interacting electron system, the external potential  $V_{ext}(\vec{r})$  is uniquely determined, up to an additive constant, by the ground-state electronic density  $\rho_0(\vec{r})$ .

Since  $V_{ext}(\vec{r})$  defines the Hamiltonian  $\hat{H}$ , all ground-state properties of a many-particle system are determined by  $\rho_0(\vec{r})$ .

- **Second Theorem**: There exists a functional  $E[\rho(\vec{r})]$  that expresses the total energy in terms of the electron density, valid for any external potential  $V_{ext}(\vec{r})$ . For a given  $V_{ext}(\vec{r})$ , the ground-state energy is the minimum value of this functional, and the corresponding density  $\rho(\vec{r})$  is the exact ground-state density:

$$E[\rho_0(r)] = \min_{\rho} E[\rho(r)] \tag{II.21}$$

The total energy functional for the ground state is written as:

$$E[\rho(\vec{r})] = F[\rho(\vec{r})] + \int \hat{v}_{ext}(\vec{r})\rho(\vec{r})d^3\vec{r}$$
 (II.22)

where:

- $\hat{v}_{ext}(\vec{r})$  represents the external potential acting on the particles,
- $F[\rho(\vec{r})]$  is the universal Hohenberg-Kohn functional, given by:

$$F[\rho(\vec{r})] = \langle \Psi | \hat{T}_{el} + \hat{V}_{el-el} | \Psi \rangle \tag{II.23}$$

where  $\hat{T}_{el}$  and  $\hat{V}_{el-el}$  are, respectively, the kinetic energy term Kohn - Sham and the electron-electron interaction terms (typically Coulombic).

The **Hohenberg-Kohn theorems** established that the energy functional  $E[\rho(\vec{r})]$  satisfies the variational principle, implying that the total energy is a unique functional of the density and is minimized for the ground-state density of the system. This provides a powerful framework for electronic structure calculations. However, the challenge remains in finding an explicit form for the universal functional  $F[\rho(\vec{r})]$ , particularly for the kinetic energy term. The theorems themselves do not provide any guidance on how to construct this functional, requiring an alternative method to solve this problem.

#### II.3.3 Kohn-Sham Method

To overcome the limitations of the Hohenberg-Kohn approach, Kohn and Sham proposed an alternative perspective. They recognized the importance of having an accurate expression for the kinetic energy term, just as the classical potential energy term (Hartree energy) is well known.

Kohn and Sham introduced the concept of a **non-interacting reference system** that has the same electron density  $\rho(\vec{r})$ . as the true interacting system. By using this reference system, they derived an exact expression for the kinetic energy of a **non-interacting** electron system as a functional of the density.

This reformulation has significant consequences:

- 1. It replaces the N-electron many-body wave function  $\Psi$  with N single-electron wave functions  $\phi_i(r)$ .
- 2. The electronic density is obtained by summing the squared modulus of these single-electron wave functions:

$$\rho(r) = \sum_{i}^{N_e} f_i |\phi_i(r)|^2$$
 (II.24)

where  $f_i$  represents the occupation number of the orbital i, and  $N_e$  is the total number of electrons.

Since these equations are interdependent, they must be solved self-consistently. The Kohn-Sham formulation remains exact within its formalism. However, an essential component, the exchange-correlation functional  $E_{xc}[\rho]$ , must be approximated to make the method practical.

# **II.3.4** Exchange-Correlation Functional Approximations

The exchange-correlation functional  $E_{xc}[\rho]$  plays a crucial role in DFT calculations. Its exact form is unknown, necessitating approximations. The two main types of approximations used in DFT are:

## 1. Local Density Approximation (LDA):

LDA assumes that the system can be locally approximated as a homogeneous electron gas, where the exchange-correlation energy depends only on the local density:

$$E_{xc}^{LDA}[\rho(\vec{r})] = \int \varepsilon_{xc}^{LDA}[\rho(\vec{r})]\rho(\vec{r})d^{3}\vec{r}$$
 (II.25)

# 2. Generalized Gradient Approximation (GGA):

GGA improves upon LDA by incorporating density gradients, providing better accuracy in certain cases, especially for weakly bound systems:

$$E_{xc}^{GGA}[\rho(\vec{r})] = \int \varepsilon_{xc}^{GGA}(\rho, \nabla \rho) \rho(\vec{r}) d^3 \vec{r}$$
 (II.26)

While GGA generally improves bonding properties and total energies, it tends to overestimate bond lengths and still underestimates band gaps in semiconductors and insulators.

#### **II.3.5 Self-Consistency in DFT Calculations**

DFT calculations rely on an iterative self-consistent procedure to solve the **Kohn-Sham equations**. The process follows these steps:

- 1. Initialize the electronic density  $\rho_{in}(\vec{r})$ .
- 2. Determine the effective potential:

$$V_{eff}[\rho(\vec{r})] = V_{ext}(\vec{r}) + V_{H}(\vec{r}) + v_{xc}[\rho(\vec{r})]$$
 (II.27)

3. Solve the Kohn-Sham equations:

$$\left(-\frac{1}{2}\nabla^2 + V_{eff}(\vec{r})\right)\phi_i(\vec{r}) = \epsilon_i\phi_i(\vec{r})$$
 (II.28)

4. Compute the new electron density:

$$\rho_{out}(\vec{r}) = \sum_{i}^{N_e} f_i |\phi_i(\vec{r})|^2$$
 (II.29)

5. Check for convergence. If  $\rho_{in} \approx \rho_{out}$ , the process stops. Otherwise, iterate until self-consistency is achieved.

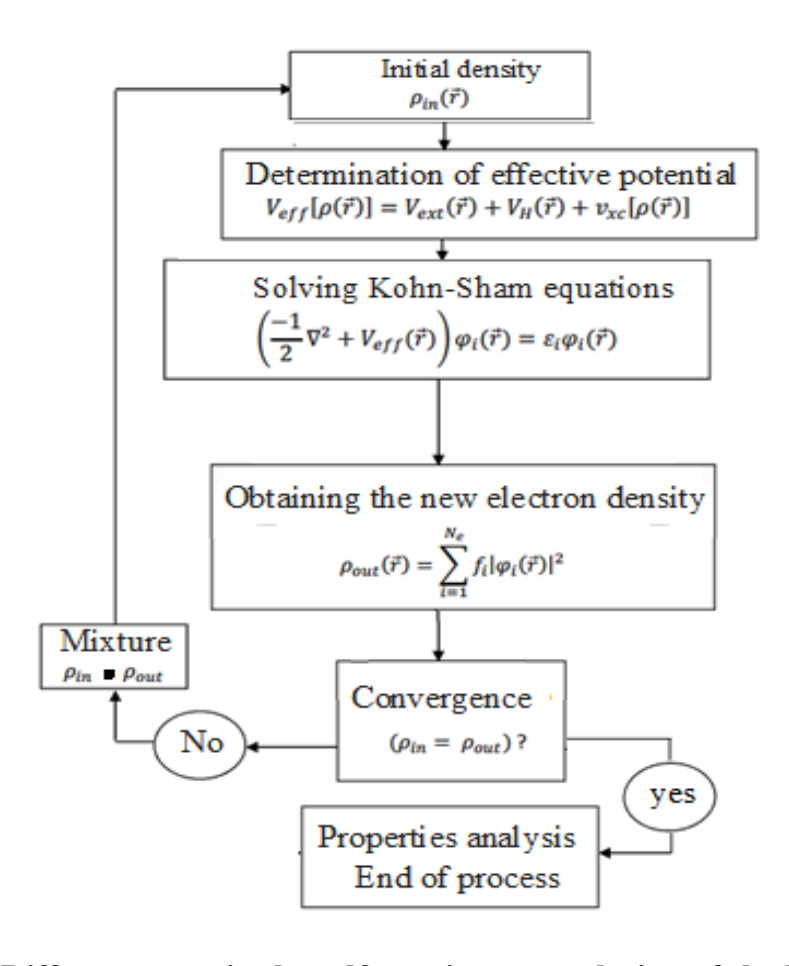


Figure II.1: Different steps in the self-consistent resolution of the Kohm-Sham equations.

#### II.4 Pseudopotential and Plane Wave Methods

In the Kohn-Sham formulation, numerical calculations of the electronic ground state of a system often face additional technical challenges. These challenges become more

significant as the number of electrons in the system increases, particularly in transition metals, where d-orbitals are highly localized.

To minimize computational costs, solving the Kohn-Sham equation within Density Functional Theory (DFT) requires selecting implementation features that define the basis set used for wave functions. This selection includes choosing the external potential, the Hartree potential, and the exchange-correlation potential, which remain relatively independent of boundary conditions and specific basis functions. The kinetic energy treatment also varies depending on whether the system contains light or heavy elements.

A crucial consideration for periodic crystal calculations is the choice of a plane wave basis set and pseudopotential method (PP-PW). This choice allows for an efficient description of wave functions while maintaining computational feasibility. The electrons that follow the Kohn-Sham equation within this framework are referred to as Bloch electrons.

#### II.4.1 Bloch's Theorem and the Plane Wave Approach

In crystalline solids, solving the Schrödinger equation for all electrons within a large atomic system is infeasible. However, for periodic structures, Bloch's theorem simplifies the problem by stating that the wave function of an electron in a periodic potential can be expressed as:

$$\phi_{n_{\vec{k}}\vec{k}}(\vec{r}) = e^{i\vec{k}\cdot\vec{r}}u_{n_{\vec{k}}\vec{k}}(\vec{r})$$
 (II.30)

where:

- $\phi_{nB,\vec{k}}(\vec{r})$  is the wave function of an electron in band nB.
- $\vec{k}$  is the wave vector in reciprocal space.
- $u_{nB,\vec{k}}(\vec{r})$  is a function that has the periodicity of the crystal lattice.

Since  $u_{nB,\vec{k}}(\vec{r})$  is periodic, it can be expanded as a Fourier series in terms of reciprocal lattice vectors  $\vec{G}$ :

$$u_{nB,\vec{\mathbf{k}}}(\vec{r}) = \sum_{\mathbf{G}} C_{nB,\vec{\mathbf{k}}}(\vec{\mathbf{G}}) e^{i\vec{\mathbf{G}}\cdot\vec{\mathbf{r}}}$$
(II.31)

Thus, the total wave function can be rewritten as:

$$\phi_{nB,\vec{\mathbf{k}}}(\vec{r}) = \sum_{\mathbf{G}} C_{nB,\vec{\mathbf{k}}}(\vec{\mathbf{G}}) e^{i(\vec{\mathbf{k}} + \vec{\mathbf{G}}) \cdot \vec{\mathbf{r}}}$$
(II.32)

This formulation allows wave functions to be described in terms of plane waves with coefficients  $C_{nB,\vec{k}}(\vec{G})$ , significantly simplifying electronic structure calculations.

# **II.4.2 Brillouin Zone Sampling**

A key challenge in solid-state physics is the infinite number of k-points in the first Brillouin zone of reciprocal space. To perform practical electronic structure calculations, it is necessary to discretize the Brillouin zone and select a representative set of k-points.

The Monkhorst-Pack method is a widely used scheme for Brillouin zone sampling. It selects k-points in a way that optimally represents the electronic structure while minimizing computational cost. This technique is crucial for computing properties such as band structures and density of states (DOS).

# II.4.3 Cut-off Energy $E_{\text{cut-off}}$

To make Bloch's theorem computationally feasible, the plane wave basis set must be truncated. Instead of including an infinite number of plane waves, only those with kinetic energy below a certain threshold, known as the cut-off energy  $E_{\text{cut-off}}$ , are retained:

$$\frac{\hbar^2}{2m}|\vec{\mathbf{k}} + \vec{\mathbf{G}}|^2 \le E_{\text{cut-off}} \tag{II.33}$$

where:

 $\vec{\mathbf{G}}$  is the reciprocal lattice vector

**k** is the plane wave vector

The cut-off energy determines the number of plane waves included in the expansion. The higher  $E_{\rm cut-off}$ , the more plane waves are used, leading to greater accuracy but also increased computational cost.

The number of plane waves  $N_{pw}$  included in the basis set can be estimated as:

$$N_{\rm pw} \approx N_k \times \frac{1}{2\pi^2} \Omega E_{\rm cut-off}^{\frac{3}{2}}$$
 (II.34)

where:

- $N_k$  is the number of sampled k-points in the Brillouin zone.
- $\Omega$  is the volume of the unit cell.

Choosing an appropriate cut-off energy is critical for balancing accuracy and computational efficiency. A higher cut-off energy leads to more accurate total energy calculations, but also requires significantly greater computational resources.

The pseudopotential and plane wave methods provide an efficient and systematic approach to solving electronic structure problems within Density Functional Theory (DFT).

- Bloch's theorem reduces the complexity of periodic systems by expressing wave functions as plane waves.
- Brillouin zone sampling ensures that only a finite set of k-points is used for electronic structure calculations.
- Cut-off energy selection determines the accuracy and computational cost of the calculation.

These methods, when implemented correctly, form the foundation of many modern electronic structure codes, including CASTEP, VASP, and Quantum ESPRESSO.

# **II.5 Pseudopotential Method**

Pseudopotentials play a crucial role in solid-state calculations and are closely linked to density functional theory (DFT), which has been developed over the past fifty years and has yielded excellent results.

The pseudopotential technique, first introduced by Fermi (1934), has proven highly effective in investigating and understanding the electronic properties of solids. Hellman [32] later proposed a pseudopotential approximation to obtain energy levels of atoms in

alkali metals. Several other suggestions [33, 34, 35] appeared in the solid-state literature, but it was in the 1950s that its use became widespread, particularly due to the work of Phillips and Kleinman [36] in 1959, who based their approach on the orthogonalized plane wave (OPW) method. Over the following decades, the pseudopotential method evolved rapidly and demonstrated its capabilities for predicting various physical properties [37-40]. Below, we provide an overview of the pseudopotential approximations, which are based on the fact that a solid's physical properties are determined primarily by its valence electrons.

## **II.5.1 Frozen Core Approximation**

This method consists of freezing core electrons while explicitly treating valence electrons, which behave like free electrons. In Kohn-Sham equations, the effective potential is replaced by a weaker pseudopotential that represents the potential felt by valence electrons, accounting for core electron screening. The valence electron wave functions are replaced by pseudowave functions. This approach reduces the number of electrons and plane waves required for calculations.

Core electrons are localized around nuclei and are considered chemically inert. The combination of these electrons with nuclei forms rigid ions, known as the frozen core approximation [41].

#### **II.5.2** Phillips-Kleinman Formulation

In 1959, Phillips and Kleinman developed the first formal (non-empirical) approach to pseudopotentials by reformulating the orthogonalized plane wave (OPW) method [42] proposed by Herring in 1940 [43]. In this method, valence wave functions are orthogonal to core states.

In the Phillips-Kleinman method, valence wave functions (single-particle) with energy  $\varepsilon_v$  are given by:

$$\varphi_v = \varphi_{ps} - \sum_i \langle \varphi_{ci} | \varphi_{ps} \rangle \varphi_{ci}$$
 (II.35)

where  $\varphi_{ci}$  is the core wave function with energy  $\varepsilon_{ci}$ , and  $\varphi_{ps}$  is the pseudo-wave function.

The wave function  $\varphi_v$  satisfies the Kohn-Sham equation:

$$\left(-\frac{1}{2}\Delta_i + V_{eff}\right)\varphi_i = \varepsilon_i\varphi_i \tag{II.36}$$

which leads to:

$$\left(-\frac{1}{2}\Delta_i + V_{ps}^{PK}\right)\varphi_{ps} = \varepsilon_v \varphi_{ps} \tag{II.37}$$

The modified potential  $V_{ps}^{PK}$  is called the Phillips-Kleinman pseudopotential and is defined as:

$$V_{ps}^{PK} = V_{eff}(\vec{r}) + \sum_{i} (\varepsilon_{v} - \varepsilon_{ci}) |\varphi_{ci}\rangle \langle \varphi_{ci}|$$
 (II.38)

where  $\sum_{i} |\varphi_{ci}\rangle\langle\varphi_{ci}|$  is the projection operator on core states.

#### **II.5.3 Pseudopotential Construction**

Pseudopotential methods are classified into two categories based on how pseudo-wave functions are developed:

- 1. Norm-conserving methods
- 2. Ultrasoft methods

Pseudopotentials must satisfy several criteria:

- Additivity: The total potential should be the sum of individual pseudopotentials for multiple atoms.
- Transferability: The same pseudopotential should be usable in different chemical environments.
- Computational efficiency: The pseudopotential should require fewer plane waves than an all-electron calculation.

#### II.5.3.a Norm-Conserving Pseudopotentials

Norm-conserving pseudopotentials were a significant step in efficiently handling core electrons. The norm that must be conserved is the charge within the cutoff radius  $r_c$ . The wave function is defined by three quantum numbers (n, l, m):

$$\varphi_{n,l,m}(\vec{r},\theta,\phi) = R_{n,l}(\vec{r})Y_{l,m}(\theta,\phi) \tag{II.39}$$

where  $R_{n,l}(\vec{r})$  is the radial part of the atomic orbital and  $Y_{l,m}$  are the spherical harmonics.

#### II.5.3.b Ultrasoft Pseudopotentials

Ultrasoft pseudopotentials, developed by Vanderbilt [46], do not conserve norm, allowing for larger cutoff radii. This reduces the number of plane waves required while maintaining accurate electronic density:

$$\rho(r) = \sum_{i} \left\{ |\varphi_{i}(\vec{r})|^{2} + \sum_{n,m,N} Q_{nm}^{N}(r) \langle \varphi_{i} | \beta_{n}^{N} \rangle \langle \beta_{m}^{N} | \varphi_{i} \rangle \right\}$$
(II.40)

where  $\beta_n^N$  functions describe localized augmentations in core regions.

Vanderbilt's pseudopotentials have been implemented in CASTEP, the software used in this thesis.

#### **II.6 Introduction to CASTEP Code and Calculation Details**

#### **II.6.1 Overview of CASTEP Calculation Code**

Several calculation codes based on DFT exist, such as Dmol3 [47], VASP [48], ABINIT [49], CRYSTAL [50], and Big DFT [51]. In this work, we use the CASTEP (Cambridge Serial Total Energy Package) code, originally developed in 1988 by Payne et al. [52, 53]. CASTEP is an ab initio calculation code that is part of the Materials Studio software suite, commercialized by Accelrys. It is a state-of-the-art quantum mechanics program designed specifically for solid-state materials science.

CASTEP employs pseudopotential-based Density Functional Theory (DFT) to perform first-principles quantum mechanics calculations that explore the properties of crystals and surfaces in materials such as semiconductors, ceramics, metals, and zeolites. Typical applications involve studies of surface chemistry, structural properties, band structure, density of states, and optical properties. CASTEP can also be used to analyze the spatial distribution of charge density and wave functions within a system. Additionally, CASTEP calculates the full tensor of second-order elastic constants and related mechanical properties of a crystal, such as Poisson's ratio, Lamé constants, and bulk modulus.

CASTEP utilizes periodic boundary conditions (PBCs), Brillouin zone (BZ) integration, a plane wave basis set, and pseudopotentials to compute the total energy of a system. The electronic wave functions are expanded in a plane wave basis, defined using Bloch's theorem and periodic boundary conditions.

In CASTEP, only Kohn-Sham orbitals with wave vectors in the irreducible part of the Brillouin zone are computed since the electronic density can be constructed from these states using symmetry operations. The use of symmetry significantly reduces computation time, especially for small unit cells containing numerous k-points. CASTEP efficiently parallelizes calculations based on k-points. Atomic forces, stress tensors, atomic displacements, and lattice parameter variations are always symmetrized.

### **II.6.1.1 Geometric Optimization with CASTEP**

Geometric optimization is a crucial step in theoretical studies of molecules and solids, allowing refinement of a system's periodic geometry to obtain a stable structure. The optimized structure is determined by minimizing forces and stress tensors until they fall below predefined convergence tolerances. Atomic forces are computed using the Hellmann-Feynman theorem, enabling the determination of equilibrium positions for nuclei and lattice parameters that minimize the system's total static energy.

CASTEP performs geometric optimization self-consistently using the Broyden-Fletcher-Goldfarb-Shanno (BFGS) algorithm [52-53]. This method is the fastest way to find the lowest-energy structure and is the only optimization scheme supporting cell optimization in CASTEP. This procedure is essential for obtaining molecular or crystalline structures and static energies comparable to experimental values.

# II.6.1.2 Convergence in Cutoff Energy and k-Point Sampling in CASTEP

The first step in a first-principles calculation for a given material is selecting two essential technical parameters:

- 1. The k-point sampling density in reciprocal space.
- 2. The plane wave basis set size defined by the cutoff energy.

The basis set size is considered sufficient when the total energy reaches a plateau as a function of cutoff energy. Since the electronic density varies rapidly near atoms due to

highly localized core electrons, pseudopotentials are required to reduce the basis set size while ensuring total energy convergence. Ultrasoft pseudopotentials allow for a lower cutoff energy, optimizing the balance between computational cost and accuracy.

The k-point density depends on the system's size and symmetry. A trade-off must be found between computational time and the number of k-points required for energy convergence. CASTEP uses the Monkhorst-Pack method [49] for uniform k-point sampling across the reciprocal space. System symmetry reduces the number of k-points needed in the primitive cell.

# II.6.1.3 Band Structure and Density of States Diagrams

#### **Electronic Band Structure**

In periodic systems, band energies vary with k. Energy minima and maxima generally occur at high-symmetry points and along high-symmetry paths in the Brillouin zone. The electronic band structure is computed by evaluating Kohn-Sham orbitals along these symmetry paths.

The energy dispersion curve E(k) represents the electronic band structure, where each k-point is associated with an eigenvalue of a given band. The band gap computed using Kohn-Sham eigenvalues in LDA and GGA approximations is typically underestimated compared to experimental values.

#### **Electronic Density of States (DOS)**

The total (TDOS) and partial density of states (PDOS) are essential analysis tools. The TDOS provides a histogram of electronic states as a function of energy. PDOS projections onto atomic orbitals help identify the orbital character (s, p, d, or f) of each band.

For spin-polarized systems, spin-up and spin-down DOS can be distinguished. Their sum yields the TDOS, while their difference defines the spin density of states (SDOS). DOS analysis aids in interpreting experimental spectroscopy and understanding electronic structure changes under external pressure.

#### **II.6.1.4 Optical Properties Computation in CASTEP**

The interaction of electromagnetic waves with a material is described by a complex refractive index:

$$\tilde{n} = n + ik \tag{II.41}$$

where k relates to the absorption coefficient  $\alpha$ :

$$\alpha = \frac{2k\omega}{c} \tag{II.42}$$

The reflection coefficient for normal incidence is:

$$R = \left| \frac{1 - \tilde{n}}{1 + \tilde{n}} \right|^2 = \frac{(n - 1)^2 + k^2}{(n + 1)^2 + k^2}$$
 (II.43)

Optical calculations are often performed by computing the complex dielectric function:

$$\varepsilon = \varepsilon_1 + i\varepsilon_2 = \tilde{n}^2 \tag{II.44}$$

where:

$$\varepsilon_1 = n^2 - k^2, \varepsilon_2 = 2nk \tag{II.45}$$

The optical conductivity is given by:

$$\sigma = \sigma_1 + i\sigma_2 = -i\frac{\omega}{4\pi}(\varepsilon - 1) \tag{II.46}$$

The loss function, describing the energy lost by an electron passing through a dielectric, is:

$$Im(\frac{-1}{\varepsilon(\omega)}) \tag{II.47}$$

#### **II.6.2** Calculation Method and Parameters

All calculations in this work use the plane-wave pseudopotential method (PP-PW) [28]. within DFT, as implemented in CASTEP. Vanderbilt-type ultrasoft pseudopotentials [46] from the Materials Studio library are used. Exchange-correlation interactions are treated with the LDA Ceperley-Alder [19] parameterized by Perdew-Zunger [18] and the GGA-PBE approximation [23]. Structural optimizations are performed using the BFGS minimization technique [52]. Spin polarization is considered in calculations. Elastic constants are computed using the finite-strain method [53]. Structural parameters such as

lattice constants, bulk modulus, and pressure derivatives are obtained from the total energy versus volume using the Murnaghan equation of state [54].

#### II.7. Conclusion

In this chapter, we have provided a comprehensive overview of the theoretical and computational methodologies employed in this study. Starting from the fundamental principles of quantum mechanics, we introduced the many-body problem and the necessary approximations that allow for practical calculations of electronic structures. The Born-Oppenheimer approximation, self-consistent field method, and Hartree-Fock theory laid the groundwork for more sophisticated approaches, such as Density Functional Theory (DFT).

DFT has been established as a powerful and widely used technique for studying material properties due to its balance between computational efficiency and accuracy. We detailed the fundamental theorems of DFT and the Kohn-Sham formulation, emphasizing the role of exchange-correlation functionals and the necessity of approximations like the Local Density Approximation (LDA) and Generalized Gradient Approximation (GGA).

Furthermore, we discussed the practical implementation of DFT using plane-wave basis sets and pseudopotentials, which significantly reduce computational complexity while maintaining accuracy. The role of Bloch's theorem, Brillouin zone sampling, and energy cut-off criteria were explored to highlight the critical aspects of numerical convergence in first-principles calculations. Additionally, the pseudopotential method was examined, emphasizing its contribution to reducing computational cost without compromising the accuracy of electronic structure calculations.

Finally, we introduced the CASTEP code as the primary computational tool used in this work, detailing its capabilities in performing structural optimizations, electronic band structure calculations, density of states analysis, optical property evaluations, and elastic constant computations. These methodologies form the foundation for the subsequent chapters, where they will be applied to investigate the physical properties of the studied materials.

# **Chapter III**

# Optical, Structural and Electronic properties of WClx (x = 3 to 6)

#### **III.1 Introduction**

Tungsten hexachloride (WCl<sub>6</sub>) is an essential compound in the family of tungsten chlorides, playing a crucial role in various applications, including chloride-ion batteries, catalysis, and thin-film deposition technologies. As a transition metal halide, tungsten chlorides exhibit complex structural, electronic, and optical properties, making them intriguing subjects for both fundamental and applied research. Their ability to undergo polymorphic transformations under varying conditions of temperature and pressure further enhances their technological relevance. The study of the phase diagram of the W-Cl system carried out by H. Okamoto [2] is illustrated in Figure III.1. The phase diagram is presented to show the effect of temperature and concentration on the present phases structure of the alloy at constant pressure, where an equilibrium state corresponds to the minimum value of free energy.

Tungsten chlorides are known for their high thermal and chemical stability, which makes them suitable for high-performance coatings, optical devices, and advanced energy storage technologies. Among the different tungsten chlorides, WCl<sub>6</sub> is particularly interesting due to its molecular geometry and electronic configuration, which significantly influence its physicochemical properties. Additionally, lower tungsten chlorides, such as WCl<sub>5</sub>, WCl<sub>4</sub>, and WCl<sub>3</sub>, exhibit distinct electronic structures and reactivities that contribute to their diverse industrial applications, including their use as precursors in chemical vapor deposition (CVD) processes.

The phase diagram of the W-Cl system, established through experimental investigations, has identified multiple crystalline forms of WCl<sub>6</sub>, primarily the  $\alpha$ -WCl<sub>6</sub> and  $\beta$ -WCl<sub>6</sub> polymorphs. These polymorphs, characterized by different space groups (R- $\overline{3}$  and P- $\overline{3}$ m1), undergo structural transformations at elevated temperatures, affecting their stability and functional properties. Understanding these phase transitions at the atomic level is essential for tailoring tungsten chlorides for specific technological applications. Additionally, their electronic behavior is influenced by the degree of hybridization between tungsten d-orbitals and chlorine p-orbitals, impacting their conductivity and optical properties. Inorganic tungsten WCl<sub>3</sub> is a brown solid obtained by chlorination of tungsten chloride [21].

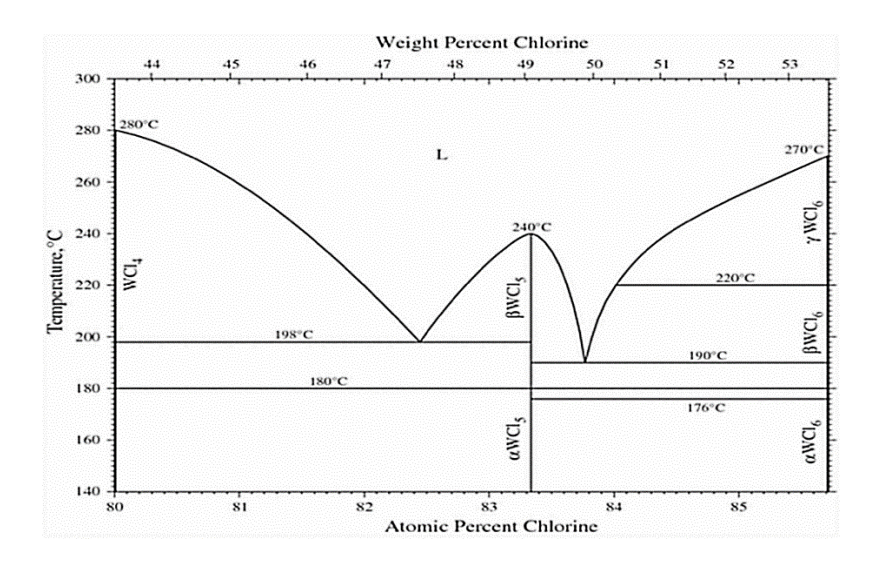


Figure III.1. The region 80 to 86 atomic Cl % of the phase diagram for the W-Cl system [2].

Despite the extensive experimental work on tungsten chlorides, theoretical insights into their fundamental properties remain limited. First-principles calculations based on Density Functional Theory (DFT) provide an efficient approach for investigating the electronic and optical behavior of these materials with high accuracy. In this study, we employ DFT calculations within the Generalized Gradient Approximation (GGA-PBESOL) framework to systematically analyze the structural, electronic, and optical properties of  $WCl_x$  (x = 3, 4, 5 and 6). By optimizing the molecular and crystalline structures, we aim to establish a correlation between the atomic arrangement and the material's electronic and optical characteristics. These calculations allow us to probe the stability, energy band structures, and density of states (DOS), which are fundamental in understanding the electronic transitions governing their functional behavior.

The investigation extends to the determination of band gaps, density of states (DOS), charge transfer mechanisms, and optical response functions, including reflectivity, refractive index, and absorption spectra. These properties are critical for evaluating the suitability of tungsten chlorides in optoelectronic and photonic applications. The strong correlation between structural parameters and optical properties enables the identification of optimal conditions for enhancing light absorption and emission, which is crucial in materials designed for photovoltaic and photonic applications. Additionally, our analysis considers the impact of external factors, such as temperature and pressure, on the stability

and performance of these materials, providing deeper insight into their robustness under different operational conditions.

Furthermore, understanding the effect of tungsten valence states and bonding environments within different chlorides helps in tailoring their properties for specific uses. The ability to fine-tune electronic states through compositional modifications and external perturbations such as strain and doping broadens their application range. These insights contribute significantly to the exploration of novel tungsten halide materials for emerging technologies, including flexible electronics, transparent conductors, and light-harvesting systems.

This work provides valuable insight into the stability and functionality of tungsten chlorides, contributing to the broader field of transition metal halides. The findings are expected to aid in the design of new materials with tailored electronic and optical properties, further advancing their potential applications in energy storage, catalysis, and electronic device fabrication. Ultimately, this study bridges the gap between theoretical predictions and experimental findings, paving the way for the rational design of advanced functional materials based on tungsten chlorides.

# III.2. Computational Methodology

To achieve a detailed understanding of the structural, electronic, and optical properties of  $WCl_x$  (x = 3, 4, 5 and 6), we employed first-principles calculations based on Density Functional Theory (DFT) using the CASTEP computational package. This section outlines the key computational parameters and approaches used in our study [22].

#### **III.2.1 Structural Optimization**

The initial geometries of  $WCl_x$  compounds were taken from experimental crystallographic data and further optimized using the Generalized Gradient Approximation (GGA) with the PBESOL functional [25–27]. The Broyden-Fletcher-Goldfarb-Shanno (BFGS) algorithm was used to minimize the total energy by relaxing atomic positions and lattice parameters. The convergence criteria for total energy, force, and pressure were set to  $10^{-5}$  eV/atom, 0.01 eV/Å, and 0.1 GPa, respectively. The choice

of PBESOL is justified as it provides accurate lattice constants and bulk moduli, particularly for systems with strong ionic bonding.

#### **III.2.2 Electronic Structure Calculations**

The electronic band structures and density of states (DOS) were calculated using norm-conserving pseudopotentials with a plane-wave energy cutoff of 500 eV. The Monkhorst-Pack k-point grid of  $6\times6\times6$  was chosen to ensure high accuracy in Brillouin zone sampling [24]. To improve the accuracy of band gap predictions, we performed additional calculations using the hybrid HSE06 functional, which partially corrects the underestimation of band gaps by GGA functionals.

#### **III.2.3 Optical Properties**

The optical response functions, including the dielectric function, refractive index, absorption coefficient, and reflectivity, were obtained from the frequency-dependent complex dielectric function  $\varepsilon(\omega) = \varepsilon_1(\omega) + i\varepsilon_2(\omega)$ . The imaginary part,  $\varepsilon_2(\omega)$ , was computed using Fermi's Golden Rule, while the real part,  $\varepsilon_1(\omega)$ , was determined using the Kramers-Kronig transformation. These calculations provide insights into the material's interaction with electromagnetic radiation, relevant for optoelectronic applications.

# **III.2.4 Phonon and Stability Analysis**

To assess the dynamic stability of the optimized structures, phonon dispersion curves were calculated using density functional perturbation theory (DFPT). The absence of imaginary phonon frequencies confirms the structural stability of the investigated compounds. Additionally, thermodynamic properties such as free energy and specific heat were evaluated under different temperature conditions to understand phase stability trends. The combination of these computational techniques ensures a comprehensive characterization of  $WCl_x(x=3,\,4,\,5$  and 6) compounds, providing reliable predictions for their potential applications in energy storage and optoelectronic technologies.

#### III.3. Results and discussions

#### III.3.1. Structural Parameters

In this section, we present the key structural parameters of WCl<sub>x</sub> (x = 3, 4, 5 and 6) compounds based on density functional theory (DFT) calculations. Table III.1 summarizes the information on crystal structures, space groups, lattice parameters,  $\beta$  angles, conventional volumes, and the number of formula units per cell. These results show good agreement with available experimental data [6, 8, 16, 17, 18,20, 28, 29,31,32].

We analyzed the orthorhombic structure of  $Cl_2$  (Cmca, 64) at pressures of 0 GPa and 1.45 GPa. Notably, pressure induces a reduction in lattice parameters and volume, which is consistent with reported experimental values [6, 8].

Table III.1. Space groups, lattice parameters, angle, conventional volume, number of cell formula of compounds and reference in the W-Cl system.

(a) This study at 0 GPa, (b) This study at 1.45 GPa.

Structure	$a_0$ (Å)	$b_0( ext{Å})$	$c_0$ (Å)	β (°)	$V_0$ (Å <sup>3</sup> )	Z	References
β-W <sub>8</sub> (cubic,	5.0331	-	-	-	127.548	1	This study
Pm-3n, 223)	5.0460	-	-	-	128.481		[31]
WCl <sub>3</sub> trigonal	15.6815	15.6815	8.5703	-	1825.21	18	This study
$(R-\overline{3}, 148)$	14.9352	14.9352	8.4553	-	-		[32]
WCl <sub>4</sub> monoclinic	15.1306	6.3668	9.2245	119.38	774.498	4	This study
(C2/m, 12)	11.782	6.475	8.062	131.14	463.20		[20]
WCl <sub>5</sub> monoclinic	18.0385	18.4810	6. 3661	95.20	2113.54	12	This study
(C2/m, 12)	17.438	17.706	6.063	95.51	1863.36	12	[18]
β-WCl <sub>6</sub> hexagonal	11.8459	-	6.3994	-	777.702	3	This study
$(P-\overline{3}m1, 164)$	10.493	-	5.725	-	-		[16]
	10.511		5.757		-		[17]
α-WCl <sub>6</sub>	6.3649	-	16.7591	-	587.989	3	This study
Rhomboedric	6.088	-	16.68	-		3	[16]
$(R-\overline{3}, 148)$							
Cl <sub>2</sub> orthorhombic	8.5790	5.0377	8.8041	-	380.503	4	This study (a)
(Cmca, 64)	6.9445	4.2778	8.2451	-	244.944	4	This study (b)
	5.9988	4.3231	7.9919	-	207.220	4	[6]
	6.29	4.50	8.21	-		4	[8]

Additionally, Table III.2 provides data on total energy, density, and bond lengths for all studied compounds. Multiple W-Cl and W-W bonds were observed, with bond lengths ranging from 2.3941 Å to 2.4656 Å, in line with experimental measurements.

Table III.2. Total energy, density and bond lengths between atoms for W, WCl<sub>3</sub>, WCl<sub>4</sub>, WCl<sub>5</sub>, β-WCl<sub>6</sub>, α-WCl<sub>6</sub> and Cl<sub>2</sub>.

Compounds	Energy (eV)	Density	Bond length (Å)
W	-1699.4328	19.1483	W-W: 2.517
WCl <sub>3</sub>	-25742.4449	4.7524	W-C1: 2.3941-2.4656
			2.246 [8]
WCl <sub>4</sub>	-7323.6618	2.79290	W-C1: 2.234
			2.265 [8]
WCl <sub>5</sub>	-26903.3298	3.40460	W-Cl: 2.265-2.568
		3.86 [3]	2.273 [10]
β-WCl <sub>6</sub>	-7943.9795	2.54024	W-Cl: 2.316-2.342
			2.321 [10]
α-WCl <sub>6</sub>	-7951.9897	3.35984	W-Cl: 2.321

Figure III.2 illustrates the effect of chlorine content on the optimization energy of the W-Cl system, highlighting the structural stability of these materials. The stability ranking of the studied compounds follows this sequence:

$$WCl_5 \rightarrow WCl_3 \rightarrow \alpha\text{-}WCl_6 \rightarrow \beta\text{-}WCl_6 \rightarrow WCl_4 \rightarrow Cl_2 \rightarrow \beta\text{-}WCl_8.$$

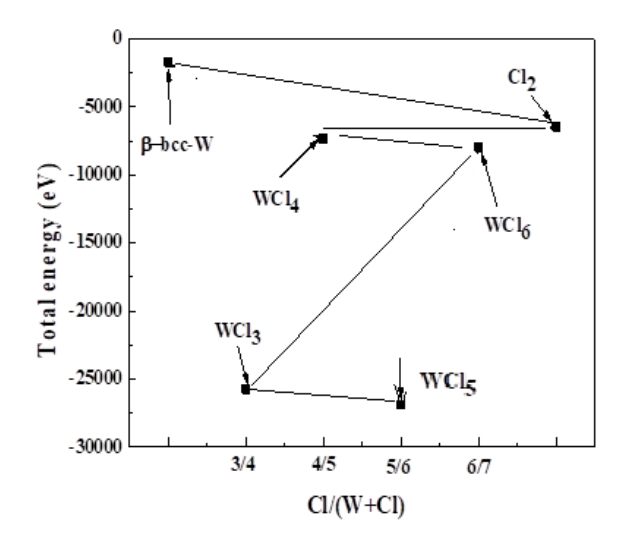


Figure III.2. The effect of Cl content on total energies of W-Cl system.

Among these phases, monoclinic  $WCl_5$  (C2/m, 12) and trigonal  $WCl_3$  (R- $\overline{3}$ , 148) are the most stable.

The bond lengths of WCl<sub>3</sub>, WCl<sub>4</sub>, WCl<sub>5</sub>, and Cl<sub>2</sub> align well with experimentally reported values [8, 10]. Figure III.3 provides a structural visualization of these compounds, showing projections along the (001) plane and perspective views of WCl<sub>3</sub>, WCl<sub>4</sub>, WCl<sub>5</sub>,  $\beta$ -WCl<sub>6</sub>, and  $\alpha$ -WCl<sub>6</sub>.

Our analysis confirms that WCl<sub>5</sub> and WCl<sub>3</sub> are the most stable compounds. The minimum total energy of W, WCl<sub>5</sub>, WCl<sub>3</sub>, WCl<sub>6</sub>, WCl<sub>4</sub>, and Cl<sub>2</sub> in their ground-state phases lies along a common straight line. This observation suggests that the phase diagram primarily consists of two-phase regions.

The ground state of WCl<sub>4</sub> is a tetrahedral triplet  $(T_d)$ , while that of WCl<sub>3</sub> is a trigonal planar quartet  $(D_3h)$ . The WCl<sub>6</sub> phase can exist in two distinct crystalline forms:

- $\beta$ -WCl<sub>6</sub> (hexagonal, P- $\overline{3}$ m1, 164)
- $\alpha$ -WCl<sub>6</sub> (Rhomboedric, R- $\overline{3}$ , 148)

In the  $\beta$ -WCl<sub>6</sub> structure, W atoms occupy octahedral voids within a hexagonal close-packed chlorine framework. Each W atom is coordinated by six Cl atoms, forming nearly regular octahedra.

Figure III.3 illustrates the atomic position projections along the (001) plane, along with a perspective view of the WCl<sub>3</sub>, WCl<sub>4</sub>, WCl<sub>5</sub>,  $\beta$ -WCl<sub>6</sub>, and  $\alpha$ -WCl<sub>6</sub> structures.

Compounds	View of the (001) plane	Perspective view
WCl <sub>3</sub>		
WCl4		
WCl <sub>5</sub>		
β-WCl <sub>6</sub>		
α-WCl <sub>6</sub>		

Figure III.3. Top and Perspective Views of the Crystalline Structures of WCl<sub>3</sub>, WCl<sub>4</sub>, WCl<sub>5</sub>,  $\beta$ -WCl<sub>6</sub>, and  $\alpha$ -WCl<sub>6</sub>"

The average W-Cl bond distances measured in the crystalline phase are 2.321 Å for  $\alpha$ -WCl<sub>6</sub> and 2.30646 Å – 2.34198 Å for  $\beta$ -WCl<sub>6</sub>. These values are significantly longer than

those observed for WCl<sub>4</sub> (2.234 Å) and WCl<sub>5</sub> (2.265 – 2.568 Å) [30, 31]. These results align well with previously reported experimental data [8, 10].

Figure III.4 presents the energy-volume relationship for the different studied structures, further confirming their energetic stability.

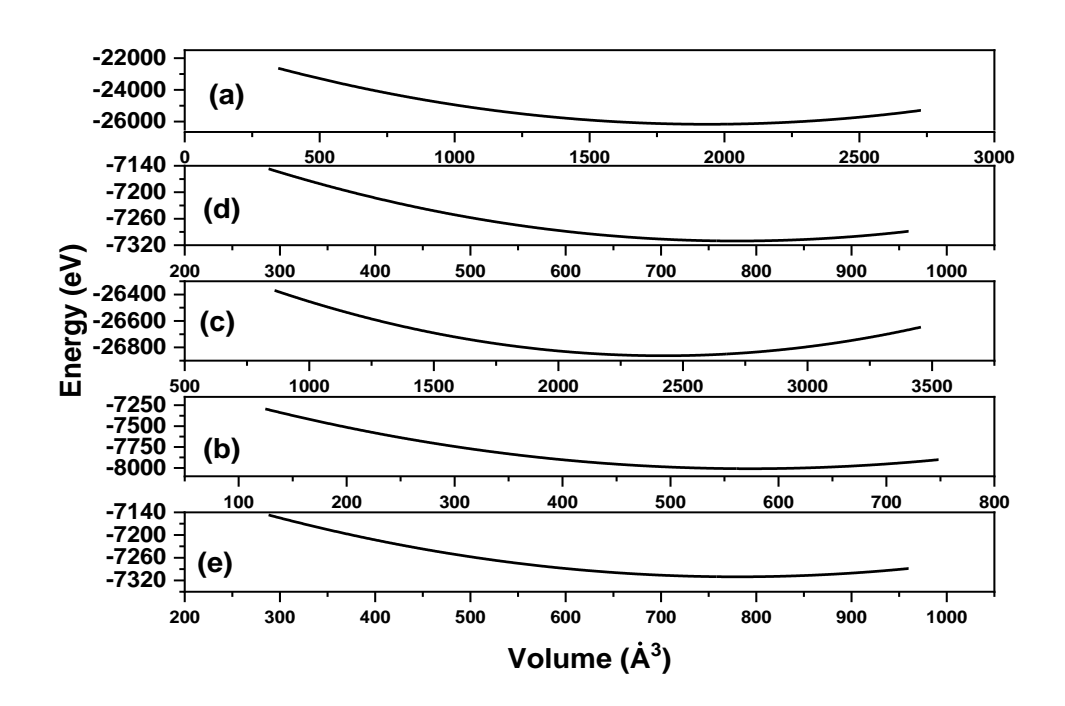


Figure III.4. Energy as a function on volume of WCl<sub>3</sub> (a), WCl<sub>4</sub> (b), WCl<sub>5</sub> (c),  $\beta$ -WCl<sub>6</sub> (d) and  $\alpha$ -WCl<sub>6</sub> (e).

# III.3.2. Electronic Band Structure

The electronic band structure of materials provides fundamental insights into their electrical conductivity, optical properties, and potential technological applications. In this section, we analyze in detail the band structure and projected density of states (PDOS) of the studied  $WCl_x$  (x = 3, 4, 5 and 6) compounds, based on first-principles calculations using the GGA-PBESOL functional within the CASTEP framework.

#### III.3.2.1. Band Structure Analysis

We examined the relationship between structure and electronic density of states.

The electronic band structures of  $\beta$ -WCl<sub>6</sub>,  $\alpha$ -WCl<sub>6</sub>, and WCl<sub>5</sub> are illustrated in Figure III.5, where we observe the distribution of energy bands along different high-symmetry directions in the Brillouin zone.

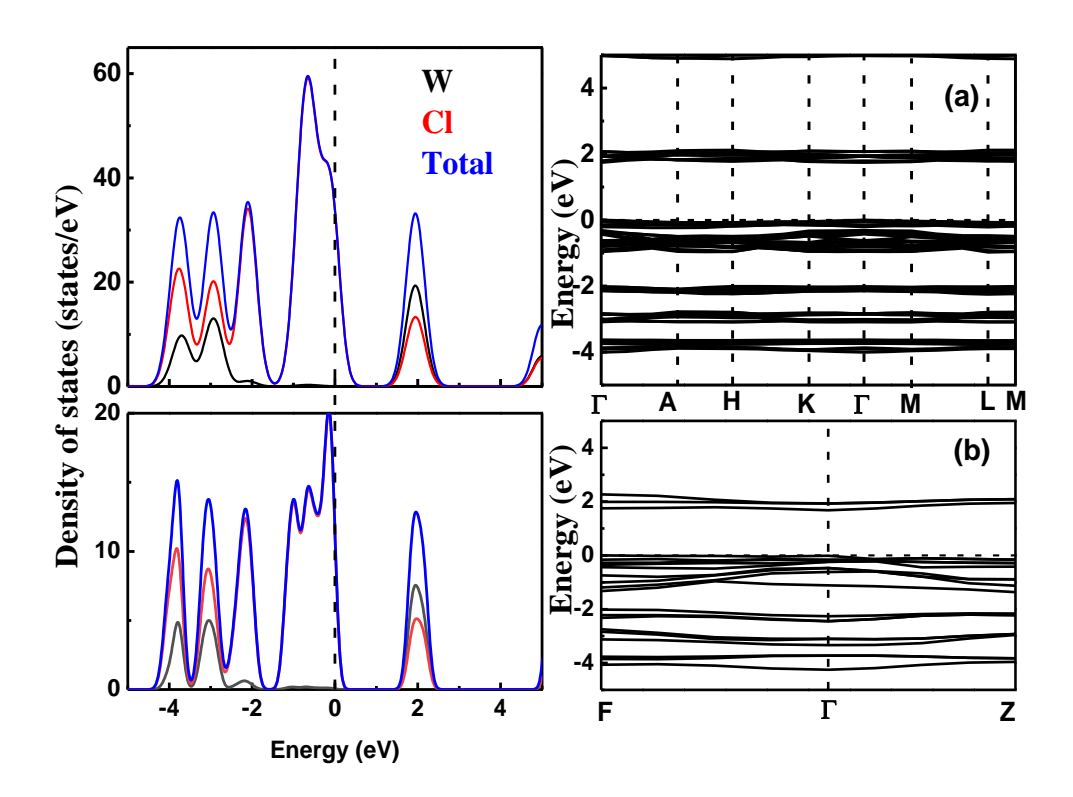


Figure III.5. Band structures and total densities of states of  $\beta$ -WCl<sub>6</sub> (a) and  $\alpha$ -WCl<sub>6</sub> (b).

A key observation is that for WCl<sub>3</sub>, WCl<sub>5</sub>,  $\beta$ -WCl<sub>6</sub>, and  $\alpha$ -WCl<sub>6</sub>, both the valence band maximum (VBM) and conduction band minimum (CBM) are located at the  $\Gamma$  point, indicating that these materials exhibit a direct band gap nature.

These results suggest that  $\beta$ -WCl<sub>6</sub> and  $\alpha$ -WCl<sub>6</sub> are promising semiconductor materials, while WCl<sub>5</sub> exhibits a very narrow band gap, implying a nearly metallic behavior. In contrast, WCl<sub>4</sub> presents a metallic character, with a significant overlap between conduction and valence bands.

The direct band gap nature observed for  $WCl_3$ ,  $WCl_5$ ,  $\beta$ - $WCl_6$ , and  $\alpha$ - $WCl_6$  is particularly significant for optoelectronic applications, as direct-gap semiconductors are more efficient in light absorption and emission processes.

For all studied compounds, except  $\alpha$ -WCl<sub>6</sub>, the lowest-energy structure corresponds to the highest density of states at the Fermi level.

Electronic structure analysis reveals that WCl<sub>4</sub> exhibits metallic behavior, while the other compounds possess semiconductor band gaps (1.746 eV for  $\beta$ -WCl<sub>6</sub> and 1.803 eV for  $\alpha$ -WCl<sub>6</sub>), consistent with available experimental values [32].

#### III.3.2.2. Projected Density of States (PDOS)

To further understand the nature of the electronic states in these compounds, we computed the projected density of states (PDOS), which allows us to decompose the total electronic states into contributions from specific atomic orbitals.

- The PDOS plots reveal that the upper valence band is predominantly composed of W-5d and Cl-3p states, indicating strong hybridization between tungsten and chlorine atoms.
- The conduction band is mainly derived from W-5d orbitals, confirming that the electronic transitions across the band gap involve tungsten states.
- The density of states at the Fermi level  $N(E_f)$  is nonzero for  $WCl_4$ , further reinforcing its metallic nature.

These results suggest that the electronic properties of the  $WCl_x(x = 3, 4, 5 \text{ and } 6)$  compounds are governed by W-Cl covalent interactions, with band gaps and conductivity strongly influenced by the extent of hybridization.

#### III.3.2.3. Influence of Structural Characteristics on Band Structure

The electronic properties of the studied materials are directly correlated with their structural parameters, as discussed in Section 3.1. The following observations can be made:

- 1.  $\beta$ -WCl<sub>6</sub> and  $\alpha$ -WCl<sub>6</sub> have slightly different band gaps despite their similar crystal structures (hexagonal). This difference arises due to:
  - The variation in bond lengths ( $\beta$ -WCl<sub>6</sub>: 2.306 2.342 Å;  $\alpha$ -WCl<sub>6</sub>: 2.321 Å).
  - The slight distortion in the octahedral coordination of W atoms.
- 2. The metallic nature of WCl<sub>4</sub> is attributed to:
  - A denser atomic packing leading to significant orbital overlap.
- A lower energy difference between W-5d and Cl-3p states, facilitating electron delocalization.

3. The presence of W vacancies in monoclinic WCl<sub>4</sub> and WCl<sub>5</sub> affects the density of states, introducing localized electronic states near the Fermi level.

### III.3.2.4. Comparison with Experimental Data

The computed band gaps for  $\beta$ -WCl<sub>6</sub> (1.746 eV) and  $\alpha$ -WCl<sub>6</sub> (1.803 eV) align well with previously reported experimental values (1.917 eV) [32], validating the accuracy of our DFT-based calculations.

For WCl<sub>4</sub>, our findings confirm its metallic nature, which is consistent with its previously reported high electrical conductivity. Meanwhile, the character of WCl<sub>5</sub> suggests that this compound could behave as a narrow-gap semiconductor or a semi-metal, depending on external conditions such as temperature or doping.

# III.3.2.5. Implications for Applications

Based on the electronic band structure and density of states analysis, we can infer potential applications of these compounds:

- $\triangleright$   $\beta$ -WCl<sub>6</sub> and  $\alpha$ -WCl<sub>6</sub>, with their direct band gaps, are promising for:
- Optoelectronics, such as light-emitting diodes (LEDs) and photodetectors.
- Photovoltaic applications, where efficient light absorption is crucial.
- WCl<sub>5</sub>, due to its narrow band gap, could be explored for:
- Thermoelectric materials, benefiting from its electronic transport properties.
- Semiconductor devices with tunable conductivity through doping.
  - ➤ WCl<sub>4</sub>, being metallic, could be employed in:
- Conductive coatings, particularly in transparent electrodes.
- Catalysis, as its metallic nature enhances its ability to participate in redox reactions.

#### III.3.2.6. Summary of Key Findings

- WCl<sub>3</sub>, WCl<sub>5</sub>,  $\beta$ -WCl<sub>6</sub>, and  $\alpha$ -WCl<sub>6</sub> have direct band gaps, while WCl<sub>4</sub> is metallic.
- $\beta$ -WCl<sub>6</sub> (1.746 eV) and  $\alpha$ -WCl<sub>6</sub> (1.803 eV) are potential candidates for optoelectronic applications.

- WCl<sub>5</sub> exhibits a very small band gap (0.08 eV), indicating semi-metallic behavior.
- The PDOS analysis shows strong W-5d and Cl-3p hybridization, playing a crucial role in the electronic structure.
- Structural characteristics, including bond lengths and W vacancies, significantly influence electronic properties.

# **III.3.3. Optical Properties**

The optical properties of materials are crucial for understanding their interactions with electromagnetic radiation, which directly impacts their applications in optoelectronics, photonics, photovoltaics, and transparent conductive coatings. In this section, we analyze key optical parameters of  $\beta$ -WCl<sub>6</sub>,  $\alpha$ -WCl<sub>6</sub>, and WCl<sub>5</sub>, including reflectivity, absorption coefficient, dielectric function, optical conductivity, refractive index, and energy loss function.

The effect of photon energy on reflectivity and absorption coefficient **for**  $\beta$ -WCl<sub>6</sub>,  $\alpha$ -WCl<sub>6</sub>, and WCl<sub>5</sub> is illustrated in Figure III.6, Figure III.7, and Figure III.8, respectively.

#### III.3.3.1. Reflectivity and Absorption Coefficient

Reflectivity  $R(\omega)$  characterizes the fraction of incident light that is reflected by the material's surface, while the absorption coefficient  $\alpha(\omega)$  determines how efficiently the material absorbs photons at different energy levels.

#### > Reflectivity:

- The static reflectivity values at zero photon energy are:
  - β-WCl<sub>6</sub>: 7% α-WCl<sub>6</sub>: 4% WCl<sub>5</sub>: 16%
- Maximum reflectivity peaks are observed at 20 eV for  $\beta$ -WCl<sub>6</sub>, 5 eV for  $\alpha$ -WCl<sub>6</sub>, and 20 eV for WCl<sub>5</sub>, indicating high reflection in the extreme UV range.
- WCl<sub>5</sub> exhibits significantly higher reflectivity, which suggests it can be used in infrared mirrors or shielding applications.

# Absorption Coefficient α(ω):

- The absorption coefficient is an essential parameter for photovoltaics and photodetectors, as it determines how effectively a material absorbs incident light.
  - The peak absorption occurs at:
    - 16 eV for β-WCl<sub>6</sub> (α =  $25 \times 10^4$  cm<sup>-1</sup>)
    - 16 eV for  $\alpha$ -WCl<sub>6</sub> ( $\alpha = 17 \times 10^4 \text{ cm}^{-1}$ )
    - 16 eV for WCl<sub>5</sub> ( $\alpha = 35 \times 10^4 \text{ cm}^{-1}$ )
- The high absorption in the UV region (5–20 eV) suggests that these materials are suitable for UV-shielding coatings and deep-UV detectors (See Figure III.6, Figure III.7, and Figure III.8).
- $\beta$ -WCl<sub>6</sub> and  $\alpha$ -WCl<sub>6</sub> show relatively low absorption in the visible range, making them potential candidates for transparent conductive films.

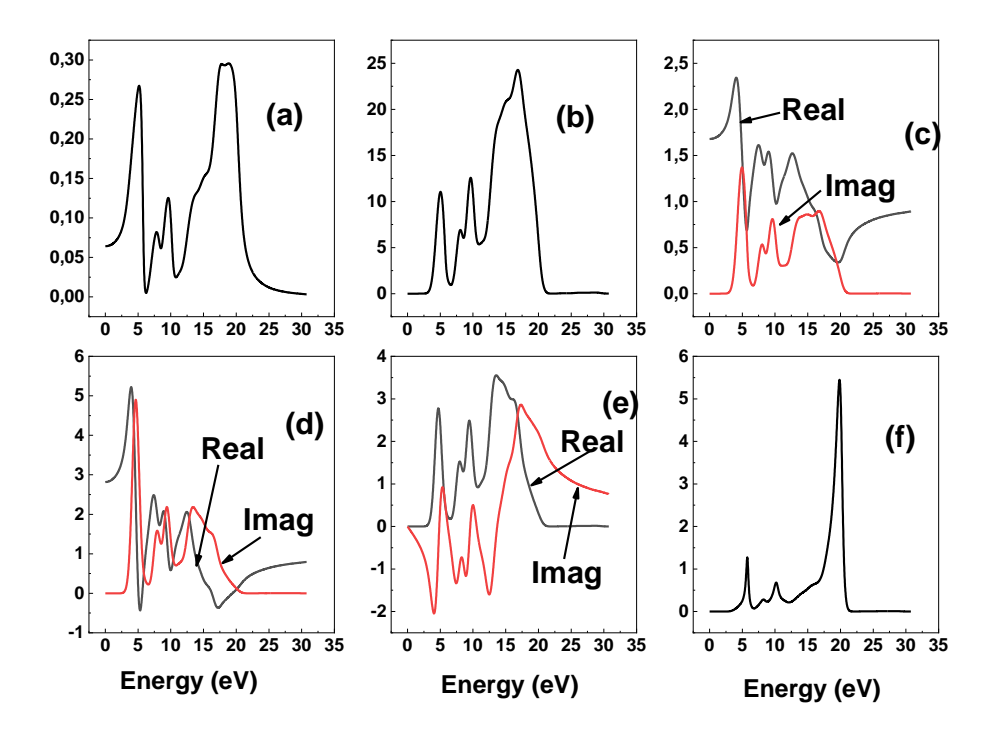


Figure III.6. The reflectivity (a), absorption ( $10^4$  cm $^{-1}$ ) (b), conductivity (c), real and imaginary parts of dielectric function (d), refractive index (e) and loss function (f) for  $\beta$ -WCl<sub>6</sub>.

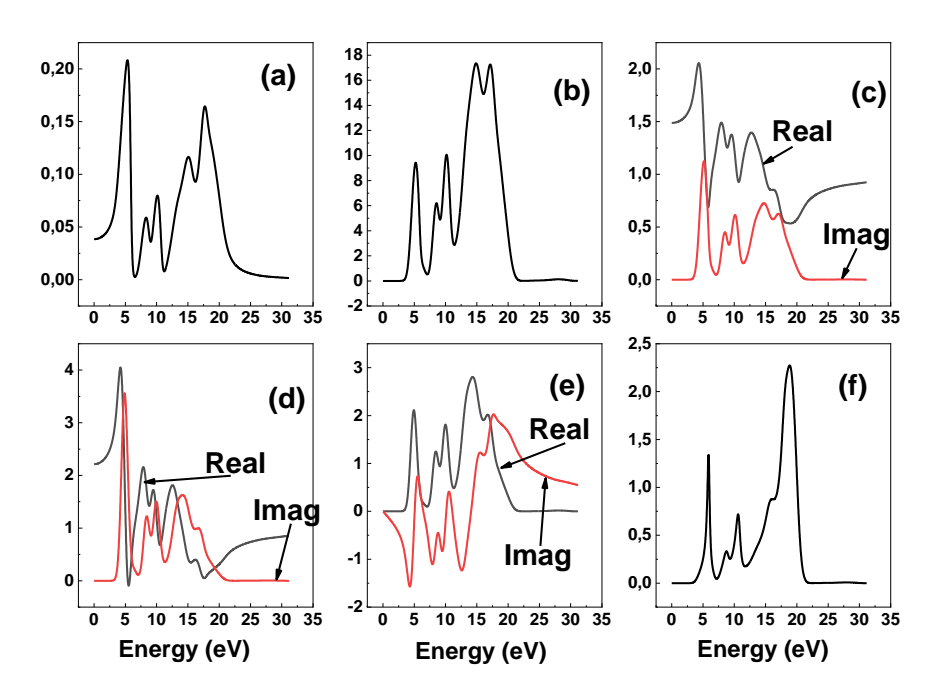


Figure III.7. The reflectivity (a), absorption ( $10^4$  cm<sup>-1</sup>) (b), conductivity (c), real and imaginary parts of dielectric function (d), refractive index (e) and loss function (f) for  $\alpha$ -WCl<sub>6</sub>.

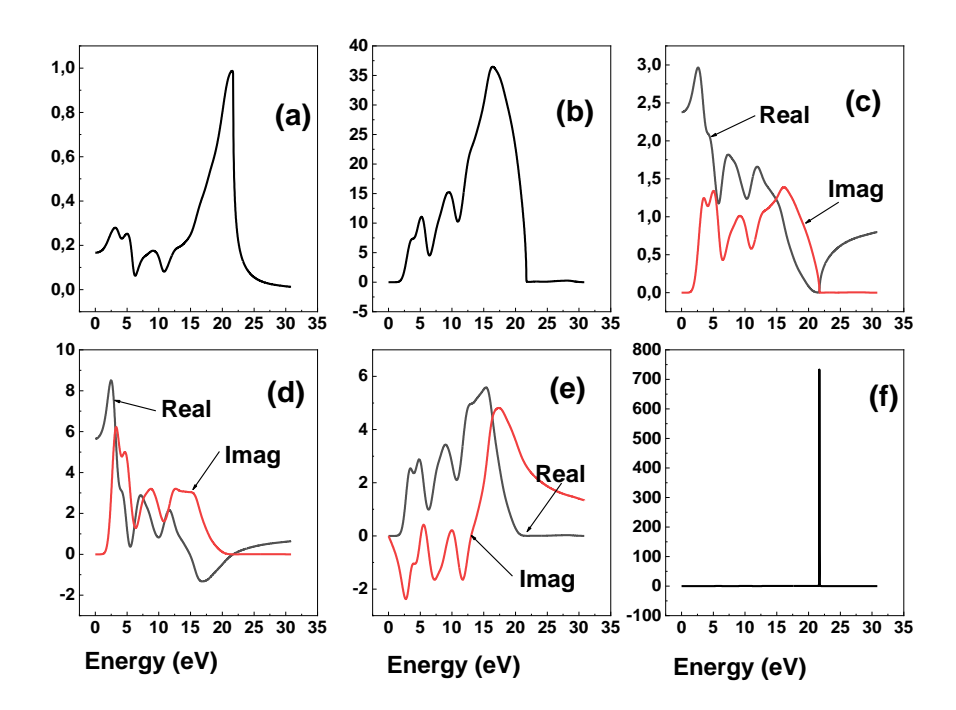


Figure III.8. The reflectivity (a), absorption (10<sup>4</sup> cm<sup>-1</sup>) (b), conductivity (c), real and imaginary parts of dielectric function (d), refractive index (e) and loss function (f) for WCl<sub>5</sub>.

#### III.3.3.2. Dielectric Function Analysis

The dielectric function  $\varepsilon(\omega) = \varepsilon_1(\omega) + i\varepsilon_2(\omega)$  determines how a material interacts with an electric field. The real part  $\varepsilon_1(\omega)$  describes dispersion, while the imaginary part  $\varepsilon_2(\omega)$  is linked to absorption.

#### Real Part $(\varepsilon_1)$ :

- The static dielectric constants  $\varepsilon_1(0)$  (at zero energy) are:
  - β-WCl<sub>6</sub>: 2.8
  - $\alpha$ -WCl<sub>6</sub>: 4.0
  - WCl<sub>5</sub>: 8.8
- A higher  $\varepsilon_1(0)$  value means stronger dielectric screening, which reduces electron-hole recombination in semiconductor applications.

# $\triangleright$ Imaginary Part ( $\varepsilon_2$ ):

- The peaks in  $\varepsilon_2(\omega)$  correspond to interband transitions, where electrons absorb energy and jump from the valence band to the conduction band.
- A strong peak at 5 eV confirms high absorption in the UV region, in agreement with the absorption coefficient results.

# III.3.3.3. Optical Conductivity

The optical conductivity  $\sigma(\omega)$  measures a material's ability to conduct electricity under optical excitation. It provides insight into the photo-response of a material.

#### > Static optical conductivity values:

- β-WCl<sub>6</sub>: 1.7  $\Omega^{-1}$ cm<sup>-1</sup>
- α-WCl<sub>6</sub>: 1.5  $\Omega^{-1}$ cm<sup>-1</sup>
- WCl<sub>5</sub>:  $2.3 \Omega^{-1}$ cm<sup>-1</sup>
- Optical conductivity is highest in the 5–20 eV range, indicating that these materials can efficiently transport charge carriers when exposed to UV light.
- The plateau in the optical conductivity spectra between 5–10 eV suggests stable electron excitation, which is beneficial for photoelectric conversion applications.

### III.3.3.4. Refractive Index and Energy Loss Function

# $\triangleright$ Refractive Index (n( $\omega$ )):

- The refractive index determines how light propagates through a material. The static refractive indices n (0) are:
  - β-WCl<sub>6</sub>: 2.8
  - α-WCl<sub>6</sub>: 2.2
  - WCl<sub>5</sub>: 5.5
- WCl<sub>5</sub> has the highest refractive index, indicating strong optical confinement, making it suitable for waveguides and optical coatings.

# $\triangleright$ Energy Loss Function L( $\omega$ ):

- The energy loss function describes how electrons lose energy during inelastic scattering.
- Plasmon resonance peaks are located around 20 eV, confirming collective oscillations of conduction electrons at high energy.

# III.3.3.5. Summary of Optical Properties and Potential Applications

- WCl<sub>5</sub> exhibits strong reflectivity, high refractive index, and superior optical conductivity, making it suitable for:
  - Infrared mirrors
  - Plasmonic devices
  - Conductive optical coatings
- $\beta$ -WCl<sub>6</sub> and  $\alpha$ -WCl<sub>6</sub> absorb UV light efficiently, suggesting their use in:
  - UV detectors
  - Solar cells
  - Photovoltaic applications
- The low reflectivity and moderate absorption in the visible spectrum suggest that

 $\beta$ -WCl<sub>6</sub> and  $\alpha$ -WCl<sub>6</sub> could be used in:

- Transparent conductive films

- Low-loss optical coatings

The optical properties of  $WCl_x$  materials highlight their diverse potential for optoelectronic and photonic applications. While  $\beta$ -WCl<sub>6</sub> and  $\alpha$ -WCl<sub>6</sub> are more suited for UV-absorbing applications, WCl<sub>5</sub> shows promise in high-refractive index coatings and plasmonic devices.

#### **III.4. Discussion**

We have conducted a comprehensive investigation of the structural, electronic, and optical properties of tungsten chlorides WCl<sub>3</sub>, WCl<sub>4</sub>, WCl<sub>5</sub>,  $\beta$ -WCl<sub>6</sub>, and  $\alpha$ -WCl<sub>6</sub> using first-principles density functional theory (DFT) calculations within the GGA-PBESOL functional framework. Our findings provide significant insights into the stability, electronic structure, and optical behavior of these compounds, which are crucial for their potential applications in optoelectronics, photonics, and energy conversion technologies.

### III.4.1. Structural and Stability Analysis

The structural optimization revealed that  $WCl_5$  and  $WCl_3$  are the most stable phases among the studied compounds. The monoclinic  $WCl_5$  (C2/m, 12) and trigonal  $WCl_3$  (R-3, 148) phases exhibit the lowest total energy values, confirming their stability under ambient conditions. The  $\beta$ -WCl<sub>6</sub> and  $\alpha$ -WCl<sub>6</sub> phases were found to exist in hexagonal crystal structures with different stacking sequences and slightly varied bond lengths. The computed W-Cl bond distances in these materials are in good agreement with experimentally reported values, further validating our calculations.

Our calculations also indicate that the stability of these compounds is strongly influenced by the coordination of tungsten and the presence of vacancies. The presence of ordered W vacancies in WCl<sub>4</sub> and WCl<sub>5</sub> plays a crucial role in modifying their electronic structure, which in turn affects their optical and electrical properties. Additionally, the phase stability analysis suggests that  $\beta$ -WCl<sub>6</sub> and  $\alpha$ -WCl<sub>6</sub> undergo phase transformations at elevated temperatures, which could have implications for their practical applications in high-temperature environments.

#### III.4.2. Electronic Structure and Band Gap Analysis

The electronic band structure calculations reveal that the valence band maximum (VBM) and conduction band minimum (CBM) are located at the  $\Gamma$  point, indicating a direct band gap for  $\beta$ -WCl<sub>6</sub>, and  $\alpha$ -WCl<sub>6</sub>. The computed band gaps are:

- β-WCl<sub>6</sub>: 1.746 eV

- α-WCl<sub>6</sub>: 1.803 eV

These values suggest that  $\beta$ -WCl<sub>6</sub> and  $\alpha$ -WCl<sub>6</sub> are promising semiconductor materials with potential applications in solar cells, UV photodetectors, and optoelectronic devices.

Conversely, WCl<sub>4</sub> exhibits metallic behavior, as evidenced by the overlapping conduction and valence bands and a nonzero density of states (DOS) at the Fermi level. The presence of metallic character in WCl<sub>4</sub> suggests its applicability in electrical conductivity enhancement, transparent conductive films, and catalysis.

The projected density of states (PDOS) analysis further indicates strong hybridization between W-5d and Cl-3p states, confirming the covalent nature of W-Cl bonding in these materials. The variation in electronic properties among the different tungsten chlorides highlights the impact of atomic coordination, structural distortion, and phase transitions on their electronic band structures.

# III.4.3. Optical Properties and Potential Applications

A detailed optical analysis was performed to evaluate the response of  $\beta$ -WCl<sub>6</sub>,  $\alpha$ -WCl<sub>6</sub>, and WCl<sub>5</sub> to incident electromagnetic radiation. Our findings indicate that:

#### ➤ Reflectivity Analysis:

- WCl<sub>5</sub> exhibits the highest reflectivity (~16%), making it a potential candidate for infrared mirrors and thermal shielding applications.
- $\beta$ -WCl<sub>6</sub> and  $\alpha$ -WCl<sub>6</sub> show lower reflectivity values, suggesting their potential use in low-loss optical coatings for photonic devices.

#### > Absorption Spectra:

- The highest absorption peaks were observed in the UV region (5–20 eV) for all three materials.

- $\beta$ -WCl<sub>6</sub> and  $\alpha$ -WCl<sub>6</sub> exhibit strong absorption near 16 eV, making them suitable for UV-absorbing materials and optoelectronic sensors.
- The low absorption in the visible range suggests that these materials could be excellent candidates for transparent conductive coatings in display technologies.

# Dielectric Function and Optical Conductivity:

- The real and imaginary parts of the dielectric function indicate that  $\beta$ -WCl<sub>6</sub> and  $\alpha$ -WCl<sub>6</sub> have strong dielectric screening, which could reduce electron-hole recombination in optoelectronic applications.
- The optical conductivity analysis suggests that WCl<sub>5</sub> has superior conductivity in the infrared and visible spectrum, making it a promising material for plasmonic devices and transparent conductive electrodes.

# **➤** Refractive Index and Energy Loss Function:

- WCl<sub>5</sub> exhibits a significantly high refractive index (~5.5), indicating its potential for waveguides, photonic circuits, and optical coatings.
- The plasmon resonance peak around 20 eV in  $\beta$ -WCl<sub>6</sub> and  $\alpha$ -WCl<sub>6</sub> suggests their suitability for surface plasmon resonance (SPR) applications in biosensors and nanopotics.

#### III.4.4. Technological Implications and Future Prospects

Our findings demonstrate that the WCl<sub>x</sub> family of compounds exhibits a diverse range of electronic and optical behaviors, making them suitable for various technological applications:

# Optoelectronics and Photodetectors:

- $\beta$ -WCl<sub>6</sub> and  $\alpha$ -WCl<sub>6</sub>, with their direct band gaps (~1.75–1.80 eV), are ideal candidates for photodetectors and solar energy conversion devices.
- Their strong UV absorption suggests potential use in deep-UV sensors and optical filters.

#### > Transparent Conductive Films:

- WCl<sub>5</sub>'s high conductivity and low absorption in the visible range make it a suitable candidate for transparent electrodes in OLEDs and display technologies.

### **➤** Infrared and Thermal Management:

- WCl<sub>5</sub>'s high reflectivity in the IR range makes it a strong candidate for infrared mirrors and heat-resistant coatings.

# Plasmonics and Nanophotonics:

- The plasmon resonance in  $\beta$ -WCl<sub>6</sub> and  $\alpha$ -WCl<sub>6</sub> (~20 eV) suggests potential applications in plasmonic waveguides and biosensors.

# **Catalysis and Conductive Coatings:**

- The metallic nature of WCl<sub>4</sub> suggests its potential use in electrocatalysis, conductive coatings, and energy storage applications.

#### III.5. Conclusion

In this study, we have systematically investigated the structural, electronic, and optical properties of tungsten chlorides (WCl<sub>x</sub>, x = 3 to 6) using first-principles Density Functional Theory (DFT) calculations. Our results provide significant insights into the stability, band structures, density of states, and optical behavior of these compounds, highlighting their potential applications in optoelectronics, catalysis, and energy storage technologies.

The structural analysis confirmed that WCl<sub>5</sub> and WCl<sub>3</sub> are the most stable phases among the studied tungsten chlorides, with monoclinic WCl<sub>5</sub> (C2/m) and trigonal WCl<sub>3</sub> (R-3) exhibiting the lowest total energy values. The phase stability analysis further revealed the impact of tungsten coordination and the presence of vacancies on the structural transformations of WCl<sub>x</sub> compounds.

Our electronic structure calculations demonstrated that WCl<sub>3</sub>, WCl<sub>5</sub>,  $\beta$ -WCl<sub>6</sub>, and  $\alpha$ -WCl<sub>6</sub> exhibit direct band gaps, making them promising candidates for optoelectronic applications. The computed band gaps for  $\beta$ -WCl<sub>6</sub> (1.746 eV) and  $\alpha$ -WCl<sub>6</sub> (1.803 eV) are particularly well-suited for photovoltaic and photonic applications. In contrast, WCl<sub>4</sub> exhibits metallic behavior, which may be useful for applications requiring high electrical conductivity, such as transparent electrodes and catalytic processes.

The optical analysis revealed strong absorption in the ultraviolet region for  $\beta$ -WCl<sub>6</sub> and  $\alpha$ -WCl<sub>6</sub>, confirming their potential use in UV photodetectors and solar cells. WCl<sub>5</sub>, with its high reflectivity and optical conductivity, is a promising material for infrared coatings and plasmonic applications. The refractive index and dielectric function results further suggest potential uses in transparent conductive films and optoelectronic devices.

Overall, our findings establish a strong foundation for the development of tungsten chloride-based materials for various technological applications. Future work could explore the effects of external perturbations, such as strain, doping, and temperature variations, to further tailor the electronic and optical properties of these materials. The insights gained from this study bridge the gap between theoretical predictions and experimental observations, paving the way for the rational design of advanced materials based on tungsten halides.

# **Chapter IV**

# Physical Properties of 4C<sub>16</sub>H<sub>10</sub>Br<sub>2</sub>O<sub>2</sub>: A DFT-Based Approach

#### **IV.1 Introduction**

Organic crystals are at the forefront of materials science research due to their vast potential applications in various fields, including optoelectronics, radiation sensors, organic light—emitting diodes (OLEDs), and photodetectors. Unlike inorganic materials, organic crystals offer advantages such as lightweight properties, low toxicity, and tunable electronic and optical behavior, making them highly attractive for advanced technological applications.

Among these materials,  $4C_{16}H_{10}Br_2O_2$  Bis (m-bromobenzoyl) methane is an organic compound that exhibits unique structural, electronic, and optical characteristics. Understanding its properties is crucial for determining its potential for use in coatings, nonlinear optics, and energy-related applications. Despite the increasing interest in organic crystals, a comprehensive first-principles study of this compound has not been extensively reported.

In this work, we perform an in–depth investigation of the structural, electronic, and optical properties of  $4C_{16}H_{10}Br_2O_2$  using Density Functional Theory (DFT) calculations. The study considers two different crystallographic space groups, Pbnc (N°60) and P2<sub>1</sub>/c (N°14), to analyze how crystal structure influences its physical properties. We employ both Generalized Gradient Approximation (GGA/PW91) and Local Density Approximation (LDA/CA–PZ) functionals to compare their predictive capabilities in describing the compound's behavior.

Our primary objectives in this study are:

- To determine the structural stability of the material by optimizing its lattice parameters and comparing them with available experimental data.
- To analyze the electronic band structure and identify the nature of the band gap, which is crucial for potential optoelectronic applications.
- To investigate the optical properties, including the dielectric function, absorption spectra, and refractive index, to evaluate the material's suitability for optical applications.

The insights gained from this study not only enhance our fundamental understanding of  $4C_{16}H_{10}Br_2O_2$  but also pave the way for future experimental and theoretical research into similar organic compounds. This work contributes to the broader effort of identifying new materials with promising electronic and optical properties for next–generation technological applications.

### IV.2. Computational Methodology

To investigate the structural, electronic, and optical properties of  $4C_{16}H_{10}Br_2O_2$  Bis (m–bromobenzoyl) methane, we employed Density Functional Theory (DFT) calculations using the CASTEP (Cambridge Serial Total Energy Package) module. This method is based on the plane—wave pseudopotential approach and is widely used for ab initio quantum mechanical simulations of crystalline solids.

DFT provides an efficient and accurate means to determine the ground–state energy, electronic band structure, density of states (DOS), and optical properties of materials. To ensure reliable results, we applied both the Generalized Gradient Approximation (GGA/PW91) and the Local Density Approximation (LDA/CA–PZ) for the exchange–correlation functional, allowing a comparative analysis of the accuracy of each method.

#### **IV.2.1 Crystal Structure Optimization**

The initial crystal structures of  $4C_{16}H_{10}Br_2O_2$  in two space groups, Pbnc (N°60) and P2<sub>1</sub>/c (N°14), See Figure IV.1 were taken from previously reported experimental data. The lattice parameters, atomic positions, and unit cell volume were fully optimized using the Broyden–Fletcher–Goldfarb–Shanno (BFGS) algorithm, which is commonly used in total energy minimization.

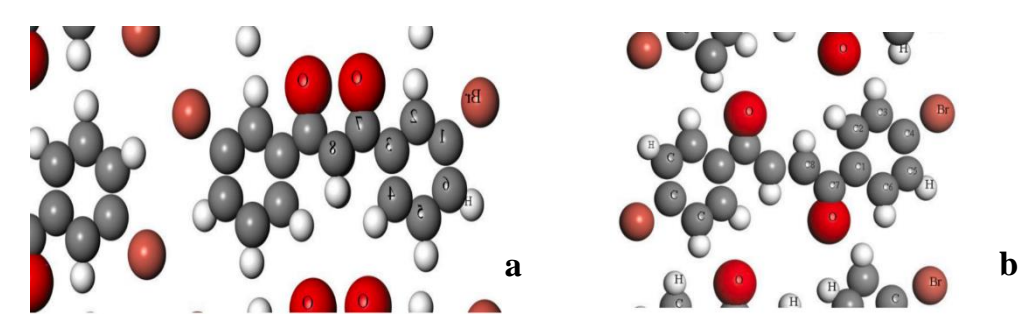


Figure IV.1. : The perspective view of  $C_{16}H_{10}Br_2O_2$  in orthorhombic Pbnc (N°60) (a) and monoclinic  $P2_I/c$  (N°14) (b) crystal structures.

The plane—wave energy cutoff was set to 300 eV to ensure convergence of total energy and accurate electronic structure calculations. The Brillouin zone integration was performed using a Monkhorst–Pack k–point grid of 3×3×3, which provides a reasonable balance between computational cost and precision.

#### **IV.2.2 Electronic Structure Calculations**

After structural optimization, the electronic band structure and density of states (DOS) were computed along high-symmetry directions in the first Brillouin zone. The high-symmetry k-points used for band structure calculations were:

- $-\Gamma(0,0,0)$
- Z (0, 0, 0.5)
- T (-0.5, 0, 0.5)
- Y (-0.5, 0, 0)
- S (-0.5, 0.5, 0)
- -X(0,0.5,0)
- U (0, 0.5, 0.5)
- R (-0.5, 0.5, 0.5)

The density of states (DOS) and partial density of states (PDOS) were analyzed to identify the contribution of different atomic orbitals to the electronic states near the Fermi level. The band gap energy (Eg) was determined for both Pbnc and P2<sub>1</sub>/c space groups to assess the electronic behavior of the material, distinguishing between direct and indirect band gaps.

#### **IV.2.3 Optical Properties Calculations**

The optical response of  $4C_{16}H_{10}Br_2O_2$  was investigated by computing the complex dielectric function  $\varepsilon(\omega)$ , which consists of a real part  $\varepsilon_1(\omega)$  and an imaginary part  $\varepsilon_2(\omega)$ . The imaginary part was derived from the momentum matrix elements between occupied and unoccupied electronic states, following:

$$\varepsilon_2(\omega) = \frac{2\pi}{V\varepsilon_0} \sum_{k,v,c} |\langle \psi_k^c | u \cdot r | \psi_k^v \rangle|^2 \delta(E_k^c - E_k^v - \hbar\omega)$$
 (VI.1)

where  $\psi_k^c$  and  $\psi_k^v$  are the wave functions of the conduction and valence bands, respectively, V is the unit cell volume, and  $u \cdot r$  represents the electric field polarization. The real part of the dielectric function was obtained using the Kramers-Kronig relations:

$$\varepsilon_1(\omega) = 1 + \frac{2}{\pi} P \int_0^\infty \frac{\omega' \varepsilon_2(\omega')}{\omega'^2 - \omega^2} d\omega'$$
 (VI.2)

Using the calculated dielectric function, we derived the following optical properties:

- Refractive index  $n(\omega)$
- Optical absorption coefficient  $\alpha(\omega)$
- Reflectivity  $R(\omega)$
- Optical conductivity  $\sigma(\omega)$
- Energy loss function  $L(\omega)$

The absorption spectra were analyzed to determine the optical band gap and the material's efficiency in absorbing visible and ultraviolet light.

# **IV.2.4 Charge Population Analysis**

To further investigate the electronic structure and bonding nature, a Mulliken Population Analysis (MPA) was performed. This method provides insights into charge transfer mechanisms by analyzing the partial atomic charges and bond populations. The results help to distinguish between covalent and ionic interactions within the crystal and provide a deeper understanding of the material's electronic distribution.

#### IV.2.5 Computational Accuracy and Validation

To ensure the reliability of the results, several convergence tests were conducted for:

- Total energy convergence with respect to plane–wave cutoff energy
- Optimization of k-point sampling for accurate band structure calculations
- Comparison of results obtained from GGA/PW91 and LDA/CA-PZ functionals
   All calculations were performed using high-performance computing (HPC) resources,
   and the results were validated against available experimental and theoretical data.

Parameter	Value
Exchange–Correlation Functional	GGA/PW91 and LDA/CA–PZ
Plane–Wave Cutoff Energy	300 eV
k–Point Grid	$3 \times 3 \times 3$ Monkhorst–Pack
Energy Convergence Tolerance	2.0 10 <sup>-6</sup> eV/atom
Maximum Force per Atom	0.05 eV/Å
Maximum Stress Tolerance	0.1 GPa
Total Number of Cycles for Optimization	≤ 100

**IV.2.6 Summary of Computational Parameters** 

This computational methodology ensures a rigorous and comprehensive analysis of the structural, electronic, and optical properties of  $4C_{16}H_{10}Br_2O_2$ . By employing DFT-based ab initio calculations, we aim to provide accurate predictions of the material's band gap, optical response, and electronic behavior, which can be further validated through experimental studies [43-45].

#### IV.3. Results and discussions

#### **III.3.1. Structural Parameters**

The compound  $C_{16}H_{10}Br_2O_2$  crystallizes in two distinct structural configurations: an orthorhombic structure with space group Pbnc (N°60) and a monoclinic structure with space group  $P2_I/c$  (N°14). The structural parameters of these two phases were determined using Density Functional Theory (DFT) calculations under the LDA/CA-PZ and GGA/PBE approximations.

The atomic coordinates of  $C_{16}H_{10}Br_2O_2$  for both space groups are presented in Table 1, where a comparison with available experimental data [1] shows that the LDA/CA-PZ method provides good agreement. To refine the calculations, an energy cutoff of 300 eV and a  $3\times3\times3$  k-point mesh were used to ensure convergence.

The lattice parameters, volume, atomic density, and cohesive energy for both structures are summarized in Table VI.2. The LDA/CA-PZ functional provides reduced relative uncertainly in lattice parameters, ranging from 0.6% to 4.9% for the orthorhombic phase and 0.4% to 3.05% for the monoclinic phase, while the GGA/PBE method exhibits larger deviations (4.4% to 10.3% and 0.7% to 16.9%, respectively).

The cohesive energy obtained via LDA/CA-PZ also indicates greater stability for  $C_{16}H_{10}Br_2O_2$ , with values of -16963.594 eV (orthorhombic) and -8493.448 eV (monoclinic), compared to -16942.807 eV and -8482.981 eV using GGA/PBE.

Additionally, the c/a and c/b ratios calculated with LDA/CA-PZ are 0.500 (0.918) and 3.456 (3.268), respectively, while those obtained with GGA/PBE are 0.496 (0.958) and 3.178 (2.941). The LDA/CA-PZ values are in closer agreement with experimental data, which reports 0.483 (0.881) and 3.155 (3.186) for the orthorhombic and monoclinic structures, respectively.

Table. VI.1: The atomic coordinates of  $C_{16}H_{10}Br_2O_2$  in orthorhombic Pnca (N°60) and monoclinic  $P2_1/c$  (N° 14) structures compared with the (experimental values [1])

Specie	X	Y	Z
Н	0.1352 (0.1308) –	0.5911 (0.574) –	0.1871 (0.2007) –
	0.3870 (0.3772)	0.3871 (0.4005)	0.6663 (0.6604)
Н	0.1935 (0.1945) –	0.7582 (0.749) –	0.8887 (0.8962) –
	0.2596 (0.2585)	0.6501 (0.6460)	0.7453 (0.7375)
Н	0.1205 (0.1212) –	0.4875 (0.471) –	0.8242 (0.8163) –
	0.0870 (0.0970	0.6703 (0.6572	0.4530 (0.4553)
Н	0.0521 (0.0524) –	0.2445 (0.245) –	0.9269 (0.9262) –
	0.2199 (0.2174)	0.4167 (0.4236)	0.3706 (0.3781)
Н	0.2408 (0.2500	0.0263 (0.000)	0.9678 (0.9676)
	- 0.4706 (0.4715)	- 0.0870 (0.0818)	- 0.6056 (0.5953)
С	0.0890 (0.0883) –	0.3964 (0.399) –	0.0661 (0.0684) –
	0.3119 (0.3105)	0.3858 (0.3876)	0.5118 (0.5110)
С	0.1314 (0.1291) –	0.5389 (0.553) –	0.1069 (0.1166) –
	0.3220 (0.3212)	0.4494 (0.4543)	0.6172 (0.6188)
С	0.1704 (0.1678) –	0.6548 (0.683) –	0.0477 (0.0546) –
	0.2503 (0.2503)	0.5975 (0.5990)	0.6629 (0.6653)
С	0.1665 (0.1648) –	0.6507 (0.651) –	0.9434 (0.9450) –
	0.1671 (0.1673)	0.6729 (0.6726)	0.6028 (0.6034)
С	0.1237 (0.1234) –	0.5033 (0.494) –	0.9053 (0.9005) –
	0.1543 (0.1538)	0.6104 (0.6073)	0.4981 (0.4962)
С	0.0850 (0.0843) –	0.3683 (0.366) –	0.9634 (0.9618) –
	0.2271 (0.2258)	0.4696 (0.4666)	0.4532 (0.4507)
С	0.2069 (0.2101) –	0.8501 (0.850) –	0.1153 (0.1047) –
	0.3870 (0.3859)	0.2348 (2399)	0.4596 (0.4570)
С	0.2430 (0.2500) –	0.0014 (0.000) –	0.0504(0.0520) –
	0.4665 (0.4672)	0.0791 (0.0760)	0.5219 (0.5218)
0	0.2012 (0.2097) –	0.8637 (0.848) –	0.2064 (0.2068) –
	03819 (0.3816)	0.2339 (0.2478)	0.3648 (0.3613)
Br	0.0379 (0.0360) –	0.2516 (0.2306) –	0.1520 (0.1554) –
	0.0682 (0.0690)	0.8626 (0.8634)	0.6665 (0.6683)

Table. VI.2: The lattice parameters c/a, c/b ratios, volume, density, atomic number and energy of in Pbnc ( $N^{\circ}60$ ) (a),  $P2_{1}/c$  ( $N^{\circ}14$ ) compound.

$C_{16}H_{10}Br_2O_2$	Experimental [1]	LDA	GGA	
Space group	Pbnc (Orthorhombic N°60) – P2 <sub>I</sub> /c (Monoclinic N°14)	Pbnc (N°60)— P2 <sub>1</sub> /c (N°14)	Pbnc (N°60) – P2 <sub>I</sub> /c (N°14)	
Lattice parameter a (Å)	26.48–14.44	26.637–14.283	28.674–14.338	
b (Å)	4.054–3.9937	3.855-4.0123	4.474-4.6715	
c (Å)	12.79–12.7244	13.336–13.1124	14.222-13.7400	
c/a	0.483-0.881	0.500-0.918	0.496-0.958	
c/b	3.155–3.186	3.456–3.268	3.178–2.941	
Cell volume (Å <sup>3</sup> )	726.92	1369.842–746.343	1702.308–914.926	
Z	2	4–2	4–2	
Calculated density (g cm <sup>-3</sup> )	1.8–1.8	1.91075–1.75350	1.53757-1.43040	
Number of atoms in cell	120–120	120–120	120–120	
Energy (eV)		<i>-</i> 16963.594 →	− 16942.807 →	
		- 8493.448	- 8482.981	
β	97.827	96.689	96.205	

#### **IV.3.2.** Electronic Properties

The electronic structure of  $C_{16}H_{10}Br_2O_2$  in both Pbnc (N°60) and  $P2_I/c$  (N°14) space groups was investigated using Density Functional Theory (DFT) with the LDA/CA-PZ approximation. The band structures and density of states (DOS) were computed to analyze the nature of the electronic transitions and the hybridization effects between atomic orbitals. The results are presented in Figure IV.2 and Figure IV.3.

The band structure calculations (Figure IV.2) reveal that  $C_{16}H_{10}Br_2O_2$  exhibits a direct band gap of 0.736 eV at the  $\Gamma$ - $\Gamma$  point in the Pbnc space group, while in the P2<sub>1</sub>/c space group, the band gap is 2eV with an indirect transition between the Y $\rightarrow$ A and Z directions. The position of the valence band maximum (VBM) and conduction band minimum (CBM) indicates the nature of electronic transitions, which are essential for optical and electronic applications.

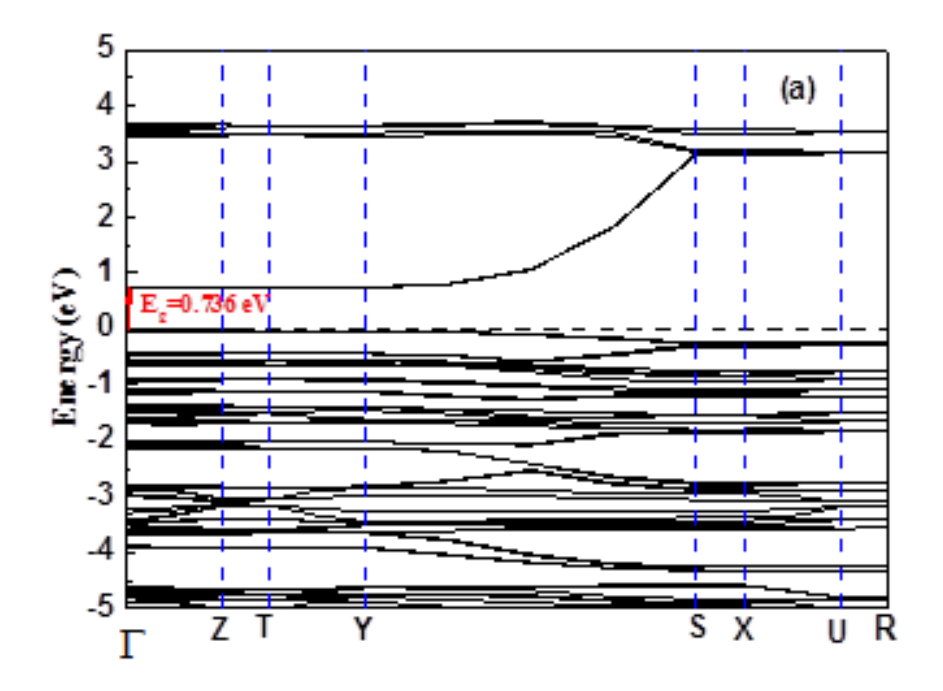
The Density of States (DOS) analysis, shown in Figure IV.3, highlights the contribution of different atomic orbitals to the electronic structure. The valence band is mainly composed of C-p, Br-p, and O-p orbitals, with minor contributions from H-s orbitals. The conduction band is primarily dominated by C-p and O-p orbitals, with a slight contribution from Br-p orbitals in P2<sub>1</sub>/c. The presence of hybridization between O-p, C-p, and Br-p orbitals confirms the covalent nature of bonding in the crystal structure.

A detailed examination of the valence band region (Figure IV.3) shows distinct energy distributions:

- The deep valence states (around -20 eV) are primarily composed of O-s orbitals, with a small contribution from C-s orbitals.
- The mid-valence region (-15 eV to -10 eV) consists of a mix of C-s, Br-s, and C-p orbitals.
- The upper valence band (from -10 eV to 0 eV) is mainly formed by C-p, Br-p, and O-p orbitals, which play a crucial role in determining the electronic transitions.

Given that efficient solar cell materials typically have a band gap between 1.1 and 1.5 eV, the  $P2_{I}/c$  structure (with a 2eV band gap) may have limited photovoltaic efficiency, while the Pbnc structure (with a 0.736 eV band gap) could exhibit enhanced charge transport properties. The calculated band gaps suggest that  $C_{16}H_{10}Br_2O_2$  could have potential applications in optoelectronic and photonic devices.

These results provide a comprehensive understanding of the electronic behavior of  $C_{16}H_{10}Br_2O_2$ , helping to establish its potential for semiconducting applications. Further optical analysis will be discussed in the next section to explore its interaction with electromagnetic radiation.



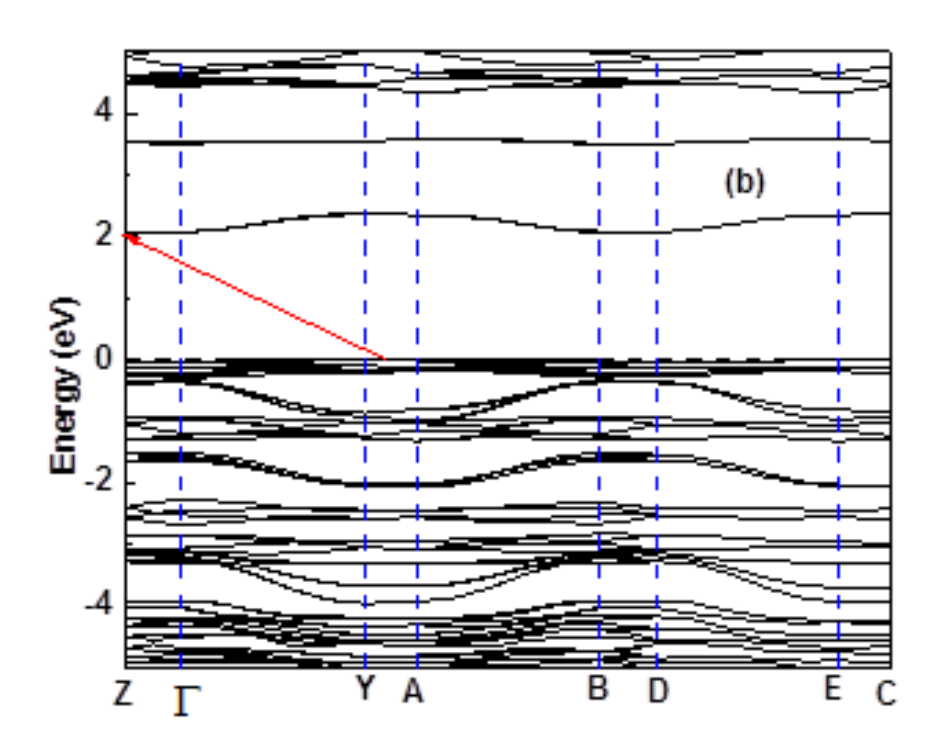
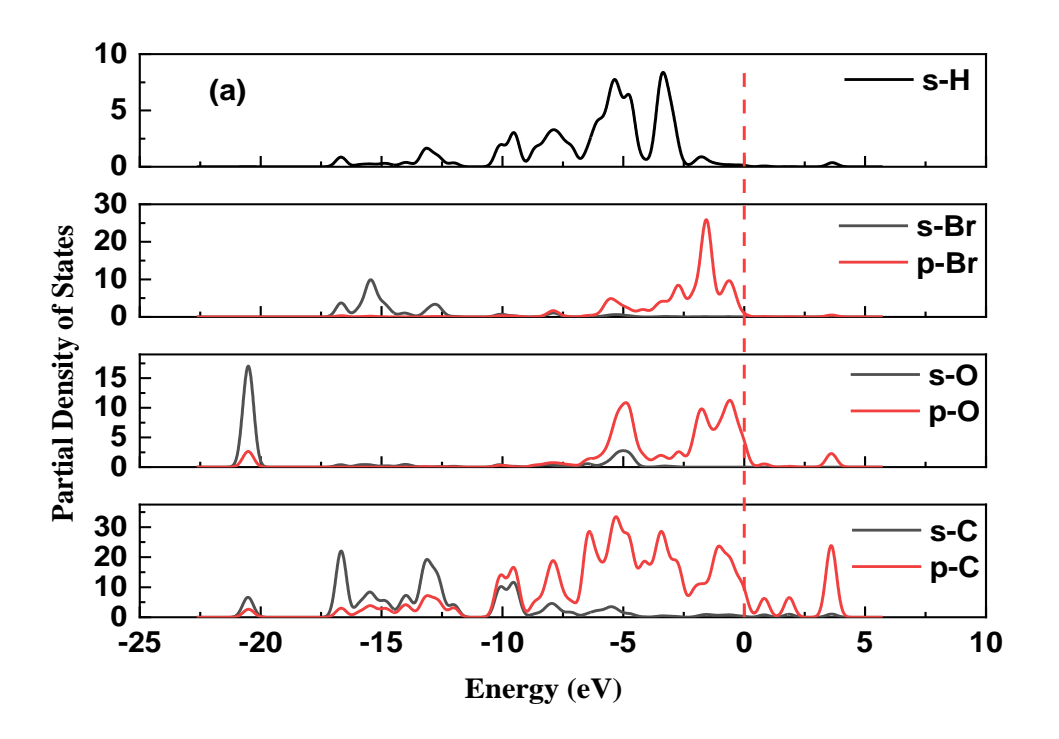


Figure IV.2: DFT calculated Band structure of  $C_{16}H_{10}Br_2O_2$  in Pbnc (a), and  $P2_I/c$  (b) space group.



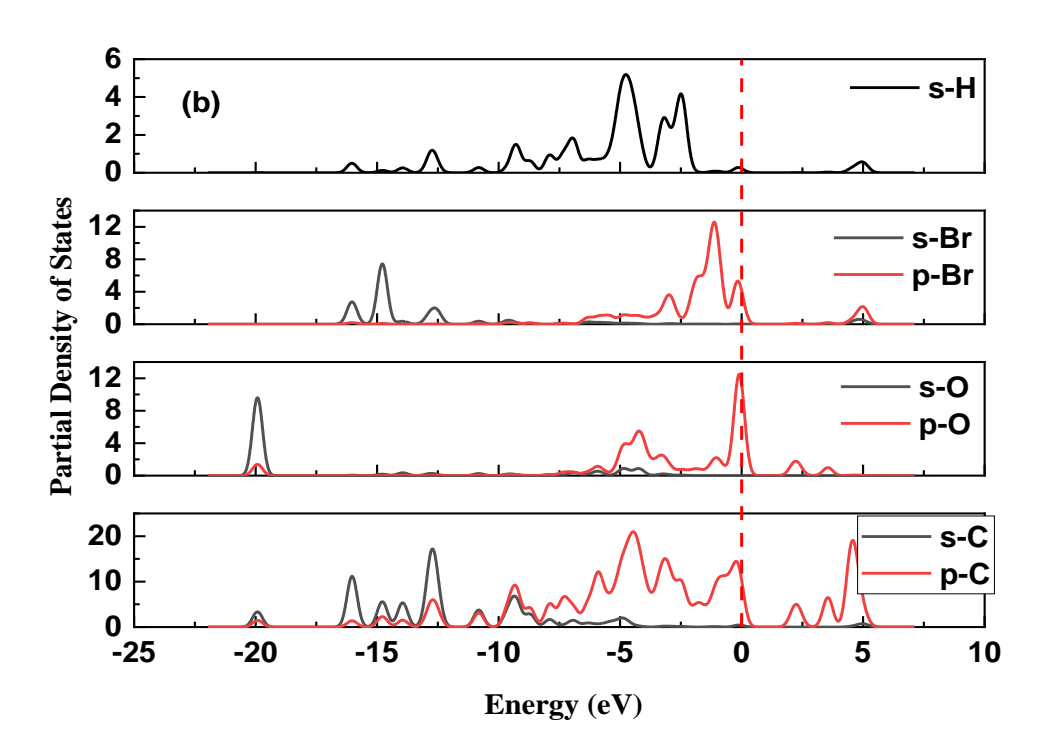


Figure IV.3: The partial density of states of  $C_{16}H_{10}Br_2O_2$  molecule in Pbnc (a) and  $P_{2I}/c$  (b) space group.

### **IV.3.3. Optical Properties**

The optical properties of  $C_{16}H_{10}Br_2O_2$  in both Pbnc (N°60) and P2<sub>1</sub>/c (N°14) space groups were analyzed to investigate its interaction with electromagnetic radiation. The dielectric function  $\varepsilon(\omega) = \varepsilon_1(\omega) + i\varepsilon_2(\omega)$  was computed to evaluate the absorption, reflectivity, refractive index, conductivity, and energy loss function of the material.

# > Dielectric Function

The real  $\varepsilon_1(\omega)$  and imaginary  $\varepsilon_2(\omega)$  parts of the dielectric function describe how the material interacts with an external electric field. The imaginary part  $\varepsilon_2(\omega)$  is obtained from the momentum matrix elements between occupied and unoccupied electronic states [17]:

$$\varepsilon_2(\omega) = \frac{2\omega^2}{\pi V \varepsilon_0} \sum_{k,\nu,c} |\langle \psi_k^c | u \cdot r | \psi_k^{\nu} \rangle|^2 \delta(E_k^c - E_k^{\nu} - \hbar \omega)$$
 (VI.3)

where u is the polarization direction of the incident light, V is the unit cell volume, and  $\psi_k$  represents the wave functions of the valence (v) and conduction (c) bands at a given wave vector k.

Using the Kramers-Kronig relations [18], the real part  $\varepsilon_1(\omega)$  is derived from  $\varepsilon_2(\omega)$ :

$$\varepsilon_1(\omega) = 1 + \frac{2}{\pi} P \int_0^\infty \frac{\omega' \varepsilon_2(\omega')}{\omega'^2 - \omega^2} d\omega'$$
 (VI.4)

where P denotes the principal value of the integral.

The real and imaginary parts of the dielectric function for  $4C_{16}H_{10}Br_2O_2$  in Pbnc and  $P2_I/c$  space groups are shown in Figure IV.4. The static dielectric constant  $\varepsilon_1(0)$  is found to be 4.39eV and 3.55eV for Pbnc and  $P2_I/c$ , respectively.

At photon energies above 15eV,  $\varepsilon_2(\omega) \to 0$ , while  $\varepsilon_1(\infty) = 0.88$  eV, indicating weak high-energy absorption.

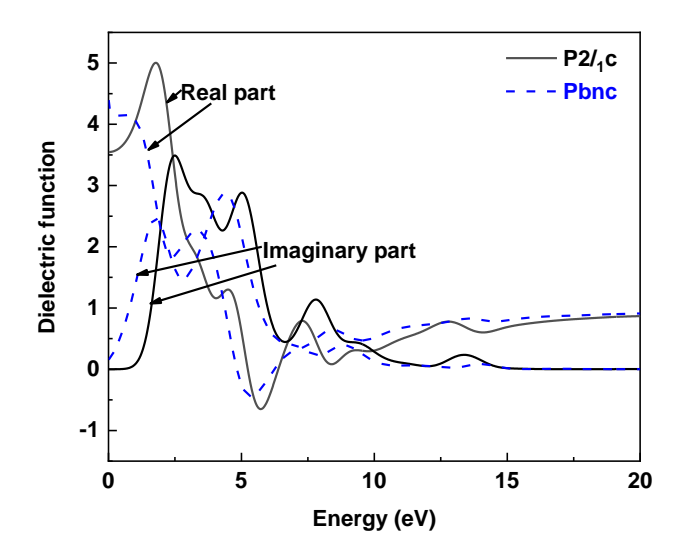


Figure IV.4: Real and imaginary parts of the dielectric function of  $C_{16}H_{10}Br_2O_2$  molecules in *Pbnc* and  $P2_1/c$  space groups as a function of energy.

# > Refractive Index and Optical Absorption

The refractive index  $n(\omega)$ , which describes the speed of light in the material, is computed as:

$$n(\omega) = \frac{1}{\sqrt{2}} \left[ \sqrt{\varepsilon_1^2(\omega) + \varepsilon_2^2(\omega)} + \varepsilon_1(\omega) \right]^{\frac{1}{2}}$$
 (VI.5)

The static refractive index n(0) is 2.979 for Pbnc and 1.88 for  $P2_1/c$ . The refractive index variation with photon energy is shown in Figure IV.5.

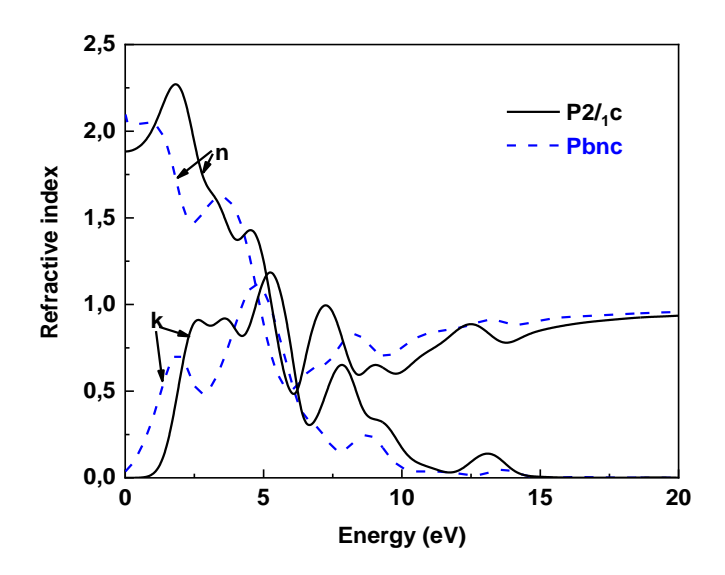


Figure IV.5: The refractive index of  $C_{16}H_{10}Br_2O_2$  in *Pbnc* and  $P2_1/c$  space groups as a function of energy.

The absorption coefficient  $\alpha(\omega)$ , which determines how much light is absorbed at a given photon energy, is calculated using:

$$\alpha(\omega) = \sqrt{2}\omega \left[\sqrt{\varepsilon_1^2(\omega) + \varepsilon_2^2(\omega)} - \varepsilon_1(\omega)\right]^{\frac{1}{2}}$$
 (VI.6)

The absorption spectra for both space groups are depicted in Figure IV.6. The  $4C_{16}H_{10}Br_2O_2$  crystal absorbs photons in the range 0.928eV - 15 eV (Pbnc) and 0.342eV - 15eV (P2<sub>1</sub>/c), covering the visible and ultraviolet spectrum.

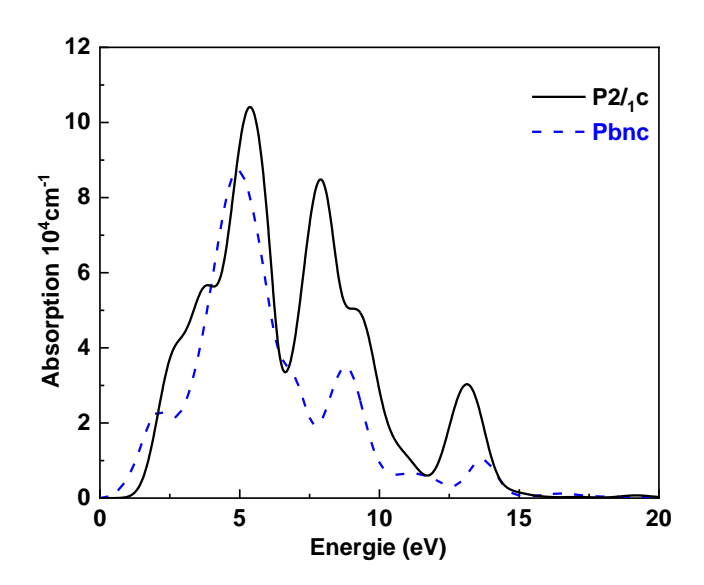


Figure IV.6: The absorption of  $C_{16}H_{10}Br_2O_2$  in *Pbnc* and  $P2_1/c$  space groups as a function of energy.

# Reflectivity and Optical Conductivity

The reflectivity  $R(\omega)$ , which represents the fraction of incident light reflected by the material, is determined by:

$$R(\omega) = \left| \frac{\sqrt{\varepsilon(\omega)} - 1}{\sqrt{\varepsilon(\omega)} + 1} \right|^2$$
 (VI.7)

The reflectivity spectra in Figure IV.7 show maximum reflection intensities at 1.44 eV, 5.53 eV, and 9.46 eV for Pbnc, and at 2.33 eV, 5.92 eV, and 9.46 eV for  $P2_1/c$ .

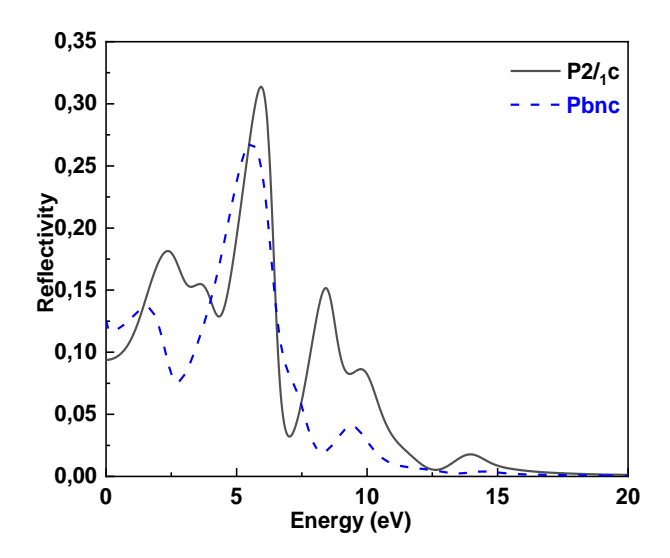


Figure IV.7: The reflectivity of  $C_{16}H_{10}Br_2O_2$  in *Pbnc* and  $P2_1/c$  space groups as a function of energy.

The optical conductivity  $\sigma(\omega)$ , which describes how the material responds to electromagnetic radiation, is given by:

$$\sigma(\omega) = \frac{\omega \varepsilon_2(\omega)}{4\pi} \tag{VI.8}$$

The optical conductivity for both space groups is shown in Figure IV.8. The material exhibits significant conductivity starting at 1.035 eV (P21/c) and 0.36 eV (Pbnc). Conductivity decreases in the range 5 eV -20 eV, indicating a reduced ability to sustain electronic excitations at higher photon energies.

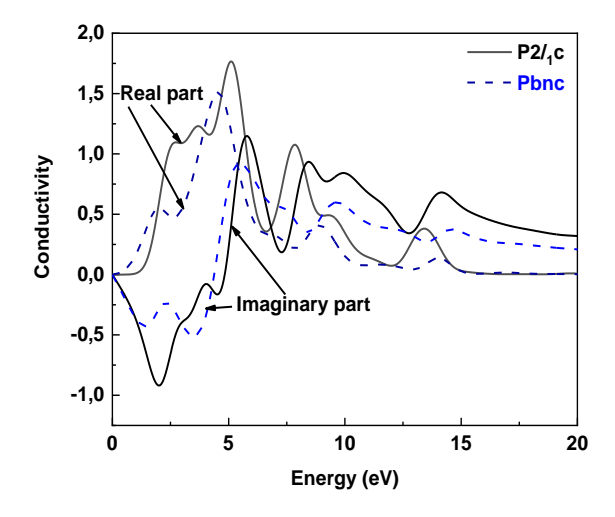


Figure IV.8: The conductivity of  $C_{16}H_{10}Br_2O_2$  in *Pbnc* and  $P2_1/c$  space groups as a function of energy.

### Energy Loss Function

The energy loss function  $L(\omega)$  provides information on how electrons lose energy while traveling through the material. It is related to the dielectric function as:

$$L(\omega) = \frac{\varepsilon_2(\omega)}{\varepsilon_1^2(\omega) + \varepsilon_2^2(\omega)}$$
 (VI.9)

The loss function spectrum, shown in Figure IV.9, exhibits three peaks between 0 eV and 15 eV, indicating significant plasmonic interactions. The effective plasma frequency  $\omega_p$  is determined to be 6.45  $10^{15}$  s<sup>-1</sup> for both space groups.

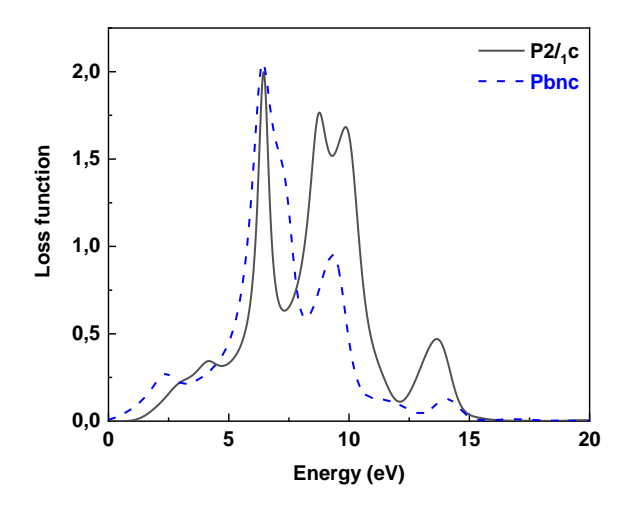


Figure IV.9: The loss functions of  $C_{16}H_{10}Br_2O_2$  in *Pbnc* and  $P2_1/c$  space groups as a function of energy.

The optical analysis of  $4C_{16}H_{10}Br_2O_2$  reveals strong photon absorption in the visible and ultraviolet range, with distinct differences between the Pbnc and  $P2_I/c$  space groups. The material exhibits moderate reflectivity, high refractive indices, and a strong loss function, making it a potential candidate for optoelectronic and photonic applications.

The results indicate that  $4C_{16}H_{10}Br_2O_2$  possesses desirable optical properties, making it a promising material for coating applications, UV absorption, and optoelectronic devices. Future experimental validation is encouraged to further assess its potential technological applications.

### IV.3.4. Population Analysis

To gain a deeper understanding of the electronic distribution and bonding nature in  $C_{16}H_{10}Br_2O_2$ , a Mulliken population analysis was conducted for both the Pbnc (N°60) and P2 $_I$ /c (N°14) space groups. This analysis provides valuable insights into the charge distribution among atoms and the nature of intermolecular interactions within the crystal structure.

### Mulliken Charge Distribution

The Mulliken charge analysis, as summarized in Table VI.3 and Table VI.4, reveals the charge transfer between different atomic species. The carboxyl oxygen (O) carries a negative charge (-0.54 e in Pbnc, 0.28 e in P2<sub>1</sub>/c), while hydrogen (H) exhibits a partial positive charge (0.24 e - 0.30 e in Pbnc, 0.25 e - 0.32 e in P2<sub>1</sub>/c). The bromine (Br) atoms carry a charge of 0.27 e in Pbnc but -0.54 e in P21/c, indicating different electrostatic environments in the two crystal phases [53, 54].

The results suggest that C–Br, C–O, and H–O interactions play an essential role in determining the electronic structure and stability of the crystal. The charge transfer observed in C-Br and C-O bonds indicates a strong covalent character, while the presence of weak Br-H and O-H interactions suggests the possibility of hydrogen bonding and van der Waals forces.

Table VI.3: Mulliken of all electrons for C<sub>16</sub>H<sub>10</sub>Br<sub>2</sub>O<sub>2</sub> in Pbnc (N°60).

Species	s-Orbitals	p–Orbitals	Total	Charge (e)
H	$0.70 \rightarrow 0.76$	0	$0.70 \to 0.76$	$0.24 \to 0.30$
C	$0.96 \rightarrow 1.29$	$2.67 \rightarrow 3.15$	$3.63 \rightarrow 4.44$	$-0.30 \to 0.38$
0	1.82	4.72	6.54	- 0.54
Br	1.68	5.04	6.73	0.27

Table VI.4: Atomic populations (Mulliken) of all electron configurations of atoms for  $C_{16}H_{10}Br_2O_2$  in  $P2_I/c$  (N°14).

Species	s–Orbitals	p–Orbitals	Total	Charge (e)
Н	$0.68 \to 0.75$	0.00	$0.68 \to 0.75$	$0.25 \rightarrow 0.32$
C	$0.99 \to 1.17$	$2.62 \rightarrow 3.13$	$3.61 \rightarrow 4.30$	$-0.06 \rightarrow 0.39$
Br	1.83	4.71	6.54	- 0.54
0	1.68	5.04	6.72	0.28

#### > Bond Population and Geometrical Parameters

The bond population analysis provides a quantitative measure of bond strength and covalency. The calculated bond populations, bond lengths, and bond angles for both space groups are summarized in Table VI.4 and Table VI.6.

The C–Br bond has a population of -0.36 to 0.33 in Pbnc and -0.36 to 0.31 in P2 $_{I}$ /c, with bond lengths of 1.856 Å (Pbnc) and 1.902 Å (P2 $_{I}$ /c), which closely match experimental values.

Similarly, the C–C and C–O bonds exhibit populations that indicate a dominantly covalent character, with bond lengths in good agreement with experimental values. The Br–H and O–H interactions exhibit weak population values, supporting the presence of weak intermolecular interactions that influence the crystal packing.

The bond angles in Pbnc and P21/c structures are consistent with X-ray diffraction data, further validating the computational approach. The C–C–Br and O–C–C angles range from 116.6° to 124.3°, aligning with experimental values.

**Table VI.5:** Geometric parameters of  $C_{16}H_{10}Br_2O_2$  in *Pbnc* (N°60) in brackets those given experimentally.

Bond	Population	Length (Å)	
BrC	-0.36→0.33	1.856 (1.901)	
Н—С	-0.25→1.0	1.086→2.948	
BrH	-0.11	2.941	
С—С	-0.40→1.16	$1.368 \rightarrow 1.525$ $(1.375 \rightarrow 1.410)$	
О—С	-0.18→0.14	1.225 (1.306)	
Н—О	0.00	2.988	
C2-C1-C6→119.5 (122.7)	C3-C4-C5 \rightarrow 115.5 (119.6)	C6-C1-Br→122.2 (119.5)	
C6-C1-C7→119.6 (118.7)	C4-C5-C6 \rightarrow 124.3 (121.6)	O-C7-C3→121.8 (115.6)	
C2-C3-C7→107.7 (119.3)	C5-C6-C1→117.8 (117.8)	O-C7-C8→119.4 (132.0)	
C3-C2-C1→121.6 (119.1)	C3-C7-C8 \rightarrow 105.9 (125.0)		
C4-C3-C2→120.7 (119.2)	C1-C2-Br→118.5 (117.8)		

Length (Å) **Bond Population** Br--C 1.902 (1.896)  $-0.36 \rightarrow 0.31$ H--C  $-0.16 \rightarrow 0.93$  $1.092 \rightarrow 2.778 (0.930)$ Br--H  $-0.11 \rightarrow 0.08$  $2.934 \rightarrow 2.946$ **C--C**  $1.389 \rightarrow 1.520 (1.374 \rightarrow 1.492)$ -0.27→1.28 **O--C** 1.237 (1.211)  $-0.20 \rightarrow 1.06$ H--O  $2.435 \rightarrow 2.658$  $0.0 \rightarrow 0.01$ C2-C1-C6 \rightarrow 116.6 (118.3)  $C3-C4-C5 \rightarrow 122.9 (121.5)$ C5-C4-Br $\rightarrow$ 121.7 (119.37) C2-C1-C7 \rightarrow 123.7 (123.1) C4-C5-C6 \rightarrow 119.3 (118.8)  $O-C7-C1 \rightarrow 117.1 (121.0)$ C6-C1-C7→119.6 (118.7)  $C5-C6-C1 \rightarrow 120.5 (121.3)$  $O-C7-C8 \rightarrow 120.7 (119.7)$  $C3-C2-C1 \rightarrow 123.6 (121.2)$  $C1-C7-C8 \rightarrow 122.1 (119.3)$ C4-C3-C2 \rightarrow 116.8 (119.0)  $C3-C4-Br \rightarrow 115.3 (118.8)$ 

Table VI.6: Geometric parameters (Å) of  $C_{16}H_{10}Br_2O_2$  in  $P2_1/c$  (N°14) in brackets those given experimentally.

#### Intermolecular Interactions and Crystal Packing

The Mulliken population analysis suggests the presence of weak Br–H and O–H intermolecular interactions, which contribute to crystal stabilization. These interactions may influence the packing efficiency of the molecules in the unit cell, affecting the mechanical and thermal stability of the material.

Notably, strong Br–H and O–H intermolecular contacts between diastereoisomers of  $C_{16}H_{10}Br_2O_2$  suggest that these weak interactions play a significant role in crystal cohesion.

The population analysis of  $C_{16}H_{10}Br_2O_2$  in both Pbnc and P21/c space groups highlights several key findings:

- Covalent bonding character is confirmed in C–C, C–O, and C–Br interactions.
- The charge transfer analysis shows that Br and O atoms carry significant partial charges, impacting their role in intermolecular interactions.
- Intermolecular interactions (Br–H and O–H) contribute to crystal packing and structural stability.

- Bond lengths and angles are in good agreement with experimental values, validating the computational methodology.

#### **IV.4. Conclusion**

In this study, we conducted a comprehensive first-principles investigation of the structural, electronic, and optical properties of the organic crystal  $4C_{16}H_{10}Br_2O_2Bis$  (m-Bromobenzoyl) Methane using Density Functional Theory (DFT). The analysis considered two different crystallographic space groups, Pbnc (N°60) and P2<sub>1</sub>/c (N°14), to evaluate how structural variations impact the material's physical properties.

Our structural analysis confirmed that the optimized lattice parameters, bond lengths, and angles are in good agreement with available experimental data. The Mulliken population analysis further revealed the covalent nature of C–Br and C–O bonds, while weak intermolecular interactions (Br–H and O–H) contribute to crystal packing stability.

Electronic band structure calculations showed that the material exhibits a direct band gap of 0.736 eV in the Pbnc structure and an indirect band gap of 2.0 eV in the  $P2_1/c$  structure. The density of states (DOS) analysis highlighted significant hybridization between C, O, and Br orbitals, confirming strong covalent interactions within the crystal.

The optical analysis demonstrated that  $4C_{16}H_{10}Br_2O_2$  has strong absorption in the UV-visible range, with absorption occurring between 0.928 eV - 15 eV (Pbnc) and 0.342 eV - 15 eV (P2<sub>I</sub>/c). The calculated refractive indices, dielectric function, and optical conductivity suggest potential applications in optoelectronics, UV sensing, nonlinear optics, and photonic devices.

Overall, this study provides valuable insights into the physical properties of  $4C_{16}H_{10}Br_2O_2$ , establishing it as a promising candidate for various optical and electronic applications. Future experimental studies are encouraged to validate these findings and explore further functionalization strategies to optimize its technological potential.

# **General Conclusion**

## **General Conclusion**

This thesis has presented a comprehensive study of the physical properties of different classes of materials, including semiconductors, transition metal halides, and organic crystals, using first-principles Density Functional Theory (DFT) calculations. Through a systematic approach, we explored the structural, electronic, optical, and mechanical properties of these materials, providing valuable insights into their potential applications in modern technologies.

#### 1. Semiconductors and Their Fundamental Properties

The study began with a detailed exploration of semiconductor materials, focusing on their electronic band structure, optical response, and mechanical characteristics. The tunability of semiconductors through doping, pressure, and external stimuli was highlighted as a key feature enabling their use in optoelectronic applications such as transistors, LEDs, and photovoltaic cells.

## 2. First-Principles Computational Methods

A rigorous theoretical and computational framework was established to analyze material properties using quantum mechanical methods. The development and implementation of the Density Functional Theory (DFT) approach, including the use of pseudopotentials and plane-wave basis sets, were detailed. The study also discussed essential approximations, such as the Generalized Gradient Approximation (GGA) and Local Density Approximation (LDA), for accurately predicting structural and electronic properties.

#### 3. Transition Metal Halides (WCl<sub>x</sub>, x = 3, 4, 5 and 6) for Optoelectronics

The investigation of tungsten chlorides (WCl<sub>3</sub>, WCl<sub>4</sub>, WCl<sub>5</sub>, β-WCl<sub>6</sub>, and α-WCl<sub>6</sub>) revealed a wide range of structural and electronic behaviors. These materials exhibit polymorphic transformations, tunable band gaps, and strong optical responses, making them suitable for energy storage, catalysis, and optoelectronic applications. The results demonstrated that β-WCl<sub>6</sub> and α-WCl<sub>6</sub> possess direct band gaps, making them potential candidates for photonic and photovoltaic devices, while WCl<sub>4</sub> and WCl<sub>5</sub> exhibit metallic and semi-metallic behavior, respectively, suggesting their utility in conductive coatings and catalysis

#### 4. Organic Crystals (4C<sub>16</sub>H<sub>10</sub>Br<sub>2</sub>O<sub>2</sub>) and Their Optical Properties

The study of the organic compound  $4C_{16}H_{10}Br_2O_2$  (Bis(m-Bromobenzoyl) Methane) demonstrated its potential for optoelectronic and photonic applications. The band structure analysis revealed both direct and indirect band gaps, while the optical properties, including strong UV-visible absorption and a high refractive index, indicate promising applications in nonlinear optics, UV detection, and organic electronic devices. Charge population and bond analysis confirmed the influence of weak intermolecular interactions on crystal stability, further supporting its role in organic semiconductors and coatings.

#### 5. Technological Implications and Future Prospects

The findings of this thesis contribute significantly to the field of material science, particularly in the development of materials for next-generation electronic and optoelectronic applications. Several key technological implications emerge from this study:

#### - Optoelectronics and Photodetectors:

Materials such as  $\beta$ -WCl<sub>6</sub>,  $\alpha$ -WCl<sub>6</sub>, and  $4C_{16}H_{10}Br_2O_2$ , with their direct band gaps and strong absorption in the UV-visible range, can be used in photodetectors, solar cells, and light-emitting devices.

#### - Energy Storage and Catalysis:

Tungsten chlorides exhibit excellent thermal and chemical stability, making them promising candidates for battery electrodes, fuel cell applications, and catalytic processes.

#### - Transparent Conductors and Coatings:

The semi-metallic behavior of WCl<sub>5</sub> and WCl<sub>4</sub> suggests their use in transparent conductive coatings, infrared mirrors, and plasmonic devices for advanced photonic applications.

## - Organic Electronics:

The optical and electronic properties of  $4C_{16}H_{10}Br_2O_2$  highlight its potential for flexible electronics, organic LEDs, and dielectric applications.

#### **6. Future Perspectives**

This work has successfully demonstrated the power of first-principles calculations in predicting and analyzing material properties with high accuracy. The combination of computational modeling and experimental validation offers a pathway to discovering novel materials tailored for specific applications.

Future research directions may include:

- 1. Doping and Defect Engineering: Investigating the effects of doping and structural defects to further enhance the electronic and optical properties of the studied materials.
- 2. Temperature and Pressure Effects: Examining phase transitions and stability under extreme conditions to optimize material performance in real-world applications.
- 3. Advanced Functional Materials: Extending the methodology to emerging materials such as 2D materials, perovskites, and hybrid organic-inorganic compounds.
- 4. Experimental Validation: Collaborating with experimentalists to validate theoretical predictions and refine computational models.

In summary, this thesis has laid the groundwork for understanding and optimizing advanced materials using computational physics. The insights gained will contribute to the ongoing development of efficient, high-performance materials for electronics, photonics, and energy applications.

## **References**

- [1] G. Karkera, M. Soans, B. Dasari, E. Umeshbabu, M.A. Cambaz, Z. Meng, T. Diemant, M. Fichtner, Tungsten Oxytetrachloride as a positive electrode for Chloride-Ion Batteries, Energ. Technol. **10** (2022) 2200193.
- [2] H. Okamoto H. Okamoto Phase Diagrams for Binary Alloys (ASM international Materials Park OH) 44 2000.
- [3] B. Schimmelpfennig, U. Wahlgren, O. Gropen, A. Haaland, "The gas phase structures of tungsten chlorides: density functional theory calculations on WCl 6, WCl 5, WCl 4, WCl 3 and W 2 Cl 6,", J. Chemical SocietyDalton Trans. 1616–1620 (2001).
- [4] B. Ivanova, Comment on "Comment on Crystallographic and theoretical study of the atypical distorted octahedral geometry of the metal chromophore of zinc (II) bis ((1R, 2R)-1, 2-diaminocyclohexane) dinitrate", J. Mol. Struct. **1287** (2023) 135746.
- [5] A. Sevy, R.F. Huffaker, M.D. Morse, Bond dissociation energies of tungsten molecules: WC, WSi, WS, WSe, and WCl, Chem. A Eur. J. **121** (2017) 9446–9457.
- [6] L. Henry, V. Svitlyk, G. Garbarino, D. Sifre, M. Mezouar, Structure of solid chlorine at 1.45 GPa, Zeitschrift Für Kristallographie-Crystalline Materials **234** (2019) 277–280.
- [7] Kohanoff, J. (2006). Electronic structure calculations for solids and molecules: Theory and computational methods. Cambridge University Press.
- [8] R.L. Collin, The crystal structure of solid chlorine, Acta Crystallogr. 5 (1952) 431–432.
- [9] N. Bartalucci, F. Marchetti, S. Zacchini, G. Pampaloni, Decarbonylation of phenylacetic acids by high valent transition metal halides, Dalton Trans. **48** (2019) 5725–5734.
- [10] K. Rinke, H. Schafer, "Nachweis der moleküle W2Cl6 und W3Cl9 im gaszustand, Angew. Chem. 79 (1967) 650–651.
- [11] K.-O. Kirk-Othmer, Encyclopedia of chemical technology, 2 Set, John Wiley & Sons, 2007.
- [12] R.A. Lewis, Hawley's condensed chemical dictionary, John Wiley & Sons, 2016.
- [13] R. Lemus, C.F. Venezia, An update to the toxicological profile for water-soluble and sparingly soluble tungsten substances, Crit. Rev. Toxicol. 45 (2015) 388–411.
- **[14]** M. Bortoluzzi, F. Marchetti, M.G. Murrali, G. Pampaloni, S. Zacchini, The chlorinating behaviour of WCl 6 towards α-aminoacids, Dalton Trans. **44** (2015) 8729–8738.

- [15] M. Bortoluzzi, F. Guarra, F. Marchetti, G. Pampaloni, S. Zacchini, Different outcomes in the reactions of WCl6 with carboxylic acids, Polyhedron **99** (2015) 141–146.
- [16] J. t Taylor and P.-W. Wilson, "Neutron and X-ray powder diffraction studies of the structure of uranium hexachloride," Acta Crystallographica Section B: Structural Crystallography and Crystal Chemistry 30 1974 1481 1484.
- [17] D. Smith, R. Landingham, G. Smith, Q. Johnson, The crystal structure of WCl6, Acta Crystallogr. Sect. B: Struct. Crystallogr. Cryst. Chem. 24 (1968) 1563.
- [18] F.A. Cotton, C. Rice, Tungsten pentachloride, Acta Crystallogr. Sect. B: Struct. Crystallogr. Cryst. Chem. 34 (1978) 2833–2834.
- [19] R. McCarley, T. Brown, The Preparation and reactions of some tungsten (II) and Tungsten (IV) Halides, Inorg. Chem. 3 (1964) 1232–1236.
- [20] V. Kolesnichenko, D.C. Swenson, L. Messerle, Facile reduction of tungsten halides with nonconventional, mild reductants. I. Tungsten tetrachloride: several convenient solid-state syntheses, a solution synthesis of highly reactive (WCl4) x, and the molecular structure of polymeric tungsten tetrachloride, Inorg. Chem. 37 (1998) 3257–3262.
- [21] Y. Zheng, E. Jonas, J. Nuss, H.G. von Schnering, The DMSO Solvated octahedro-[W6Cl] Cl Cluster Molecule, Z. Anorg. Allg. Chem. **624** (1998) 1400–1404.
- [22] S.J. Clark, M.D. Segall, C.J. Pickard, P.J. Hasnip, M.I. Probert, K. Refson, M. C. Payne, First principles methods using CASTEP, Zeitschrift Für KristallographieCrystalline Materials 220 (2005) 567–570.
- [23] T. Chihi, M. Fatmi, B. Ghebouli, First-principles prediction of metastable niobium and tantalium nitrides M4N5 and M5N6 stoichiometry, Solid State Sci. 14 (2012) 80–83.
- [24] H.J. Monkhorst, J.D. Pack, Special points for Brillouin-zone integrations, Phys. Rev. B 13 (1976) 5188.
- [25] P. Hohenberg, W. Kohn, Density functional theory (DFT), Phys. Rev 136 (1964) B864.
- [26] W. Kohn, L.J. Sham, Self-consistent equations including exchange and correlation effects, Phys. Rev. 140 (1965) A1133.
- [27] W. Keesom, K. Taconis, On the crystal structure of chlorine, Physica 3 (1936) 237–242.
- [28] H.-J. Lunk, H. Hartl, Discovery, properties and applications of tungsten and its inorganic compounds, ChemTexts 5 (2019) 15.

- [29] A. N" agele, J. Glaser, H. Meyer, "W6Cl18: Neue Synthesen, neue Strukturverfeinerung, elektronische Struktur und Magnetismus," Zeitschrift für anorganische und allgemeine, Chemie 627 (2001) 244–249.
- [30] Y.S. Ezhov, S. Komarov, Determination of the molecular constants of tungsten tetrachloride from electron diffraction data, J. Struct. Chem. **25** (1984) 71–76.
- [31] Y.S. Ezhov, A. Sarvin, An electron diffraction study of tungsten pentachloride, J. Struct. Chem. **24** (1983) 140–143.
- [32] G. Hautier, S.P. Ong, A. Jain, C.J. Moore, G. Ceder, Accuracy of density functional theory in predicting formation energies of ternary oxides from binary oxides and its implication on phase stability, Phys. Rev. **B 85** (2012) 155208.
- [33] D. E. Williams, Z. L. Dumke and R. E. Rundle, Acta Cryst. 15 627 (1962).
- [34] D. N. Lastovickova, J. J. La Scala and R. C. Sausa, Acta Cryst. E74 352 (2018).
- [35] Xiaolu Liu, Yang Li, Zhongshan Chen, Hui Yang, Suhua Wang, Zhenwu Tang, Xiangke Wang, Eco-Environment & Health 2 (2023) 117–130.
- [36] Lin Fang, Tao Huang, Hua Lu, Xi-Lin Wu, Zhongshan Chen, Hui Yang, Suhua Wang, Zhenwu Tang, Zhuang Li, Baowei Hu and Xiangke Wang, (2023) 5:42
- [37] Shoji Watanabe, Kosuke Nakaema, Toyokazu Muto, Akiko Okamoto, and Noriyuki Yonezawa, Acta Crystallogr Sect E, 66 2 (2010) o403. [6] Gordon R. Engebretson, R. E. Rundle, *J. Am. Chem. Soc*, 86 4 (1964) 574–581.
- [38] Borduin, W. G. Substituent effects on the spectra and ionization constants of diaroylmethanes. Unpublished M.S. thesis. Ames, Iowa, Library, Iowa State University of Science and Technology. 1954.
- [39] Z. Zerrougui, M. A. Ghebouli, T. Chihi, S. I. Ahmed, L. Krache, B. Ghebouli, M. Fatmi, *J. Mater. Res. Technol.* 18 396 (2022).
- [40] J. P. Perdew, K. Burke and M. Ernzerhof, *Phys. Rev. Lett.* 77 3865 (1996).
- [41] J. S. Lin, A. Qteish, M. C. Payne and V. Heine, *Phys. Rev. B* 47 4174 (1993)
- [42] H. J. Monkhorst and J. D. Pack, *Phys. Rev. B* 13 5188 (1976).
- [43] P. Hohenberg and W. Kohn, *Phys. Rev. B* 136 864 (1964).
- [44] W. Kohn and L. J. Sham, *Phys. Rev. A* 140 1133 (1965)
- [45] E. L. Albuquerque, U. L. Fulco, V. N. Freire, E. W. S. Caetano, M. L. Lyra and B. F. Moura *Phys. Rep.* 535 139 (2014).
- [46] R. L. Araujo, M. S. Vasconcelos, C. A. Barboza, N. X. Lima, E. L. Albuquerque and U. L. Fulco, *Comput. Theor. Chem.* 1170 112621 (2019).
- [47] M. Jubair, A. M. Karim, M. Nuruzzaman and M.A. Zilani, *J. Phys. Commun.* 3 055017 (2019).

- [48] D. Li, F. Ling, Z. Zhu and X. Zhang, *Phys. Rev. B Condens. Matter* 406 3299 (2011).
- [49] Y. Fang, X. Kong, D. Wang, J. Lu and D. Cui, J. Phys. Chem. Solids 127 107 (2019).
- [50] M. Zhong, Q. J. Liu, C. L. Jiang, F. S. Liu, B. Tang and X. J. Peng, *J. Phys. Chem. Solids* 121 139 (2018).
- [51] I. Sharma, S. Reddy Madara, P. Sharma, Mater. Today Proc. 28 (2020) 402–407.
- [52] M. A. Rahman, M. Z. Rahaman and M. A. Sarker, *Comp. Condens. Matter.* 9 19 (2016).
- [53] M. D. Segall, C. J. Pickard, R. Shah and M. C. Payne, *Mol. Phys.* 89 571 (1996).
- [54] M. D. Segall, R. Shah, C. J.Pickard and M. C. Payne, *Phys. Rev. B* 54 16317 (1996).

#### **Abstract**

This thesis presents a first-principles study of the structural, electronic, and optical properties of selected binary intermetallic compounds of type AB<sub>3</sub>, using Density Functional Theory (DFT). The aim is to provide a fundamental understanding of these materials and assess their potential applications in optoelectronics, energy storage, and catalysis.

The study begins with an overview of semiconductor physics, emphasizing the role of band structures, optical transitions, and mechanical stability in determining material performance. Next, a detailed computational methodology is introduced, describing the use of DFT-based simulations, pseudopotential methods, and exchange-correlation functionals to accurately predict material properties.

The investigation focuses on transition metal halides (WCl<sub>x</sub>, x = 3 to 6) and an organic crystal ( $4C_{16}H_{10}Br_2O_2$ ). The results show that  $\beta$ -WCl<sub>6</sub> and  $\alpha$ -WCl<sub>6</sub> exhibit direct band gaps and strong UV-visible absorption, making them suitable for photodetectors and solar cells. Meanwhile, WCl<sub>4</sub> displays metallic properties, suggesting applications in conductive coatings and catalysis. The study of the organic compound  $4C_{16}H_{10}Br_2O_2$  reveals high refractive indices and strong absorption in the UV-visible range, indicating potential use in nonlinear optics and organic electronic devices

Overall, this work provides valuable insights into the fundamental properties of  $AB_3$ -type intermetallic compounds and highlights their potential for next-generation optoelectronic and energy applications. Future research could focus on doping effects, temperature stability, and experimental validation to further optimize their performance.

**Keyword :** Density Functional Theory (DFT); Binary Intermetallic Compounds (AB<sub>3</sub>); Electronic Structure; Optical Properties; Band Gap Engineering; Transition Metal Halides (WCl<sub>x</sub>, x = 3 to 6).

#### Résumé

Cette thèse présente une étude ab initio des propriétés structurales, électroniques et optiques de certains composés intermétalliques binaires de type AB<sub>3</sub>, en utilisant la Théorie de la Fonctionnelle de la Densité (DFT). L'objectif est d'analyser en profondeur ces matériaux afin d'évaluer leur potentiel pour des applications en optoélectronique, stockage d'énergie et catalyse.

L'étude commence par une analyse des propriétés fondamentales des semi-conducteurs, mettant en évidence l'importance des structures de bande, des transitions optiques et de la stabilité mécanique. Ensuite, une méthodologie détaillée est exposée, décrivant l'utilisation des simulations DFT, des pseudopotentiels et des fonctionnelles d'échange-corrélation pour prédire avec précision les propriétés des matériaux.

L'investigation porte sur les halogénures de tungstène (WCl<sub>x</sub>, x=3 à 6) ainsi qu'un cristal organique (4C<sub>16</sub>H<sub>10</sub>Br<sub>2</sub>O<sub>2</sub>). Les résultats montrent que  $\beta$ -WCl<sub>6</sub> et  $\alpha$ -WCl<sub>6</sub> possèdent un gap direct et une forte absorption UV-visible, ce qui les rend prometteurs pour les photodétecteurs et cellules solaires. De son côté, WCl<sub>4</sub> présente un comportement métallique, suggérant des applications en revêtements conducteurs et catalyse. L'étude du composé organique 4C<sub>16</sub>H<sub>10</sub>Br<sub>2</sub>O<sub>2</sub> révèle une forte absorption UV-visible et un indice de réfraction élevé, ce qui le rend intéressant pour des applications en optique non linéaire et électronique organique.

En conclusion, cette thèse apporte des informations précieuses sur les propriétés des composés intermétalliques  $AB_3$  et souligne leur potentiel pour les technologies de nouvelle génération. Des recherches futures pourraient explorer l'effet du dopage, la stabilité thermique et une validation expérimentale pour optimiser davantage leurs performances.

**Mots-clés :** Théorie de la Fonctionnelle de la Densité (DFT) ; Composés Intermétalliques Binaires (AB<sub>3</sub>) ; Structure Électronique ; Propriétés Optiques ; Ingénierie du Gap Électronique ; Halogénures de Métaux de Transition (WCl<sub>x</sub>,  $x = 3 \ a$  6).

#### لملخص:

نتناول هذه الأطروحة دراسة نظرية أولية للخصائص الهيكلية والإلكترونية والبصرية لبعض المركبات البينفلزية الثنائية من النوع AB<sub>3</sub> باستخدام نظرية الكثافة الوظيفية (DFT). تهدف هذه الدراسة إلى تحليل هذه المواد بعمق وتقييم إمكانياتها في مجالات الإلكترونيات الضوئية وتخزين الطاقة والتحفيز الكيميائي.

يُبدأ البحث بعرضٌ شامل للمواد شبه الموصلة، مع التركيز على أهمية بنية النطاق الإلكتروني، والانتقالات الضوئية، والاستقرار الميكانيكي. كما يتم تقديم منهجية حسابية مفصلة تعتمد على المحاكاة باستخدام DFT، مع استخدام الجهود الكاذبة (pseudopotentials) والدوال التقريبية للتبادل والارتباط لحساب الخصائص الفيزيائية بدقة.

α- β-WCI<sub>6</sub> النتائيستن (E = X- E = X-

توفر هذه الأطروحة رؤى هامة حول الخصائص الفيزيائية لمركبات AB<sub>3</sub> البينفلزية، مما يبرز إمكاناتها في التقنيات الحديثة. يمكن أن تركز الأبحاث المستقبلية على تأثير التطعيم، واستقرار المواد عند درجات حرارة مختلفة، والتحقق التجريبي لتحسين أدائها بشكل أكبر.

الكلمات المفتاحية: نظرية الكثافة الوظيفية (DFT) ؛ المركبات البينفلزية الثنائية (AB<sub>3</sub>) ؛ البنية الإلكترونية ؛ الخصائص البصرية ؛ هندسة فجوة الطاقة ؛ هاليدات المعادن الانتقالية (WCl<sub>x</sub>, x = 3).